Master's thesis

NTNU
Norwegian University of Science and Technology
Faculty of Engineering
Department of Energy and Process Engineering

Thor Gudmund Weisz

Pragmatic Modeling of Flow in the Human Upper Airways for Sleep Apnea Treatment

Master's thesis in Mechanical Engineering
Supervisor: Bernhard Müller
Co-supervisor: Reidar Kristoffersen
June 2022

NTNU
Norwegian University of Science and Technology

Thor Gudmund Weisz

Pragmatic Modeling of Flow in the Human Upper Airways for Sleep Apnea Treatment

Master's thesis in Mechanical Engineering
Supervisor: Bernhard Müller
Co-supervisor: Reidar Kristoffersen
June 2022

Norwegian University of Science and Technology
Faculty of Engineering
Department of Energy and Process Engineering

NTNU
Norwegian University of
Science and Technology

NTNU

Norwegian University
of Science and Technology

Department of Energy
and Process Engineering

EPT-M-2022

MASTER THESIS

for

Student Thor Gudmund Weisz

Spring 2022

Pragmatic Modeling of Flow in the Human Upper Airways for Sleep Apnea Treatment
Pragmatisk modellering av strømning i de menneskelige øvre luftveier for søvnapné behandling

Background and objective

The master thesis will be a part of the larger research project "Virtual Surgery in the Upper Airways - New Solutions to Obstructive Sleep Apnea Treatment (VirtuOSA)" funded by the Research Council of Norway. Obstructive sleep apnea (OSA) is a sleep related breathing disorder caused by repetitive collapses of the upper airways during sleep, resulting in reduced breathing, oxygen desaturation and sleep disturbances, thus leading to cardiovascular diseases. In VirtuOSA, an interdisciplinary team with experts from St. Olavs Hospital, NTNU and SINTEF aims to develop a software tool for treatment of OSA through virtual surgery.

In the master thesis, the upper airways of obstructive sleep apnea (OSA) patients will be modeled in pragmatic, i.e., suitable simplified ways. The geometries of upper airways of OSA patients before and after nasal surgery are provided by experts from St. Olavs Hospital. The outcome of nasal surgery for OSA is documented for OSA patients. The goal of the project is to provide a tool for surgeons from CT scans of OSA patients to flow predictions. Machine learning may be used to tune the model.

The following tasks are to be considered:

1. to get a basic understanding of sleep apnea and its treatment,
2. to verify a pragmatic model of flow in the upper airways for OSA patients by means of CFD,
3. to provide a tool from CT scans of OSA patients to flow predictions,
4. to assess the potential and limits of the pragmatic model.

-- " --

Within 14 days of receiving the written text on the master thesis, the candidate shall submit a research plan for his project to his supervisors.

When the thesis is evaluated, emphasis is put on processing of the results, and that they are presented in tabular and/or graphic form in a clear manner, and that they are analyzed carefully.

The thesis should be formulated as a research report with summary in English, conclusion, literature references, table of contents etc. During the preparation of the text, the candidate

should make an effort to produce a well-structured and easily readable report. In order to ease the evaluation of the thesis, it is important that the cross-references are correct. In the making of the report, strong emphasis should be placed on both a thorough discussion of the results and an orderly presentation.

The candidate is requested to initiate and keep close contact with his academic supervisors throughout the working period. The candidate must follow the rules and regulations of NTNU as well as possible directions given by the Department of Energy and Process Engineering.

Risk assessment of the candidate's work shall be carried out, in cooperation with the supervisors, according to the department's procedures. The risk assessment must be documented and included as part of the final report. Events related to the candidate's work adversely affecting the health, safety or security, must be documented and included as part of the final report. If the documentation on risk assessment represents a large number of pages, the full version is to be submitted electronically to the supervisors and an excerpt is included in the report. Those who have a theoretical exercise only need to check this and fill out page 1 of the form provided by the Department of Energy and Process Engineering.

Pursuant to “Regulations concerning the supplementary provisions to the technology study program/Master of Science” at NTNU §20, the Department reserves the permission to utilize all the results and data for teaching and research purposes as well as in future publications.

The master's thesis is to be submitted in NTNU’s examination system Inspera Assessment by 15:00 h on June 11, 2022.

☐ Work to be done in lab
☐ Field work

Department of Energy and Process Engineering, January 10, 2022

_____
Bernhard Müller
Academic Supervisor

_____
Reidar Kristoffersen
Co-supervisor

Abstract

A pragmatic model has been developed to provide rapid flow predictions on a patient-specific basis to gain insight into the state of a patient's airways. These flow predictions are aimed to be further used to predict the outcome of obstructive sleep apnea (OSA) surgery and provide the basis for a patient-specific system to be used by medical doctors. The pragmatic model transforms the human upper airways into a piping system by applying the hydraulic diameter equation to cross-sections extracted from 3D geometries created based on patient-specific computed tomography (CT) images. In this thesis, the pragmatic model has been expanded to include a system for creating the patient-specific 3D models, which provide the input for the pragmatic flow simulations. CFD simulations of a simplified version of the nasal cavity were performed to assess the use of the hydraulic diameter on the complex cross-sections in this region. The test cases implied that the standard hydraulic diameter was not entirely accurate in the nasal cavity by performing both CFD and pragmatic simulations. Therefore a novel approach that involved substituting the constant 4 in the hydraulic diameter equation with a variable coefficient, C_{D_h}, termed the hydraulic diameter coefficient, was proposed. The results from the validation case showed that $C_{D_h} = 3.71$ gave more accurate results when applied to the pragmatic simulations for the test cases. Negligible improvements were found when applying the new coefficient to the pragmatic simulations for the upper airways of an OSA patient. The hydraulic diameter coefficient was further decreased to obtain the coefficient which gave the best results. $C_{D_h} = 1.80$ gave the best agreement with the verification data available. Pressure-recovery coefficients have been implemented in the pragmatic model to adjust for unphysical pressure increases seen in sections with expanding geometries in the previous model iteration. The implementation of pressure-recovery coefficients in these sections, using an optimization approach, gave excellent agreement with the verification data. Applying the obtained coefficients to the same patient's post-operative geometry gave a similarly good result. Patient-specific pragmatic simulations for two other patients have been performed by applying the same simulation settings for the hydraulic diameter and the pressure-recovery coefficients. However, results from these simulations proved to be inconclusive. In conclusion, notable improvements to the pragmatic model have been made by adjusting the proposed hydraulic diameter coefficient and for unphysical pressure recovery by applying pressure-recovery coefficients.

Sammendrag

En pragmatisk modell for å gi pasientspesifikke strømningsprediksjoner har tidligere blitt utviklet for raskt kunne gi få innsikt i tilstanden til pasienters luftveier. Disse strømningsprediksjonene skal videre brukes til å forutsi utfallet av obstruktiv søvnapné-kirurgi og gi grunnlaget for et pasientspesifikt system som skal brukes av leger. Modellen gjør om menneskets øvre luftveier til et rørsystem ved å bruke den hydrauliske diameterligningen på tverrsnitt tatt fra 3D-geometrier laget basert på pasientspesifikke CT- bilder. I denne oppgaven har den pragmatiske modellen utvidet for å inkludere et system for å lage de pasientspesifikke 3D-modellene, som er grunnlaget de pragmatiske strømningssimuleringene. CFD-simuleringer av en forenklet versjon av nesehulen har blitt utført for å vurdere bruken av den hydrauliske diameteren på de komplekse tverrsnittene i denne regionen. Testtilfellene antydet at den konvensjonelle hydrauliske diameteren ikke var helt nøyaktig i nesehulen ved å utføre både CFD og pragmatiske simuleringer. Derfor ble det foreslått en ny tilnærming som innebar å erstatte konstanten 4 med en variabel koeffisient, C_{D_h}, kalt den hydrauliske diameterkoeffisienten. Resultatene fra valideringen viste at $C_{D_h} = 3.71$ ga mer nøyaktige resultater når de ble brukt på de pragmatiske simuleringene for testtilfellene. Ubetydelige forbedringer ble funnet når den nye koeffisienten ble brukt på de pragmatiske simuleringene for de øvre luftveiene til en søvnapné -pasient. Den hydrauliske diameterkoeffisienten ble ytterligere redusert for å oppnå en koeffisient med best mulig resultater. $C_{D_h} = 1,80$ ga best samsvar med tilgjengelige bekreftelsesdata. Trykkgjenvinningskoeffisienter ble videre implementert i den pragmatiske modellen for å justere for de ufysisikalske trykkøkningene observert i seksjoner med ekspanderende geometrier i forrige iterasjon av den pragmatiske modellen. Implementeringen av trykk-gjenopprettingskoeffisienter i disse seksjonene, ved bruk av en optimaliseringstilnærming, ga utmerket samsvar med verifikasjonsdataene. Bruk av de oppnådde koeffisientene på samme pasients postoperative geometri ga et tilsvarende godt resultat. Pasientspesifikke pragmatiske simuleringer for to andre pasienter er utført ved å bruke de samme simuleringsinnstillingene for den hydrauliske diameteren og trykkgjenvinningskoeffisienten. Resultatene fra disse simuleringene viste seg imidlertid å være usikre. Avslutningsvis har bemerkelsesverdige forbedringer av den pragmatiske modellen blitt gjort ved bruk av den foreslåtte hydrauliske diameterkoeffisienten, sammen med justering for den ufysikalske trykkgjenvinningen ved å bruke trykkgjenvinningskoeffisienter.

Acknowledgements

I would first like to thank my thesis supervisor Bernhard Müller from the department of energy and process engineering at NTNU. Through detailed and constructive feedback he has consistently helped steer me in the right direction while allowing this thesis to be my own work.

Secondly I would like to thank my thesis co-supervisor Reidar Kristoffersen from the department of energy and process engineering at NTNU. Through valuable discussion and creative suggestions he inspired me to pursue new ideas and aided in the continued progress of my work.

Finally, I must express my gratitude to my parents for providing me with unfailing support and continuous encouragement throughout my years of study and through the process of researching and writing this thesis. Thank you.

Thor Gudmund Weisz

Table of Contents

Abstract **iii**

Sammendrag **v**

Acknowledgments **vii**

Nomenclature **xi**

List of Figures **xv**

List of Tables **xvii**

1 Introduction **1**

1.1 Obstructive Sleep Apnea 1

1.1.1 The Human Respiratory System 2

1.1.2 Treatment of OSA 2

1.1.3 Surgical Treatment of OSA 3

1.2 Medical Imaging 5

1.3 Fluid Mechanics in Medicine 5

1.3.1 Improvements and Modern Approaches 6

1.3.2 Approximating the Upper Airways as a Piping System 6

1.3.3 Hydraulic diameter applied to the Human Upper Airways . . . 6

1.4 The Objective of this Thesis 7

1.5 Thesis Outline 8

2 Mathematical Models **9**

2.1 Governing Equations for the Pragmatic Model 9
2.1.1 Bernoulli Equation with Losses 9
2.1.2 Volumetric Flow Rate 10
2.1.3 Major Losses 10
2.1.4 Minor Losses 11
2.1.5 Hydraulic Diameter 12
2.1.6 Diffuser 13
2.1.7 Governing Equations for CFD 13

3 Method **15**
3.1 Introduction to the Pragmatic Model 15
3.2 Data Extraction 15
3.2.1 Processing Medical Images and Automatic Segmentation . . . 16
3.2.2 Creating a 3D Model of the Airways 16
3.2.3 Removing Noise from the 3D model 18
3.2.4 Extracting Cross-Sections from 3D Models 18
3.3 1D Flow Simulations 19
3.3.1 The Airways as Piping System 20
3.3.2 Modeling Irreversible Losses 23
3.3.3 Flow Simulation Results 24
3.3.4 Choice of Verification Case 24
3.3.5 Assessing the Accuracy of a Simulation 25
3.3.6 Outline of the Solver 26

4 Numerical Validation of the Hydraulic Diameter **31**
4.1 Method 31
4.1.1 Numerical Setup 31
4.1.2 Inlet and Boundary Conditions 33
4.1.3 Grid Generation 33
4.1.4 Tuning the Hydraulic Diameter 34

4.1.5 Minor Losses and Diffuser Effects . . . 34
4.1.6 Verification of the Numerical Code . . . 35
4.1.7 Pragmatic Simulations . . . 36
4.2 Results and Discussion . . . 37
4.2.1 Wall with Wedged Ends . . . 37
4.2.2 Wall with Flat Ends . . . 37
4.3 Conclusions for Validation of Hydraulic Diameter . . . 38

5 Results and Discussion **41**
5.1 Hydraulic Diameter Coefficient . . . 41
5.2 Pressure Recovery Coefficient . . . 42
5.3 Post Operative Results . . . 45
5.4 Patient Specific Results . . . 46
5.5 Sensitivity Study . . . 47
5.6 Computing Time of the Pragmatic Model . . . 48
5.7 Discussion of the Hydraulic Diameter as Choice of Optimization Parameter . . . 50

6 Conclusions **51**

7 Further Work **53**

Bibliography **55**

Appendix **59**
A Conference Paper Submitted to SIMS2022 . . . 59
B Python Code . . . 68
C Ansys Fluent Settings and Solution Report . . . 77

Nomenclature

Abbreviations

AHI	Apnea hypopnea index
CAD	Computer aided design
CFD	Computational fluid dynamics
CPAP	Continuous positive airway pressure
CT	Computed tomography
DICOM	Digital Imaging and Communication in Medicine
HU	Hounsfield unit
MMA	Maxillomandibular Advancement
MRI	Magnetic resonance imaging
OSA	Obstructive sleep apnea
RSS	Residual sum of squares
STL	Stereolithography
UPPP	Uvulopalatopharyngoplasty

Greek Letters

ρ	Density [kg/m^3]
α	Kinematic energy correction factor [-]

Symbols

ΔL	Length of a section [m]
C_{D_h}	Hydraulic diameter Coefficient [-]
D_h	Hydraulic diameter [m]
g	Gravitational acceleration [m/s^2]
$h_{L,major}$	Major losses [m]

$h_{L,minor}$	Minor losses [m]
h_L	Total head loss [m]
K_L	Minor loss coefficient [-]
p	Pressure [Pa]
V	Velocity [m/s]
z	Height [m]
Re	Reynolds number [-]
Re_{avg}	Averaged Reynolds number [-]
f	Darcy friction factor [-]

List of Figures

1.1 Representation of a collapsed airway 2

1.2 The anatomy of the human upper airways 3

3.1 Screenshot from CT segmentation in 3D Slicer 17

3.2 Noise removal in MeshMixer 18

3.3 Simplified representation of a 90° bend in SpaceClaim 20

3.4 Extracting cross-sectional data in SpaceClaim 21

3.6 Hydraulic diameter conversion for a nasal cavity cross-section 21

3.5 Location and numbering of cross-sections in the upper airways 22

3.7 The human upper airways as a piping system 22

3.8 An arbitrary section of an OSA patient's upper airways after its conversion to a piping system. 24

3.9 Pre and post-operative results of turbulent CFD simulations of patient 12 [38]. 25

3.10 Flowchart outlining the pragmatic model's solution algorithm. 27

4.1 Numerical setup with 10.4° wedges at both ends of the separating wall. 32

4.2 Numerical setup where the leading and trailing ends of the separating wall are flat. 33

4.3 Verification of numerical setup 36

4.4 Numerical and pragmatic results for test case with wedge 38

4.5 Numerical and pragmatic results for test case without wedge 39

4.6 Calculations of the RSS values for both test cases 39

5.1 Pragmatic simulation results from varying the hydraulic diameter coefficient C_{D_h} 43

5.2 RSS values for the deviation between pragmatic and CFD results . . 44

5.3 Results from pragmatic simulations with pressure-recovery coefficients included 45

5.4 Pragmatic simulation using post-operative data 46

5.5 Pragmatic simulations using data from patient 1 and patient 6 47

List of Tables

2.1 Minor losses for a gradual expansion, $\theta = 20°$ [32, p. 367]. 12
2.2 Minor losses for a gradual contraction [32, p. 367]. 12

3.1 Extracted data from 3D model of patient 12's upper airways. 26

4.1 The pragmatic model's input for test case simulations 36

5.1 Data extracted from the 3D geometries of patient 1 and patient 6. . . 48
5.2 Results from sensitivity study 49
5.3 Computational time for pragmatic simulations 49

Chapter 1

Introduction

This section is adapted from the author's specialization project [1]. The human respiratory system performs one of the most vital functions for humans to live and function well. Its main functions are providing the entire body with oxygen and removing CO_2 produced in the cells through cellular respiration [2]. Given the system's functions, it needs to function continuously and without fail. Any issues with the respiratory system could affect the entire body. Research within this field to provide insights and new medical advancements is incredibly important for those who suffer from ailments affecting the respiratory system's functioning. The collapse of the airways causes one such ailment during sleep leading to a blockage of oxygen supply and removal of CO_2. This problem is known as obstructive sleep apnea (OSA) [3]. In the human upper airways, the complex geometries cause a variety of flow phenomena that lead to OSA. Understanding the underlying flow structures can yield important insights and help improve many people's lives. This master's thesis aims to aid in the further understanding of these phenomena and contribute to the furthered research in this field through an engineering perspective.

1.1 Obstructive Sleep Apnea

Obstructive sleep apnea (OSA) is a condition that negatively impacts the quality of sleep of those affected by it by causing collapses in the upper airways, which obstruct airflow. A representation of a collapse in the upper airways of a patient with OSA is shown in Fig. 1.1. Recent estimates from the United States show that the condition impacts 9% to 38% of the adult population [4]. There are several surgical and non-surgical treatment options that help to alleviate or remove OSA entirely. Even though OSA was first described in the middle of the last century [5], the outcome of corrective surgery is still not entirely predictable [6], [7]. There are two ways of defining obstructive sleep apnea. The first definition is five or more pharyngeal collapses per hour with daytime symptoms of the disorder. Daytime symptoms include excessive daytime sleepiness, fatigue, and impaired cognition despite getting enough sleep. The other definition is 15 or more pharyngeal collapses without the associated symptoms [8]. The severity of sleep apnea is determined by measuring the

total number of overnight events and dividing it by the number of hours of sleep, thus obtaining the average number of abruptive events per hour. This severity measurement is known as the apnea-hypopnea index (AHI) [9].

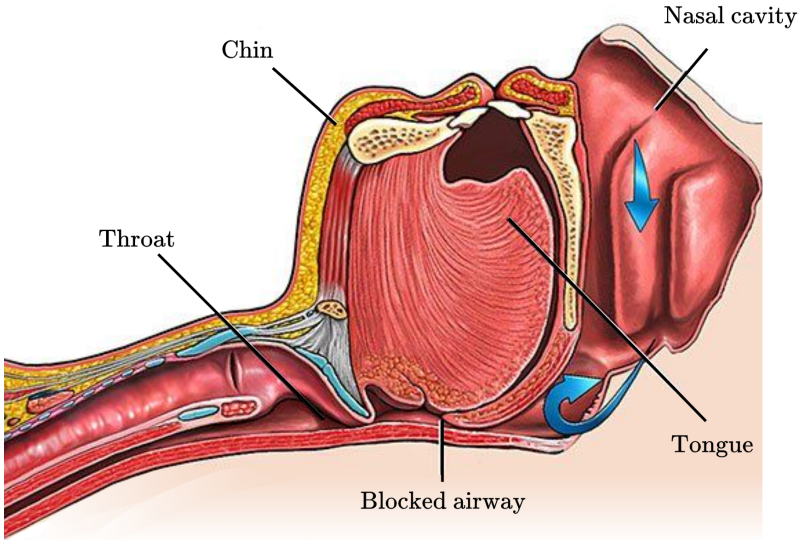

Figure 1.1: Representation of a collapsed airway [10].

1.1.1 The Human Respiratory System

The human respiratory system consists of two main sections; the airways and the lungs. Subdividing the respiratory system into these parts is common in terms of the physical location of the sections. However, it is not descriptive in terms of their functionality. Regarding the section's functions, dividing the system into a conducting zone and a respiratory zone is more useful. The conducting zone is the part where the air is transported to the lungs. In contrast, the respiratory zone handles the gas exchange between the incoming oxygen and the outgoing carbon dioxide [11, p. 567]. The mechanics relevant to OSA occur in the conducting zone; thus, this thesis will not discuss the respiratory zone further. The conducting zone can be subdivided into two sections; the upper and the lower respiratory airways. The upper respiratory airways are comprised of the nose, the nasal cavity, and the pharynx, which are depicted in Fig. 1.2. The lower airways consist of the larynx, the bronchial tree, and the lungs. This thesis will focus on the section which extends from the external nares and terminates in the lower part of the trachea.

1.1.2 Treatment of OSA

There are two main options for treating OSA, surgical and non-surgical approaches. The most common non-surgical treatment approaches are a combination of lifestyle changes, such as weight loss, increased physical activity, avoidance of alcohol and sedatives before going to sleep, and using positive airway pressure devices. The most common non-surgical devices are continuous positive airway pressure (CPAP) devices [13]. CPAP devices involve the use of a mask during sleep that introduces

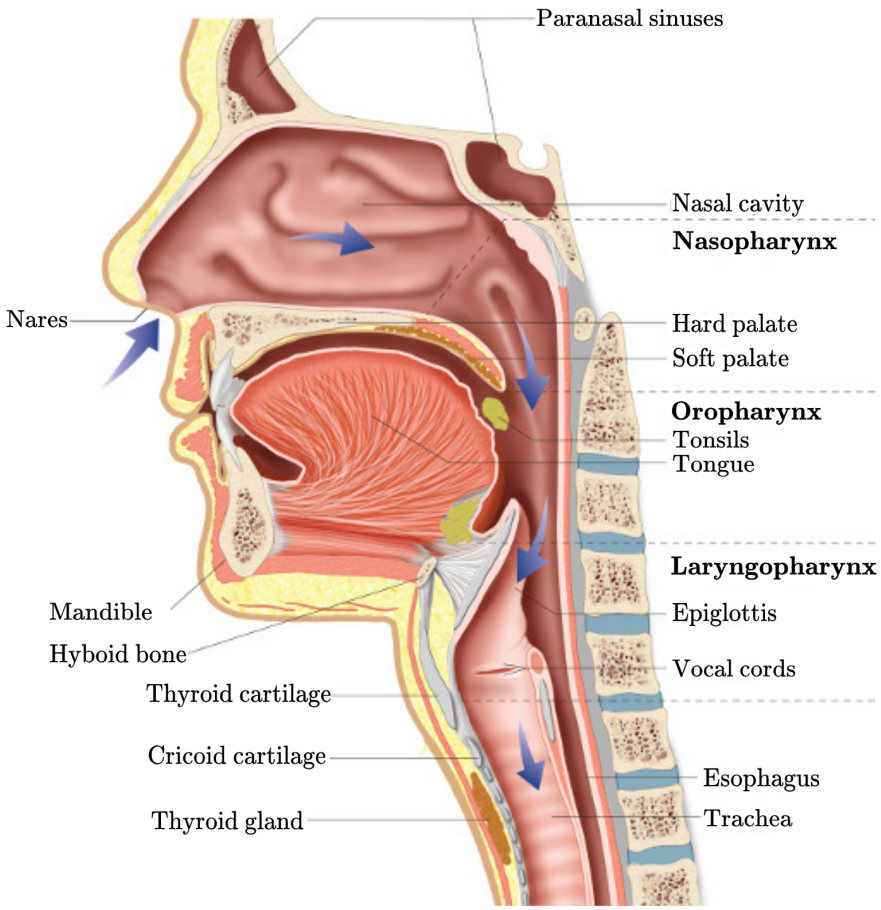

Figure 1.2: The anatomy of the human upper airways [12].

a greater-than-atmospheric pressure to the OSA patient's upper airways, reducing the chance of collapse. CPAP devices work well for treating OSA; however, they do not permanently solve the problem and require daily use. These devices are often uncomfortable and invasive for the patient; therefore, patient compliance is challenging. The issues regarding patient compliance with these devices are an important motivating factor for alternative treatment approaches. Commonly the alternative to the methods discussed is the implementation of surgical treatment. There are multiple surgical approaches to reduce collapses in the upper airways of OSA patients. Some of them involve altering the geometries of the upper airways, while other approaches improve airflow by bypassing the collapse regions. Common surgeries include alterations of the nose, the nasal cavity, or the soft palate [14], [15]. Surgery choice depends on the OSA's nature for each case.

1.1.3 Surgical Treatment of OSA

Surgery should be considered a treatment option only after an extensive presurgical evaluation due to the severity and invasive nature of the surgical processes. Surgical approaches for OSA either involve altering different anatomical regions in the upper airway to improve airflow and reduce the chance of pharyngeal collapse or bypassing the region of collapse entirely [16]. There are several definitions of surgical success

regarding OSA; however, it is commonly defined as a reduction in AHI by at least 50%, an AHI of less than 20 post-surgery or both [17]. Although this does not necessarily mean the patient's OSA is entirely resolved, it sets the standard for regarding a surgical intervention as successful. The following subsections review some of the most common surgical treatments for OSA.

Uvulopalatopharyngoplasty

Uvulopalatopharyngoplasty (UPPP) is one of the most common surgical procedures to reduce OSA [18]. The procedure involves altering the anatomy of the upper pharyngeal airspace, which is commonly the collapse site. Traditional UPPP involves removing redundant tissue in the soft palate and pharynx and removing the tonsils if they are present[15]. UPPP is often preferred if more conservative non-surgical procedures are not tolerable by the patient [19]. Despite the method's prevalence, success rates for UPPP are relatively low at around 50% [20].

Nasal Surgery

The flow in the nasal cavity contributes to the collapse of the upper airways in OSA patients. Therefore, nasal surgery is a common approach to reduce the prevalence of airway collapse. The septum, the nasal conchae, and the nasal valve are among the anatomical regions responsible for obstruction in the nasal cavity. Two common surgical procedures to reduce obstruction in these regions are septoplasty and turbinate reduction. A septoplasty involves correcting a deviated septum [21] while a turbinate reduction is the surgical reduction of the nasal conchae located in the nasal cavity.

Maxillomandibular Advancement

A common trait for patients diagnosed with OSA is the prevalence of maxillofacial skeletal abnormalities. Maxillomandibular advancement (MMA) is a surgical procedure involving advancing the mandible, the lower jaw, and the maxilla, the skeletal section of the upper jaw. The maxilla and the mandible are held in their new place using titanium plates. This procedure increases the airspace in the pharyngeal airway, thus decreasing the possibility of collapse [15]. MMA is considered the most effective OSA surgical procedure available, with a success rate of around 85% [22].

Tracheotomy

Tracheotomy is a procedure that bypasses the site of collapse entirely. Its surgical procedure involves creating an opening in the patient's trachea, where a tube is commonly connected, creating a breathing system independent of the nasal cavity. Although the procedure has high success rates [23], it is associated with an increased risk factor and unwanted side effects. Common complications regarding the

treatment include infections and the negative social implications of a visible breathing tube. Since there is a considerable negative impact compared to the benefits, tracheotomy is not commonly the first line of treating OSA.

1.2 Medical Imaging

Medical imaging is an integral part of the advances in modern medicine. There have been rapid advances within image processing in the past decades, like in other computational fields. These advances have contributed to the rise in medical image segmentation, which helps aid in virtually assessing different internal organs and body parts [24]. The nature of image processing in medical science makes it a good candidate for applying modern data-science techniques allowing the creation of applicable 3D models to aid in treating patients. Magnetic resonance imaging (MRI), ultrasound, and computed tomography (CT) scans are today's most common imaging methods. These techniques are fundamentally different in the physics they use to approach the creation of the medical images. However, they result in the same file format, DICOM (Digital Imaging and Communication in Medicine) [25]. From the study conducted by Moxness et al. [26] CT and MRI images of 78 patients with OSA were taken both prior to and post-surgery. These images are used in this thesis to extract patient-specific cross-sectional information.

Computed tomography (CT) is an imaging method for the internal parts of the human body. With X-ray as the technology behind the imaging, the output is a pseudo-three-dimensional array of numerical values, each representing a value of the Hounsfield units (HU). HU is the measure used in CT images of how much radiation is absorbed in the various organic material in humans. The resulting information is stored in a DICOM file. DICOM is the standard file format for the output of medical imaging procedures, including MRI, CT scans, and ultrasound [27]. DICOM is both the file format abbreviated to .dcm and a container for patient information by storing a three-dimensional array containing the intensity of each voxel in the medical image. Along with the voxel data, a great deal of information about the patient can also be included in the DICOM file, leading to a compact and useful file format. These files can be opened using specific file-handling software for these kinds of files, such as 3D Slicer [28], which will be discussed in further detail in Chapter 3. The CT images and their corresponding DICOM file form the foundation for the pragmatic model by providing the basis for further data processing, which eventually serves as the input for the pragmatic simulations.

1.3 Fluid Mechanics in Medicine

Even though medicine and engineering are two seemingly completely different fields of study, there are areas in which they coincide. Fluid mechanics is highly relevant to the mechanics of the human body. For example, the cardiovascular system pumps blood through the body using high pressure, and the lungs create a negative

gauge pressure for the inhalation of air and increase the pressure during exhalation. The possibilities for these two fields to work cross-disciplinary are vast, especially concerning the respiratory system. With the complicated airways and the amount of air being inhaled and exhaled, the fluid dynamics of the upper airways is essential to the occurrence of OSA. Therefore, it is essential to understand underlying physics to create a simplified model to help solve these problems.

1.3.1 Improvements and Modern Approaches

Over the past decade, the collaborative efforts behind VirtuOSA have been utilizing engineering and mathematical approaches to help understand and predict surgical outcomes [29]. One such approach has been to use computational fluid dynamics (CFD) to simulate the flow through the human upper airways and use the results from these simulations to understand airway collapses during sleep further. Even though CFD is a useful and powerful approach, it is limited by factors currently challenging to surpass. One limiting factor is the expertise needed to set up the simulations and validate the result to ensure their physical accuracy. Another limitation is the computational cost of running the simulations. Currently, there is no easy way to get highly accurate results quickly using CFD. This project aims to help fill the gap between CFD and obtaining useful results quickly. The further goal is for medical professionals to be able to import patient-specific data into an application and receive a report of the status of the patient's airways and what effect changes will have. This is meant to be used as an objective assessment device that will aid the doctor in deciding which treatment approach to take. This improves the reliability of surgical outcomes leading to fewer unnecessary and unsuccessful surgeries.

1.3.2 Approximating the Upper Airways as a Piping System

The basis of the pragmatic simulation model, created through the author's specialization project [1] is its potential to apply a well-known engineering approach to a complex problem and thus yield quick and valuable results. The engineering approach proposed is to model the human upper airways as a piping system. Using a piping system as an approximation allows for calculating the flow features through empirically tested pipe calculation tools, such as the Bernoulli equation with losses [30]. If the well-known and reliable tools can be applied, it will allow for the pressure calculations to be much quicker than the previously utilized CFD calculations.

1.3.3 Hydraulic diameter applied to the Human Upper Airways

In the study of nasal passage segmentation conducted by Al-Omari et al. [31], the hydraulic diameter was stated as playing an important role in the analysis of flow regimes in the upper airways. The study concluded that there are possibilities to

utilize the hydraulic diameter for aerodynamic calculations. Their method used the left nasal canal of patients and was focused on aiding in surgical planning. The present study aims to have a more pragmatic approach by combining both of the nasal passages into one hydraulic diameter and thus one single pipe. The goal of this combined system is to take the whole system into account while not losing any information to unknown factors, for example, the different flow rates in the two passages.

In industrial applications of the engineering approaches used by the pragmatic model, the pipes are in general considered to be circular. The models and the approximations created for flow calculations are all based on geometries being circular. Since it is common for piping systems to have non-circular sections, such as rectangular duct sections, it is possible to transform non-circular sections into circular ones. The most common transformation of this kind is known as the hydraulic diameter conversion. It converts the cross-sectional area and the wetted perimeter of a non-circular section into the section's equivalent diameter, given as $D_h = 4 \cdot \frac{A}{P_e}$, where A is the cross-sectional area and P_e is the wetted perimeter. This is commonly used to calculate the flow's Reynolds number and other length-related quantities. The proposed simulator converts the cross-sections of the human upper airways into pipes of equivalent hydraulic diameter and applies the engineering approaches described above.

The hydraulic diameter is a good way to convert rectangular ducts and other simple geometries into circular geometries. The cross-sectional shapes are simple through the pharynx to the trachea, and the hydraulic diameter is assumed to be reasonably accurate. However, with complex geometries, such as the ones in the nasal passages, its documented use is rare to the author's knowledge. Rarer still is combining two complex geometries to a single hydraulic diameter for further use in flow calculations. This was the approach used in the author's specialization project [1]. Verifying the approach's validity was outside that specialization project's scope. For the further development of the pragmatic model, this assumption needs to be verified to create a trustworthy simulator. A numerical test case has been proposed in this thesis to verify the use of the hydraulic diameter outside its intended application domain. The verification setup aims to determine whether the claim mentioned above is valid. If this is not the case, the goal is to create an equation for the hydraulic diameter that better represents the human upper airway geometries.

1.4 The Objective of this Thesis

With difficulty in predicting surgical outcomes being a limiting factor for success in OSA surgery, a tool to predict the outcome of surgery could be advantageous. Since there are limiting factors to CFD becoming a widespread predictive tool in medicine, other approaches might be better suited. The pragmatic model proposed in this thesis is a predictive system that aims to have the accuracy of CFD without the computational requirements or need for expertise. This thesis aims to develop a method of data extraction from CT images to provide input for the pragmatic model and improve the pragmatic model further. Although the surgical predictions

are an eventual aim pragmatic model, developing this aspect is outside the scope of this thesis. The objective of validating the hydraulic diameter used in the flow simulations is to validate its use on the human upper airways and propose a better-suited version.

1.5 Thesis Outline

In the present thesis, all mathematical models used for the 1D flow simulations are presented in Chapter 2 along with the governing equations of CFD used for validating the hydraulic diameter. The methods used for extracting data from CT images and the methods used for the 1D flow simulations are presented in Chapter 3. In Chapter 4 the methods behind the validation of the hydraulic diameter are presented. This is followed by the results, a discussion, and their corresponding conclusions. In Chapter 5 the results from various improvements implemented in the pragmatic model are presented and discussed, followed by their conclusions in Chapter 6. Future improvements to the present work and a general idea for the complete prediction system are discussed in Chapter 7.

Chapter 2

Mathematical Models

In this thesis, a pragmatic model for 1D flow simulations was further developed using the work from the author's specialization project [1] as a starting point. Another element investigated through this thesis is the use of the hydraulic diameter for the complex geometries of the human upper airways. The governing equations for both of these separate parts of the thesis are presented in this chapter.

2.1 Governing Equations for the Pragmatic Model

This section presents the mathematical models used to model the physics of the airflow in the human upper airways and is adapted from the author's specialization project [1]. The Bernoulli equation with losses has been used to create the main part of the pragmatic flow simulator. The Bernoulli equation, combined with additional losses, is a well-known engineering approach for modeling piping systems in a simplified way [32]. From the derivation of the equation, it is valid along a streamline and assumes a steady, incompressible flow where net frictional forces are negligible.

2.1.1 Bernoulli Equation with Losses

The Bernoulli equation with losses between two arbitrary points 1 to 2 along a streamline is given as [32, p. 199]

$$\frac{p_1}{\rho g} + \alpha_1 \frac{V_1^2}{2g} + z_1 = \frac{p_2}{\rho g} + \alpha_2 \frac{V_2^2}{2g} + z_2 + h_L \tag{2.1}$$

where p_1 and p_2 are the pressures and V_1 and V_2 are the velocities at point 1 and 2 respectively. z_1 and z_2 correspond to the height of each point, while α_1 and α_2 are the kinetic energy correction factors. ρ is the density of the fluid and g is the gravitational acceleration. h_L is the loss term which accounts for irreversible losses in the equation. Through solving (2.1) for the pressure at point 2 and substituting in an index notation, the pressure is given as

$$p_i = p_{i-1} + \rho \frac{\alpha_{i-1} V_{i-1}^2 - \alpha_i V_i^2}{2} + \rho g (z_{i-1} - z_i) - \rho g h_L. \tag{2.2}$$

where $i-1$ and i refer to cross-sections along the same streamline. In the pragmatic model, this pressure corresponds to the gauge pressure, as the starting pressure is assumed to be atmospheric.

2.1.2 Volumetric Flow Rate

Since the velocity is one of the input variables in Eq. (2.2), it needs to be obtained. Since the flow rate, Q, is known, the velocity can be calculated using the incompressible volumetric flow rate equation, which is given as

$$Q = V_i A_i = \text{constant}. \tag{2.3}$$

In this equation V_i is the velocity and A_i is the cross-sectional area of cross-section i.

2.1.3 Major Losses

An essential assumption for using the Bernoulli equation is the assumption of negligible frictional forces. This is a reasonable assumption for certain flow situations and is valid along a streamline. However, this assumption is not valid in the case of an internal flow such as a pipe flow or a flow through the human upper airways. This is due to the shear stresses along the walls of the airways and the losses due to flow separation and other occurring flow structures. There are several reasons why the flow separates; one of them is due to changes in the geometry which commonly leads to backflow and causes additional losses. The frictional losses are included through the term h_L in Eq. (2.2) and are given by

$$h_{L,major,j} = f_j \frac{\Delta L_j}{D_{hj}} \frac{V_j^2}{2g} \tag{2.4}$$

where the subscript j denotes the sectional index along the geometry. A section j corresponds to a section beginning at $i-1$ and ending at i from Eq. (2.2). ΔL_j is the length of section j and $D_{h,j}$ and V_j are the hydraulic diameter and velocity for section j respectively. They are obtained by calculating the corresponding average values from cross-section $i-1$ and i. The velocity for section j is obtained by

$$V_j = \frac{V_{i-1} + V_i}{2}, \tag{2.5}$$

and the hydraulic diameter for section j is given by

$$D_{h,j} = \frac{D_{h,i-1} + D_{h,i}}{2}. \tag{2.6}$$

In Eq. (2.4), f_j is the Darcy friction factor and is given as

$$f_j = \frac{64}{\mathrm{Re}_{avg,j}}, \tag{2.7}$$

for a laminar pipe flow. In Eq. (2.7), $\mathrm{Re}_{avg,j}$ is the average Reynolds number for section j and is obtained by

$$\mathrm{Re}_{avg,j} = \frac{\mathrm{Re}_{i-1} + \mathrm{Re}_i}{2}, \tag{2.8}$$

where the Reynolds number at cross-section i is given by

$$\mathrm{Re}_i = \frac{\rho V_i D_{h,i}}{\mu}. \tag{2.9}$$

In Eq. (2.9), ρ is the air density, μ is the dynamic viscosity, V_i is the local velocity and $D_{h,i}$ is the hydraulic diameter of the respective cross-section. Since Eq. (2.7) at location i assumes a constant diameter, the Reynolds number used in the equation has been averaged over the section of the geometry,

2.1.4 Minor Losses

Along with the major losses presented in section 2.1.3 there are losses caused by changes in the geometry. These losses are known as minor losses. Minor losses include expansions, contractions, bends and other changes in the pipe geometry [30]. The general equation for this additional loss term is given as

$$h_{L,minor} = K_{L,j} \frac{V_j^2}{2g} \tag{2.10}$$

where j is the sectional index where the loss occurs and $K_{L,j}$ is the minor loss coefficient for the same section.

The Loss Coefficient K_L for Sudden Expansions and Contractions

The most common changes include expansions, contractions and bends, which have known equations and loss values associated with them for piping systems. The main varieties that the upper airways consist of and are included in the pragmatic model will be presented in this section. The equation for a sudden expansion is given by [30, p. 388]

$$K_L = \alpha \left(1 - \frac{d^2}{D^2}\right)^2, \tag{2.11}$$

where d is the hydraulic diameter of the smaller cross-section and D is the hydraulic diameter of the larger cross-section, α is the kinetic energy correction factor. For all of the pragmatic simulations in this thesis $\alpha = 1$ has been assumed, both for the minor loss equations and the Bernoulli equation with losses, Eq. (2.2). For a sudden contraction the following equations are given [30, p. 388]

$$K_L \approx \begin{cases} \alpha \cdot \left(0.42\left(1 - \frac{d^2}{D^2}\right)\right) & \text{for } \frac{d}{D} \leq 0.76 \\ \alpha \cdot \left(1 - \frac{d^2}{D^2}\right)^2 & \text{otherwise} \end{cases} \tag{2.12}$$

The Loss Coefficient K_L for Gradual Expansions and Contractions

In the cases where gradual contractions and expansions occur table values are given, they are presented in Tab. 2.1 for gradual expansions and 2.2 for gradual contractions. The value for a specific case was found by interpolating the table values.

Table 2.1: Minor losses for a gradual expansion, $\theta = 20°$ [32, p. 367].

d/D	K_L
0.2	0.30
0.4	0.25
0.6	0.15
0.8	0.10

Table 2.2: Minor losses for a gradual contraction [32, p. 367].

θ	K_L
30°	0.02
45°	0.04
60°	0.07

2.1.5 Hydraulic Diameter

Noncircular geometries do not have an explicit diameter, from their nature. To use the relations presented in section 2.1.3 and section 2.1.4 a conversion is required. The hydraulic diameter is a common conversion for noncircular geometries, and for a duct and other simple geometries, it is given as [30, p. 374]

$$D_h = 4 \cdot \frac{A}{P_e}, \tag{2.13}$$

where A is the cross-sectional area of the geometry and P_e is the wetted perimeter of the same cross-section. This equation is not meant for complex geometries such as the ones in the human upper airways. An alternate version has therefore been proposed. The proposed alteration of the hydraulic diameter is given as

$$D_h = C_{D_h} \cdot \frac{A}{P_e}, \tag{2.14}$$

where C_{D_h} is the "hydraulic diameter coefficient" which replaces the constant 4 in the Eq. (2.13).

2.1.6 Diffuser

Although the loss coefficient found in Eq. (2.10) includes losses that occur due to gradual and sudden expansions, results from the pragmatic simulations show that additional loss modeling may be required in these regions. These additional losses due to flow separation can be modeled as a pressure-recovery coefficient given as [30, p. 398]

$$C_p = \frac{p_e - p_t}{p_{0t} - p_t}, \tag{2.15}$$

where p_e and p_t are the pressure at the exit and throat of the diverging nozzle, respectively, and p_{0t} is the stagnation pressure at the throat. To include this as an additional loss, it can be solved for p_e after obtaining a value for C_p and adding it to Eq. (2.2). In this equation, throat and exit refer to the inlet and the outlet of a section of pipe, respectively.

2.1.7 Governing Equations for CFD

To validate the use of the hydraulic diameter in the upper airways of OSA patients, a benchmark test case has been proposed. For the computation of the test case, the commercial CFD software Ansys Fluent [33] was used. In Ansys Fluent, the Navier Stokes equations are solved using the finite volume method on a discretized mesh. For each cell, the continuity equation and the momentum equation, which make up the Navier-Stokes equations, are solved. Since the Mach number is much lower than 0.3, the incompressible variants of the equations have been solved. The incompressible continuity equation is given by

$$\frac{\partial u_i}{\partial x_i} = 0 \tag{2.16}$$

where u_i is the velocity component in the $x_i -$ direction where $i = 1, 2, 3$. The incompressible momentum equation is given by

$$\frac{\partial u_i}{\partial t} + u_j \frac{\partial u_i}{\partial x_j} = f_i - \frac{1}{\rho}\frac{\partial p}{\partial x_i} + \nu \frac{\partial^2 u_i}{\partial x_j \partial x_j} \tag{2.17}$$

f_i is the i^{th} component of the gravitational acceleration, where $i = 1, 2, 3$. ν is the kinematic viscosity, which is a constant for this case. The Einstein summation is assumed for equations (2.16) and (2.17).

Chapter 3

Method

3.1 Introduction to the Pragmatic Model

Parts of this chapter are adapted from the author's specialization project [1]. The author's specialization project [1] included developing a pragmatic model for predicting area-averaged gauge pressure through the human upper airways of OSA patients. The proposed pragmatic model had three main components: its input, the 1D flow simulations, and its output. In the specialization project, the code for the 1D flow simulations was the main focus of attention and contributed to a solid foundation for the present thesis. This thesis aims to improve the model's accuracy while expanding its scope to make it a complete system for flow predictions. In the specialization project, the model's input was extracted from the pre-existing 3D geometries presented in section 3.3.4. A system for extracting and preparing patient-specific data for the 1D flow simulations is proposed in this thesis to further the development of the pragmatic model. In section 3.2 this method is presented; it involves creating 3D models from patient-specific CT images and extracting cross-sectional data from the 3D models. Improvements have been made to the 1D flow simulations and their interconnection with the extracted cross-sectional data. The 1D flow simulator is presented in section 3.3 and its solution algorithm is outlined in section 3.3.6. The third component of the pragmatic model is its output, presented as the area-averaged gauge pressure at the locations indicated by the input. These results can further be used in surgical treatment predictions. However, this will not be further investigated as it is outside the scope of this thesis. These three components provide the complete pragmatic model, which encompasses the processing of CT images to create flow predictions and are presented in this Chapter.

3.2 Data Extraction

The input of the flow simulation part of the pragmatic model is the cross-sectional data from patient-specific CT images. The data of interest is the cross-sectional area and the wetted perimeter of a sufficient number of cross-sections through the pa-

tient's upper airways. An automatic image segmentation procedure was considered to extract the cross-sectional data from the CT images. The method would use image segmentation libraries in Python [34] to provide a clean input which could further be used in the flow simulations. With the complex geometry of the nasal cavities, this turned out to be more challenging than expected. Therefore, an alternate approach was devised. The chosen extraction method involves the use of the CT-image segmentation software 3D Slicer [28]. 3D Slicer was used to create a 3D model of the patient's airways, which could be prepared for further use in the 3D editor Autodesk Meshmixer [35] through cleaning imperfections in the model. From the cleaned 3D geometry, the cross-sections of interest could be extracted and were used as the input of the 1D flow simulator.

3.2.1 Processing Medical Images and Automatic Segmentation

As mentioned in the introduction of Chapter 3.2 above, automatically extracting the cross-sections with self-developed code was abandoned. However, the progress made through the exploratory phases of this development is worth mentioning. The progress gained will be briefly outlined in this section. With the digital image processing capabilities available through the many libraries of Python, it is possible to create an automatic segmentation tool, several of which have been made to create a 2D representation of the lungs and lower airways. The first step of the image segmentation process was creating processable images and converting the CT images into usable data. Their data types are Nifti and DICOM, most commonly, the initial images are stored in DICOM format. The DICOM format was chosen for continued segmentation due to the files being in this format initially . The data in the DICOM format was then usable for image segmentation and viewing in the chosen 3D array of HU unit values. With a 3D array obtained, any slice of the CT-imagine could be viewed, and various thresholding could be applied to get the desired range. The airways can be segmented with the correct thresholding applied to obtain the range of the airways. Calculations of the cross-sectional area and the surrounding perimeter can be determined from these. Thus automatically creating the input of the 1D flow simulator.

3.2.2 Creating a 3D Model of the Airways

The first step in creating the cross-sectional input of the flow simulator is to create patient-specific 3D models. The first exploratory methods used involved more self-developed code, while the chosen approach uses available open-source and commercial software. In this section, an outline of the extraction process is presented. The software application used for the initial extraction was 3D Slicer [28]. 3D Slicer offers a complete platform for viewing, editing, and segmentation of medical images, along with other functionality. The first step is to load the desired DICOM file into the program, allowing the user to view the CT images. The CT images can be viewed in the three spatial directions allowing the user to obtain full access to the

CT image. Any patient-specific data included in the DICOM file can be accessed along with the images themselves. From the initial viewing of the CT scans, 3D Slicer provides a large variety of editing and data-extraction possibilities. The functions and tools related to image segmentation and creating 3D models are the most relevant to this study. The upper airway segmentation process can be initialized after choosing the user's preferred CT image. 3D Slicer includes several image recognition algorithms along with plenty of possibilities for segmenting different parts of the human body. The method used to segment the airways is an improved version of the grow-cut algorithm developed by Zhu et al. [36]. To use the method, the user marks sections of the organ to be segmented along with the background as a separate segmentation. This allows the algorithm to detect sections of the CT scan where the pixels have the same HU value and grow into a complete 3D model. This initially yields a crude but visually accurate representation of the 3D human upper airways, which can be edited through a manual iterative process. Fig. 3.1 shows a screenshot from the slicer viewing window after the completed segmentation process. When a reasonably accurate 3D representation is obtained, the 3D model is exported as a stereolithography (STL) which is ready to be cleaned further, as the model contains unwanted artifacts and noise.

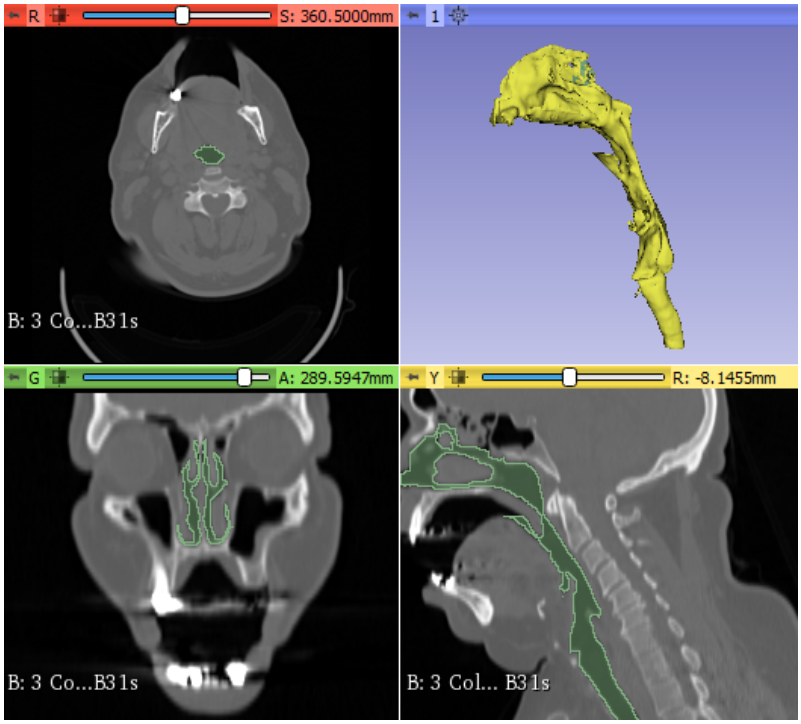

Figure 3.1: Screenshot from the viewing window in 3D slicer, after the segmentation procedure is completed for patient 6. The green areas in the figure are the segmented airways. The top left window shows the CT image in a top-down view, while the lower-left and lower-right windows are from the front and side, respectively. The top-right window shows the 3D model resulting from the extraction procedure.

3.2.3 Removing Noise from the 3D model

The imperfections in the 3D model can be cleaned up using the Autodesk Meshmixer [35], a 3D editing and drawing application used to prepare models for 3D printing. In Meshmixer, a function to remove unnecessary artifacts from the 3D model can be applied, leaving the 3D model as a single body. Further drawing and editing functions can be used to add material where sections are incomplete and remove material where there are uneven parts. Fig. 3.2 shows the result of the cleaning processes for Patient 6 from the study performed by Moxness et al. [26]. From this stage, the model can again be exported as an STL file, ready for cross-section extraction.

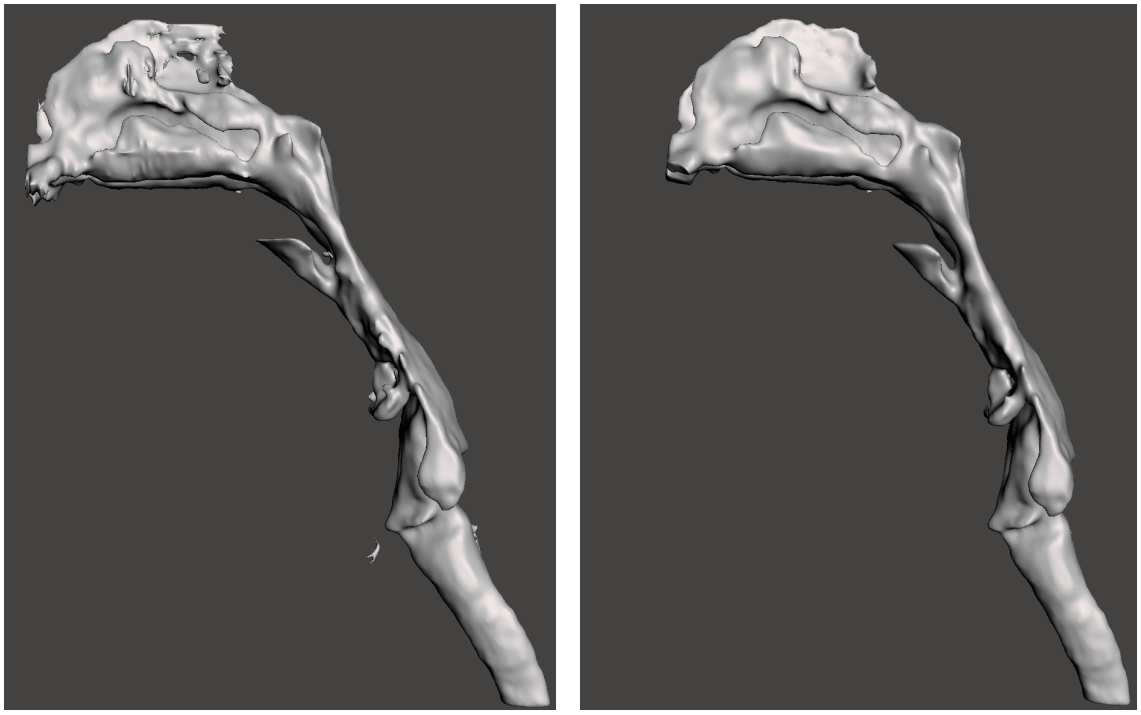

(a) Before cleaning (b) After cleaning

Figure 3.2: Patient 6's pre-surgical airway before and after the cleaning procedure in MeshMixer.

3.2.4 Extracting Cross-Sections from 3D Models

After obtaining a 3D version of the upper airway geometry, the cross-sectional data of interest to this study can be extracted. The extraction is done using the computer-aided design (CAD) program Ansys SpaceClaim [37]. In SpaceClaim, the locations of the cross-sections were found by matching the location and geometry of the cross-sections in Fig. 3.5. The procedure for extracting cross-sections is presented in the following subsections.

Obtaining Cross-Sectional Data

A reference plane is set at the default origin after the STL file has been opened. Another plane can be created parallel to the original plane, and the distance between the two planes can be measured and controlled precisely. The positions of both the plane located at the origin as well as the measurement plane are visualized in two dimensions in Fig. 3.4. In Fig. 3.4 the vertical plane represents the plane used for cross-sectional extraction in the nasal cavity, while the horizontal plane was used to retrieve the cross-sections from the pharynx to the trachea. The cross-sections' positions were found through comparison with Fig. 3.5. From Aasgrav's master's thesis, [38] the area-averaged gauge pressure was extracted from these cross-sections as a result of CFD simulations of patient 12's airways. Therefore using these cross-sections as input for the pragmatic model yields a comparable case for verification, further presented in Section 3.3.4. The plane used for obtaining these locations was placed either by manually pulling the plane or entering a distance from the origin plane. A combination of the two methods was used to achieve the best results. Although the method requires visually comparing the two cross-sections, the unique features of each cross-section in the upper airways make the comparison possible. This procedure resulted in an accurate re-creation of the cross-sections. For other OSA patients' airways, a more pragmatic approach was used, which involved matching the locations best possible to achieve a comparable case. When a cross-section had been located with a plane in SpaceClaim, the entire geometry could be split up at that location, creating two smaller 3D geometries. This revealed the cross-section at the split location. From the resulting cross-sections, both the cross-sectional area and the perimeter of the cross-section could be measured using built-in measuring tools.

Measuring the Distance of Sections with Bends

For the sections with bends, the procedure is less straightforward. Fig. 3.3 shows a representation of a section with a bend. The figure is a simplified version of the actual airway geometry, where the hydraulic diameter has not been applied. $r_{i-1,1}$, $r_{i-1,2}$, $r_{i,1}$ and $r_{i,2}$ are the radii at the relevant locations and were averaged to obtain an average radius, $\overline{r}$. This radius was used to calculate the length of the arc to obtain the distance between the two cross-sections ΔL.

The cross-sectional data and the distance to each can then be manually input into a Microsoft Excel [39] spreadsheet for further processing.

3.3 1D Flow Simulations

The main component of the pragmatic model is the 1D flow simulator. The simulation code provides fast upper airway simulations, where patient-specific cross-sectional data is used as the input. Discretization is done one-dimensionally, where the input and the volumetric flow rate given by Eq. (2.3) provide the boundary con-

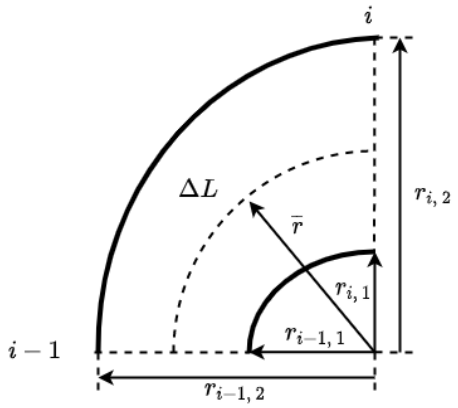

Figure 3.3: A simplified representation of a 90° bend in SpaceClaim. The distance between cross-section $i-1$ and i, which will be used in the 1D flow simulations, is given by ΔL. The different radii represent physical distances measured in SpaceClaim, used to calculate the mean radius, $\bar{r}$ which is further used to calculate the mean arc distance, ΔL.

ditions for each cell. With several of the parameters through the simulation domain already known, the quantity of interest is the area-averaged gauge pressure, which can aid in describing the flow through the upper airways. When the area-averaged gauge pressure is obtained, the state of the patient's upper airways can be analyzed further.

3.3.1 The Airways as Piping System

In the flow simulator the Bernoulli equation with losses, Eq. (2.2), is implemented. The pressure calculations begin at the nasal inlet, and the area-averaged gauge pressure for each of the following cross-sections is calculated using the pressure of its neighboring upstream cross-section. Fig. 3.8 shows an arbitrary section of an OSA patient's upper airways, where cross-section i's pressure is to be calculated using the properties from cross-section $i-1$, which already are obtained. Without implementing additional losses, Eq. (2.2) only depends on the pressure at cross-section $i-1$ and the velocity, yielding a far too general result, not valuable for a patient-specific analysis. Therefore, the additional irreversible losses need to be modeled in the flow simulations. The two contributions to the irreversible losses in the Bernoulli equation with losses (2.2) are the minor and the major losses. These losses have known equations and empirical values for piping systems. To apply these equations and empirical values to the human upper airways, they need to be converted into a system of pipe sections. This conversion is implemented by employing the hydraulic diameter [32, p. 340]. The hydraulic diameter can be obtained by applying Eq. (2.13) using the cross-sectional area and perimeter of each cross-section as input. Fig. 3.6 shows a representation of this conversion for a cross-section in patient 12's pre-operative nasal cavity. The irreversible losses can be calculated when the hydraulic diameter for each cross-section is obtained. In Chapter 4 this conversion has been validated for the cross-sections in the nasal cavity.

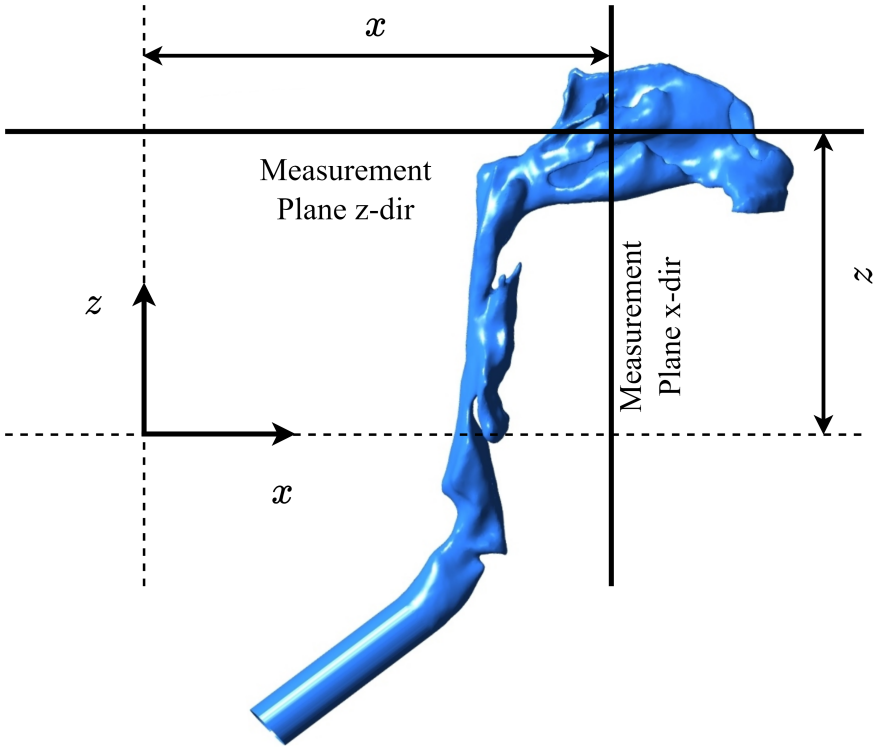

Figure 3.4: The measurement process in SpaceClaim for the extraction of the cross-sections. The dotted line is the base plane, while the planes used for measuring and dividing the geometry are solid lines. The x and z coordinates were further used to determine the distance between sections.

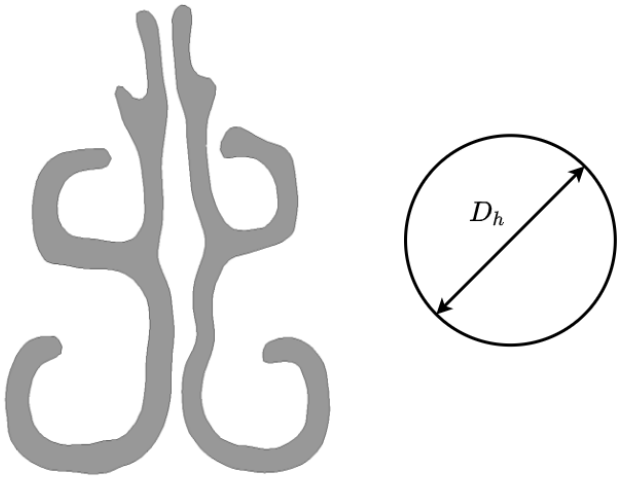

Figure 3.6: Conversion of cross-section number 3 from Fig. 3.5a to its circular counterpart using the hydraulic diameter.

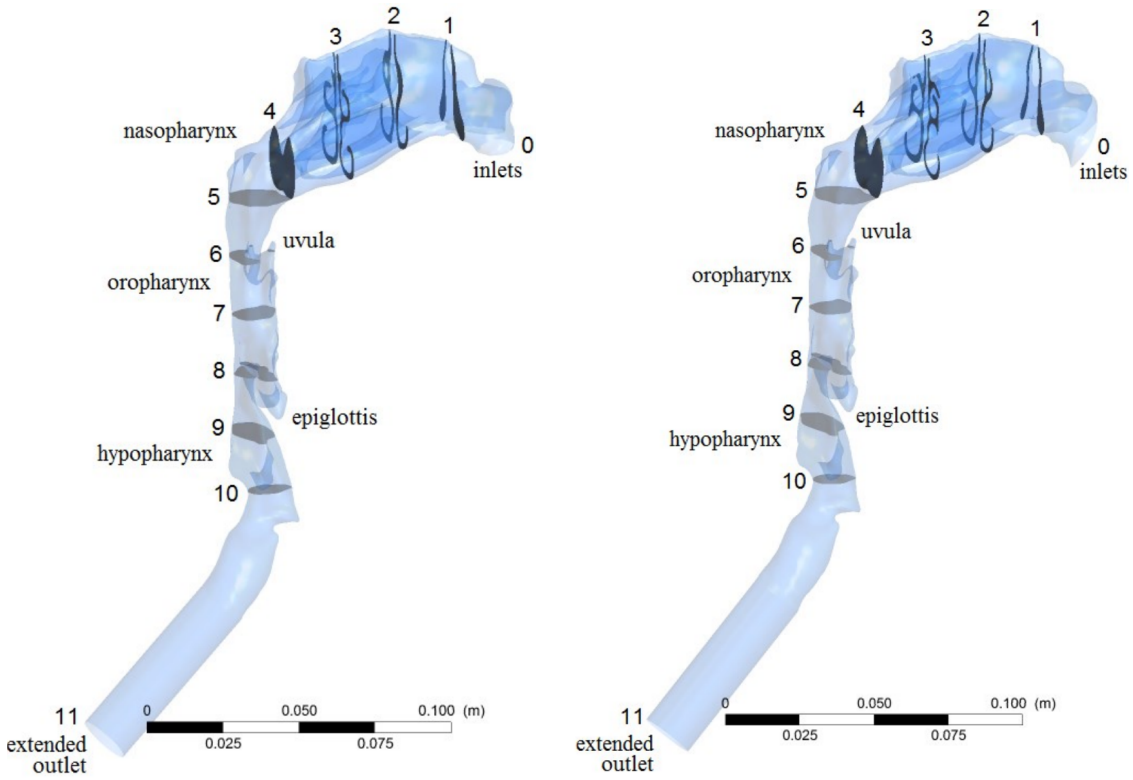

(a) Pre-operative (b) Post-operative

Figure 3.5: Location and numbering of the cross-sections in pre and post-operative geometries of patient 12. Figures are taken from Aasgrav's master's thesis [38]

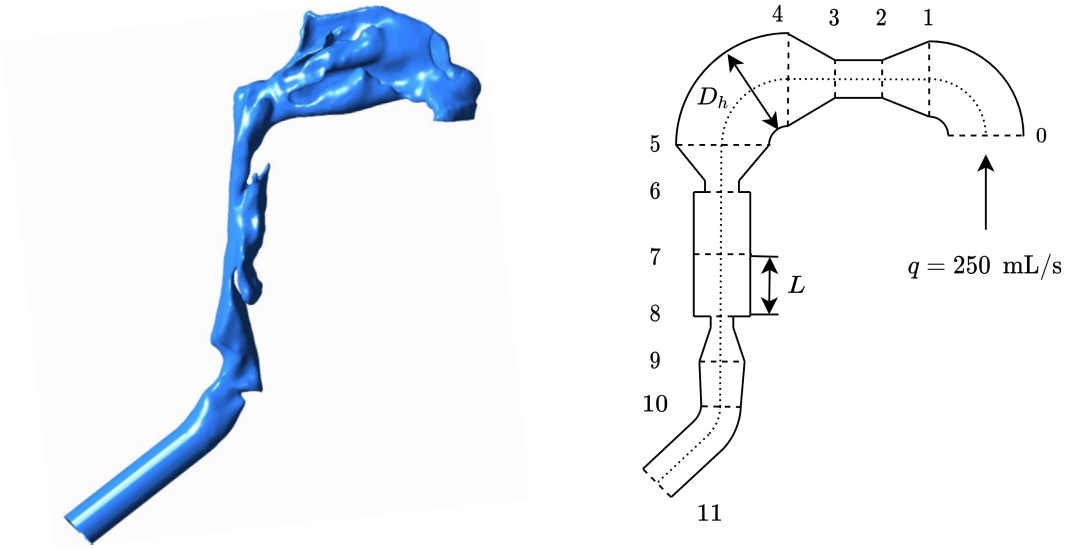

(a) 3D airway model (b) Piping representation

Figure 3.7: Fig. 3.7a [40] shows a 3D model of patient 12's airways and Fig. 3.7b shows its corresponding piping representation.

3.3.2 Modeling Irreversible Losses

There are two main loss contributions to the irreversible losses h_L in equation (2.2), they are the minor and the major losses. Changes in the geometry cause minor losses, while major losses are caused by friction along the walls. The simulator evaluates the various possibilities for losses based on geometrical changes. These losses can then be calculated and are further used to calculate the pressure. A detailed outline of the solution algorithm is further described in Section 3.3.6. The calculation procedures for the various irreversible losses are presented in the following subsections.

Minor Losses

To calculate the minor losses' contributions to the area-averaged gauge pressure, the loss coefficient, K_L, must be estimated for each section. Since the flow structures are different for various pipe components, they contribute differently to the losses. The general outline of the different pipe components is shown in Fig. 3.7. Sudden expansions and contractions are found by Eq. 2.11 and Eq. 2.12 respectively. The gradual expansions are found by interpolating the values in Table 2.2 and Table 2.1. Whether the geometrical change is sudden or not is determined by the user, as the algorithm cannot determine this on its own. For all of the expansion and contraction cases, the velocity used for calculating the minor loss $h_{L,minor}$ is the largest velocity from the two cross-sections, i.e., the velocity at the cross-section with the smallest diameter. In the literature, the loss coefficient for bends is highly variable. Therefore, they have been estimated based on Table 6.5 in [30, p. 385]. The resulting coefficients used were $K_L = 0.3$ for 45° bends and $K_L = 0.5$ for 90° bends.

Major Losses

The length of each section and the corresponding mean Reynolds number needs to be calculated to determine the major loss' contribution to the area-averaged gauge pressure. The Reynolds number at each cross-section is calculated using Eq. 2.9. The obtained Reynolds numbers are further used to calculate the mean Reynolds number using Eq. 2.8. With the mean Reynolds number obtained the friction factor, f, could be found using Eq. (2.7). To calculate the distance ΔL from cross-section $i-1$ to i the distance from the nasal inlet to cross-section $i-1$ is subtracted from the distance from the nasal inlet to cross-section i. The distance and the friction factor, along with the mean velocity and hydraulic diameter, were then used to calculate the major losses $h_{L,major}$ using Eq. (2.4).

User-Added Losses

Even though the simulation algorithm can detect a wide array of various irreversible losses that need to be taken into account, there may be losses due to factors that

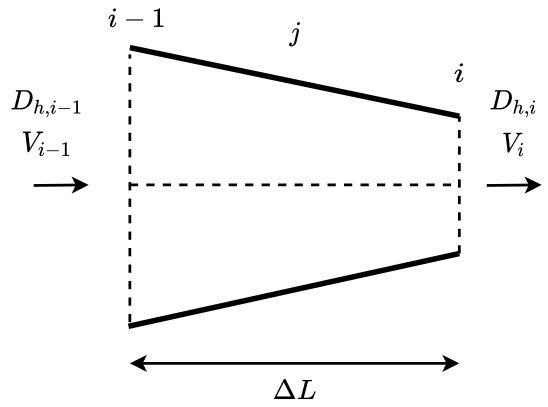

Figure 3.8: An arbitrary section of an OSA patient's upper airways after its conversion to a piping system which is used in the flow simulations. Index i is the cross-sectional index of a section, while index j is the sectional index for calculation of properties which take place between the cross-sections. ΔL is the distance between cross-section $i-1$ and cross-section i.

cannot be found for various reasons. The modular nature of the code allows additional losses to be added either prior to the simulations or at a later stage. These are losses that can be found through further analysis of the CT images or the 3D model. When the losses are found, they can be added to the simulation, and the losses will be taken into account. This allows the doctor or any other user to add to the automatically generated results, leading to much more accurate flow predictions. When the user is satisfied with the simulation results, they can be used in the assessment of procedure choice.

3.3.3 Flow Simulation Results

The code offers a wide variety of visualization options between simulations, for example, area-averaged gauge pressure plotted with the cross-section number or the distance from the nasal inlet. Apart from plots, the results can also be viewed as a table with all required relevant data, plus any desired user-defined data. The rapid result retrieval helps the user quickly analyze the simulation results and make informed adjustments. Informed adjustments could be made on the basis of additional data such as rhinomanometry data or other experimental data. When the simulations are tuned, the results can be extracted from the simulation. With the results ready, a decision on the correct way to proceed can be made, along with the professional opinion of a medical professional.

3.3.4 Choice of Verification Case

A verification case was required to assess the accuracy of the pragmatic model. The 3D models used for the input and further validation of the pragmatic model were created using the open-source software ITK-Snap [41]. Creating these 3D models is described in Jordal's specialization project [40] and master's thesis [42].The

models were retrieved from CT images of patient 12 in the OSA study, a male born in 1948 who made significant post-surgery improvements. CFD simulations were performed using the same 3D models through Aasgrav's specialization thesis [43] and master's thesis [38]. Fig. 3.9 shows the results of both the pre-and post-operative simulations. The results show the area-averaged gauge pressure plotted against the cutplane number. The cutplane number refers to the numbering scheme used in Fig. 3.5, where cutplane number 0 is located at the nasal inlet, and cutplane 11 is in the trachea. Since the results from Aasgrav's CFD simulations [38] were presented in this format, this was also chosen as the result format for the pragmatic simulations. This approach yields a way to assess the pragmatic simulation results directly and comparably. Although this yields a relevant result to compare the pragmatic simulations to, it is not comparable for all of the cross-sections. The CFD simulations were performed using Ansys Fluent [33], and the results were further extracted using Ansys postprocessing tools. The highlighted sections of Fig. 3.5 shows the cross-sections used when extracting the area-averaged gauge pressure curves shown in Fig. 3.9. For cross-section number 8, the highlighted region is extended to include parts of the oral cavity in front of the epiglottis. This is an area that contributes to the calculation of the area-averaged gauge pressure, even though it does not contribute to airflow. In the author's specialization project this was a cross-section with large deviations when compared to the pragmatic model, which could be caused by the increased calculated domain from Fluent. When assessing the accuracy of the pragmatic model in the present thesis, comparing the results from the pragmatic model to the CFD simulation at cross-section number 8 has therefore been excluded.

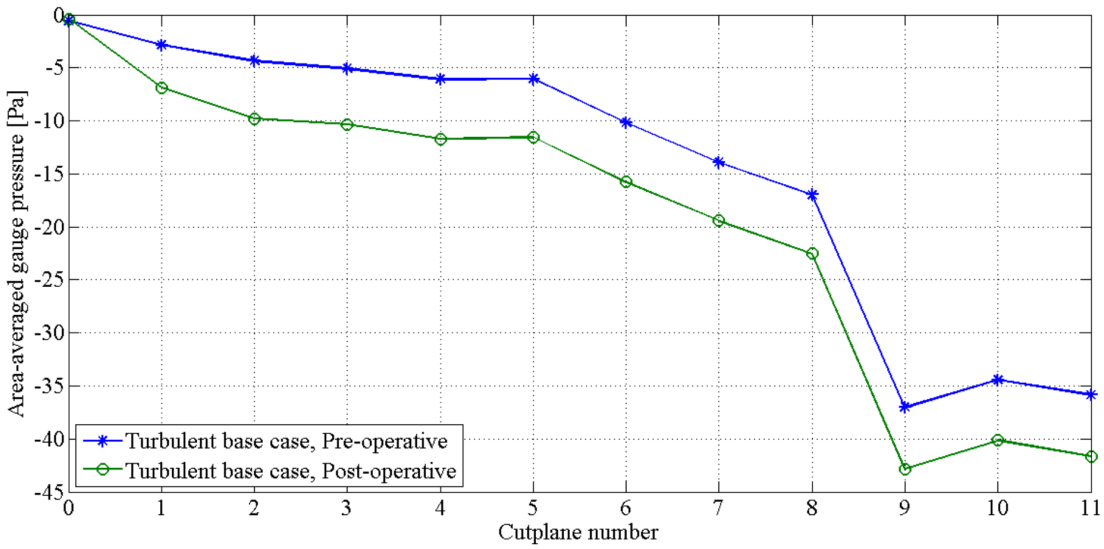

Figure 3.9: Pre and post-operative results of turbulent CFD simulations of patient 12 [38].

3.3.5 Assessing the Accuracy of a Simulation

To find the deviation between the results from the pragmatic model and the results from the CFD investigations, given in Fig. 3.9, a statistical comparison technique

Table 3.1: Pre-operative data extracted from the 3D model of patient 12's upper airways used as the input of the pragmatic model. Table adapted from [1]

Cutplane no.	Cross-sectional area [mm^2]	Perimeter [mm]	Distance [mm]
0	268.89	94.49	0.00
1	225.59	136.79	26.76
2	306.03	287.86	48.76
3	326.94	322.08	66.76
4	401.70	86.28	84.96
5	290.00	62.79	111.72
6	101.38	47.00	131.72
7	189.61	50.83	151.72
8	44.01	30.39	176.72
9	189.55	58.38	186.72
10	170.93	49.69	191.72
11	94.19	40.54	200.22

was applied. The residual sum of squares (RSS) was used to optimize the hydraulic diameter and indicate the difference between the curves objectively by finding the deviation between the pragmatic simulations and the pre-obtained data. The equation for RSS is given as [44]

$$\mathrm{RSS} = \sum_{i=1}^{n} (y_i - f(x_i))^2, \tag{3.1}$$

where y_i is the i^{th} component of the value to be predicted (the area-averaged gauge pressure from CFD simulation) and $f(x_i)$ is the i^{th} component of the predicted value (the area-averaged gauge pressure from the pragmatic model).

3.3.6 Outline of the Solver

In this subsection, the solution algorithm and its decision-making processes are described. This outline closely follows the flowchart presented in Fig. 3.10. The solution algorithm has been implemented using Python [34] and is included in Appendix B.

Input

Prior to beginning the solution algorithm, the input needs to be included. The pragmatic model is designed to take input as a DataFrame, an object format commonly used in the Python library Pandas [45]. The DataFrame includes the cross-sectional area, the perimeter, and the distance from the nasal inlet to each section. The input for the pragmatic simulations of patient 12's pre-operative geometry is included in Table 3.1.

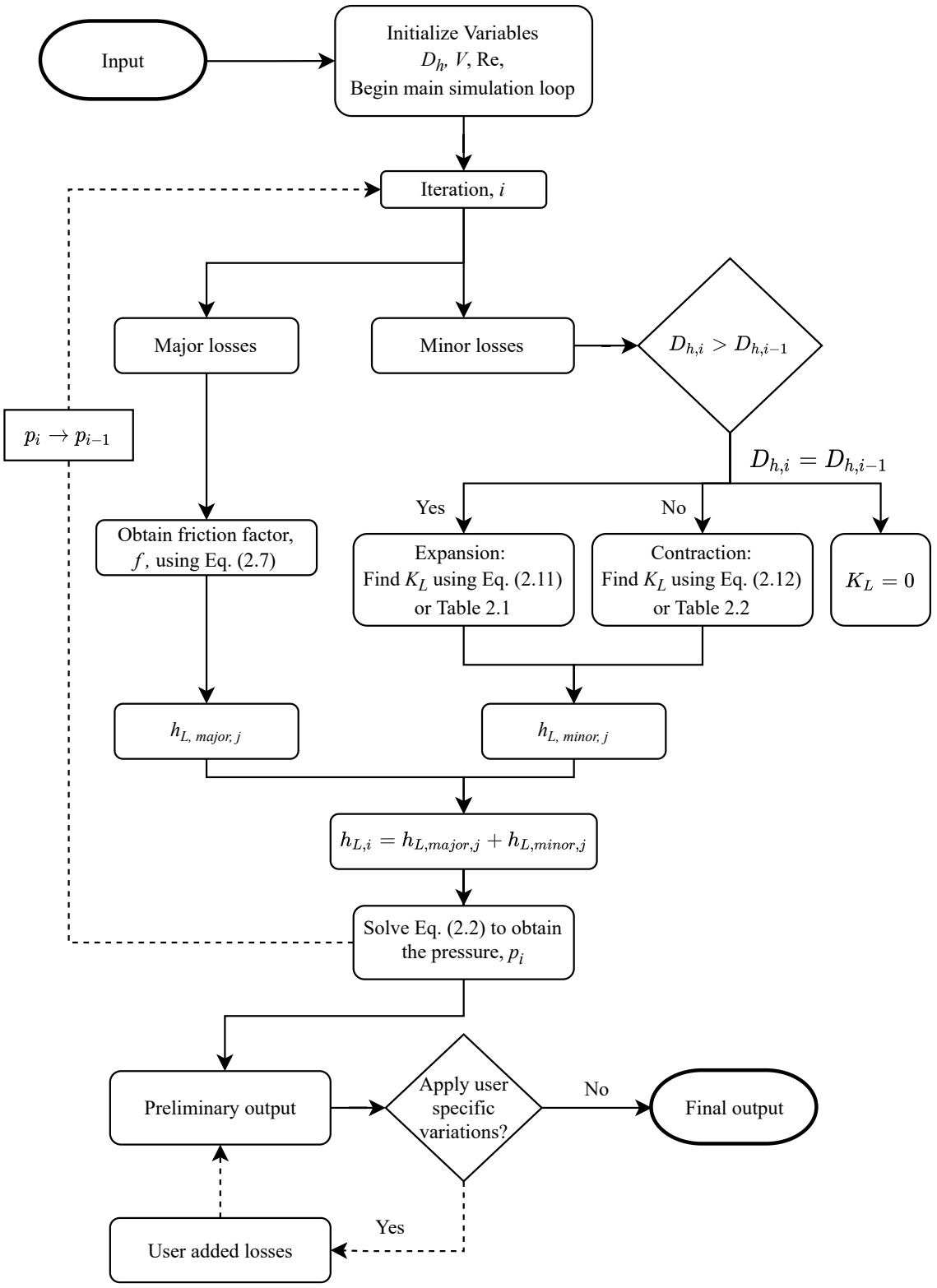

Figure 3.10: Flowchart outlining the pragmatic model's solution algorithm.

Step 1: Initialize Variables and Begin Main Solution Loop

Before the main simulation loop begins, the hydraulic diameter, D_h, the velocity, V, and the Reynolds number corresponding to each section are calculated. These variables are stored in a similar format to the input described above for simple access during the simulations. When the relevant parameters are initialized, the main solution loop can begin. The input parameters are then iterated over, and each section's minor and major losses can be obtained.

Step 2: Include Losses

Step 2 of the solver is to include losses in the model. Due to the iterative nature of the solution, an arbitrary iteration, i, will be used in the further explanations. Fig. 3.8 shows an arbitrary section of an OSA patient's upper airways and is used as a reference for an arbitrary section, where $i-1$ and i indicate the beginning and end of a section, respectively. Index j is used to represent properties between cross-sections, e.g. the minor loss coefficient $K_{L,j}$ which applies to the section itself, not cross-section i. However, their effects are included in the pressure calculations for cross-section i.

Minor losses

The minor losses are calculated by first determining what type of loss is present by comparing the hydraulic diameters of each cross-section. If $D_{h,i} > D_{h,i-1}$ there is an expansion and the minor loss coefficient $K_{L,j}$ is either determined by Eq. (2.11) or by interpolating the values in Table 2.1. If $D_{h,i} < D_{h,i-1}$ there is a contraction and the minor loss coefficient $K_{L,j}$ is determined by Eq. (2.12) or by interpolating the values in Table 2.2. The minor loss coefficient is set to zero if the hydraulic diameter is the same for both cross-sections. For the solution algorithm, losses for bends are added manually through user-added losses. With the loss coefficient for a section obtained, the minor loss, $h_{L,minor,j}$, for a section can be calculated using Eq. (2.10).

Major losses

For calculating the major loss of a section, $h_{L,major,j}$, the friction factor f_i and the length between cross-section $i-1$ and i are obtained. With the relevant major loss variables obtained, $h_{L,major,j}$ for the section is calculated using Eq. (2.4).

Step 3: Obtain the Area-Averaged Gauge Pressure

With both the minor and major losses for the section known, the total irreversible head loss, $h_{L,i}$ for cross-section i, is calculated by adding $h_{L,minor,j}$ and $h_{L,major,j}$ together. The area-averaged gauge pressure is obtained by applying the parameters determined in the previous steps, and the pressure from iteration $i-1$ to Eq. (2.2).

Step 4: Evaluate Output and Include User Added Losses

All the losses and parameters are presented in the DataFrame format used as input. The data can be visualized and verified using available data from this output. If any user-added losses need to be included for a patient-specific case, this step is where they are added. User-added losses are added to through rerunning the simulations. However, the major and minor losses are not re-calculated as they are retained from the initial simulation.

Final Output

Once the results are acceptable, the final output can be extracted and used for further analysis.

Chapter 4

Numerical Validation of the Hydraulic Diameter

As mentioned in the introduction, converting two ducts into one using the hydraulic diameter is not a common approach. To the author's knowledge, this conversion has not been used in the method proposed in the pragmatic model. Validation of the hydraulic diameter's validity on a two-channel cross-section has been examined to determine if the conversion approach is valid. The validation procedure, along with its results and conclusions, are presented in this chapter.

4.1 Method

4.1.1 Numerical Setup

A simple numerical case was chosen to validate the use of the hydraulic diameter on cross-sections from the human upper airways. For simplicity, a duct was chosen as the foundation of the simplified geometry. A wall was then introduced to the geometry giving the duct a divided geometry, further mimicking the human upper airway geometry in the nasal cavity. The separating wall is the simple geometry's counterpart to the septum, the cartilage which divides the nasal passage in the airways [46]. One of the ducts was created more narrow than the other because of the prevalence of deviated septums in OSA cases. A deviated septum is a deformation of the cartilage and bone wall separating the nasal passages, which impacts the many functions of the nasal cavity [47]. Therefore, the variation in geometry between the two passages in the numerical geometry was implemented to generalize the test case. Fig. 4.1 shows the setup and the dimensions of the different passages. The length of the wall was chosen to allow the flow to develop while not necessarily becoming fully developed, as the flow in the nasal cavity does not become fully developed due to the short entry length and its varying geometry. Two test cases were chosen since differences will occur in the various patient-specific upper airways. Both of the test cases have the same overall dimensions apart from the leading and trailing ends of the wall. One numerical case has a wedge at the leading and trailing ends of the

wall, while the other has flat ends.

Wall with Wedged Ends

In the human upper airways, flow separation is likely to occur at various stages because of the complexity of the geometry. However, for the simple generalizable case presented in this paper, investigating a non-separated flow is of interest, possibly yielding a better base case for future comparison. To avoid flow separation leading into the region with two passages, a 10.4° wedge is placed in front of the wall. The walls on either side are flat, which effectively leads to an angle of 5° for either passage. For a circular diffuser, flow separation has been found to occur in the range $1000 \leq \mathrm{Re} \leq 4000$ [48] giving a comparable case downstream of the wall. The Reynolds number of the flow in both of the single duct sections, prior to and post the separated passages, was $\mathrm{Re} = 2500$. Although the test case is not circular, it was chosen as a case with a lower chance of separation than its wedge-less counterpart. The dimensions of the computational domain have been taken from the height and width of a nasal cavity cross-section at its largest point. The left figure in Fig. 3.6 shows the cross-section used which was taken from patient 12's nasal cavity.

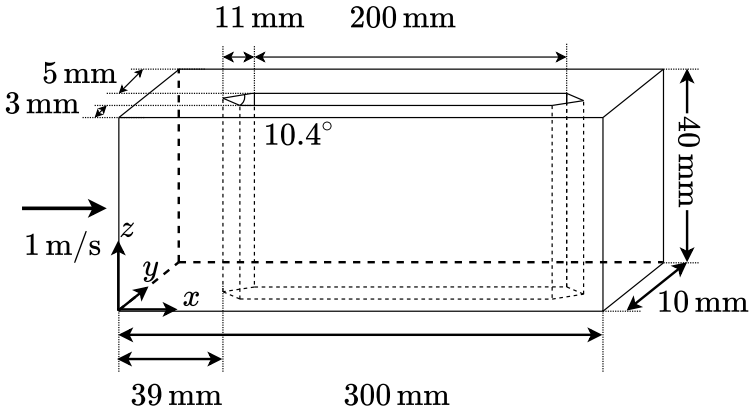

Figure 4.1: Numerical setup with 10.4° wedges at both ends of the separating wall.

Wall with Flat Ends

An alternative numerical setup to the wedged setup presented in the section above was tested. This alternative setup was proposed to capture flow separation and recirculation which are likely to occur in the complex human upper airways [49]. The alternative setup chosen is identical to Fig. 4.1 apart from the leading and trailing ends of the separating wall, which in the alternative case are flat. The alternative setup is shown in Fig. 4.2. The flat leading and trailing ends of the separating wall are hypothesized to cause flow separation and recirculation, similar to the flow structures found in a backward-facing step [50]. This is meant to aid in the validation of the hydraulic diameter by providing more test data that more closely resembles actual human upper airway flow structures.

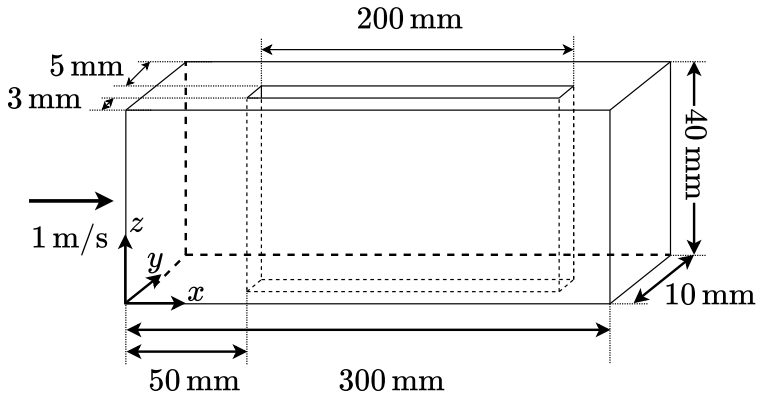

Figure 4.2: Numerical setup where the leading and trailing ends of the separating wall are flat.

4.1.2 Inlet and Boundary Conditions

For both test cases, the boundary conditions at the inlet and outlet were the same. In both cases, air with a kinematic viscosity of $\nu = 1.6 \cdot 10^{-5}$ was used as the fluid. A fully developed laminar flow was given as the inlet condition. The fully developed flow was found by extending the numerical domain prior to the inlet by an entry length of 800 mm, with a uniform flow of $V = 1\,\mathrm{m/s}$ at the inlet of the extended domain. The entry length was found using the equation for a nondimensional hydrodynamic entry length for a laminar flow [32, p. 342]. The inlet velocity was found by calculating the Reynolds number using the actual human upper airway geometry and is based on a flow rate of 250 mL/s [38]. The outlet condition specified the gauge pressure and is set to 0 Pa at the end of the flow domain. The outer and internal separating walls were treated with no-slip boundary conditions.

4.1.3 Grid Generation

The mesh for both cases was created using Ansys Meshing [51], a part of the Ansys simulation environment, where all of the simulations were carried out. With the help of the mesh creator and Ansys Workbench [52], several different grid configurations were tested to find a grid that would provide a grid-independent solution. The result from the pragmatic model simulations was the area-averaged gauge pressure. This was a natural quantity to check when performing the mesh independence study. The grid was created by predetermining the number of subdivisions along the outer horizontal edges, the horizontal edges along the separating wall, and the outer vertical edges. The number of divisions along the edges in the flow direction was set to 300. This applied to both the internal edges along the separating wall and the outer edges of the domain. For the outer edges in the y-direction, 8 divisions were used. For the height of the numerical domain, the z-direction, 40 divisions were used. In Ansys Meshing [51], the behavior of these sections was set to "hard" to create a structured mesh mainly containing hexahedral cells. This meshing scheme

made it possible to generate meshes at different scales with the same proportions in a controllable way. Different resolutions for the mesh were created and simulated while controlling the selected parameter, the area-averaged gauge pressure. The meshes with a slightly coarser resolution gave similar pressure values for the control plane. Therefore, the mesh with a higher number of cells was chosen for further simulations since the control parameter remained reasonably constant. The mesh independence study was only performed on the numerical domain with a 10° wedge. The same grid generation technique and resolution were applied to the case with flat wall ends. A complete list of grid properties, solver used, and other simulation information is included in Appendix C.

4.1.4 Tuning the Hydraulic Diameter

Altering the hydraulic diameter given by Eq. (2.13) is proposed to match the results from the CFD investigations more accurately. A novel method to tune this parameter was to define a hydraulic diameter coefficient, C_{D_h}. The hydraulic diameter coefficient replaces the constant, 4, in Eq. (2.13) to obtain a new equation given by (2.14), allowing the possibility to find a coefficient that better represents the present case. The method involved running the CFD simulations described in this chapter along with the pragmatic simulations and comparing the results from both. The pragmatic simulations' input were the flow rate, cross-sectional area, and the wetted perimeter from evenly spaced cross-sections in the streamwise directions of the numerical geometries. The pragmatic model was modified to only include the frictional losses introduced through the major loss term in Eq. (2.4)when validating the hydraulic diameter. The hydraulic diameter is present in the Reynolds number and the loss term itself, leading to a negative squared inverse correlation between the pressure and the hydraulic diameter. This correlation implies that a decrease in the hydraulic diameter leads to a decrease in the pressure slope. To compare the CFD simulations and the pragmatic simulations were run for hydraulic diameter coefficients in the range $3 \leq C_{D_h} \leq 4.2$. The residual sum of squares (RSS) presented in Section 3.3.5 was calculated for each pragmatic simulation. The RSS value given by Eq. (3.1) was calculated using pragmatic and CFD gauge pressures from the middle of the wall to the end of the walled section, i.e. $150\,\text{mm} \leq x \leq 200\,\text{mm}$ in Fig. 4.1 and Fig. 4.2. This was done to reduce the impact of inaccuracies in the error estimation in the entrance regions of the split geometries. In these regions, deviations are expected due to the simple nature of the pragmatic simulations. The hydraulic diameter coefficients could then be obtained by minimizing the error in this region.

4.1.5 Minor Losses and Diffuser Effects

With the pragmatic model using loss relations known from piping systems, the accuracy of these relations is essential. An effect seen in the results of the pragmatic simulations is a nonphysical pressure recovery where the human upper airway geometry has an expansion. The relations for expansions used in the pragmatic model

did not accurately model the pressure difference seen in the CFD simulations [1]. Therefore, it was proposed that the effects of flow separation were more significant than initially thought. To further investigate this increased flow separation and model it accurately, the effects were included in the validation simulations presented in this chapter. This was implemented at the end of the walled section, which is the simplified model's equivalent to where the nasal passages coincide. This effect can be taken into account through added diffuser losses for these sections. These losses were calculated using Eq. (2.15) by using the CFD gauge pressure to calculate the pressure recovery coefficient C_p, using Eq. (2.15). The exit pressure, p_e, in Eq. (2.15) was the CFD gauge pressure from the cross-section downstream of the expansion, and the throat pressure, p_t, in Eq. (2.15) was the gauge pressure from the cross-section upstream of the same expansion. The calculated C_p values for the expanding sections were included in the pragmatic model by solving Eq. (2.15) for the exit pressure p_e using the area-averaged gauge pressure from the pragmatic model, p_{i-1}, as the throat pressure, p_t. This was used as p_i in the pragmatic model instead of using Eq. (2.2) to calculate p_i for this section, leading to a more significant, more physically accurate pressure loss in the relevant region.

4.1.6 Verification of the Numerical Code

A crucial part of any CFD simulation is verifying the accuracy of the code used for simulations. In the present case, this step was done by simplifying the numerical domain. The 3D domain was simplified to a 2D domain with the same height as the 3D domain, 40 mm, and long enough for the flow to fully develop. The fully developed flow was found by using a domain that was 7000 mm in length, allowing the flow to become fully developed. The grid for the verification case was created using Ansys Meshing [51], where a structured grid with rectangular cells was created. The mesh had 1000 cells in the flow direction, where a bias that decreased the cell size from the inlet to the outlet was included to achieve similar cell dimensions as in the 3D case towards the end of the domain. 40 cells were used in the y-direction with even spacings. The inlet velocity was chosen to be $V = 1\,\mathrm{m/s}$ to achieve a Reynolds number of $\mathrm{Re} = 2500$ using the height of the domain as the length scale and $\nu = 1.6 \cdot 10^{-5}$ as the kinematic viscosity. The simulations were carried out using Ansys Fluent [33], using the same settings as the full 3D simulations. The results from the verification were compared to the analytical solution of a plane Poiseuille flow [32, p. 468]. Fig. 4.3 compares the two solutions and shows a high degree of accuracy between the numerical simulations and the analytical solution. Fig. 4.3 also shows the development of the flow, at the locations $x = 0.05, 2$ and $6.9\,\mathrm{m}$, where x is the downstream distance from the inlet located at $x = 0\,\mathrm{m}$. The flow profiles show an expected development with the flow reaching its fully developed state at $x = 6.9\,\mathrm{m}$. Since these results correspond to their analytical counterpart, the solver was considered an accurate enough standard for further numerical investigation.

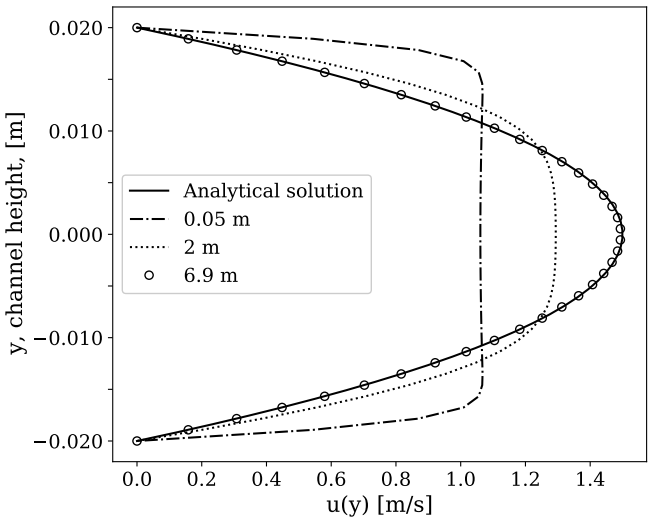

Figure 4.3: Fluid flow profiles at the locations $x = 0.05, 2$ and 6.9 m downstream from the inlet. The flow profile reaches the analytical solution close to the end of the simulation domain, $x = 6.9$ m. The analytical solution is given for a fully developed plane Poiseuille flow.

4.1.7 Pragmatic Simulations

The pragmatic simulations were run using input data found using the numerical geometries. The area-averaged gauge pressure was extracted when the CFD simulations were completed. The pressure was extracted at evenly spaced cross-sections along the length of the numerical domain. The pragmatic model's input for each location is the cross-sectional area, the perimeter, and the flow rate for the given simulation. The cross-sectional area and the perimeter of each cross-section were calculated based on the numerical geometries' dimensions shown in Fig. 4.1 and Fig. 4.2, the extracted values are shown in Tab. 4.1. The flow rate was calculated using the area-averaged input velocity $V = 1\,\mathrm{m/s}$. The flow rate could then be converted into the velocity at the various cross-sections in the wall-separated region using equation (2.3). The pragmatic simulations were then carried out, and the area-averaged gauge pressure from both the pragmatic simulations and the CFD simulations could be compared.

Table 4.1: Cross-sectional area and perimeter calculated using dimensions from Fig. 4.1 and Fig. 4.2, where the dimensions at $x = 45\,\mathrm{mm}$ only apply to the wedged case. This was the input used for the pragmatic simulations of the test case geometries.

x [mm]	A [mm^2]	P_e [mm]
0	400	100
45	356.36	177.82
150	320	176

4.2 Results and Discussion

The area-averaged gauge pressure from the pragmatic simulations and the CFD simulations are compared to assess the accuracy of the standard hydraulic diameter Eq. (2.13) and find an accurate fit for the hydraulic diameter coefficient C_{D_h} in Eq. (2.14). Fig. 4.4 and 4.5 show the results from both simulations along with the initial pragmatic results using Eq. (2.13), which are the uppermost curves The initial results revealed deviations from the CFD simulations, most notably the slope of the area-averaged gauge pressure. The slope of the pragmatic curve was initially too flat and was altered by varying the hydraulic diameter coefficient C_{D_h}. In the Bernoulli equation with losses (2.1) the hydraulic diameter D_h is inversely correlated with the pressure through its representation in the loss term h_L, given by Eq. (2.4). However, as the term is negatively signed, the pressure gradient and the hydraulic diameter correlate, leading to predictable changes when tuning the coefficient C_{D_h}. Changing the hydraulic diameter coefficient and introducing losses from the pressure-recovery coefficient gave more accurate results when compared to the CFD simulations. The effects on the pragmatic model from both of the numerical validation cases are presented and discussed in the following subsections.

4.2.1 Wall with Wedged Ends

Fig. 4.4 shows the results from both the CFD simulations and the pragmatic simulations in the case where the wedge is present. The results show an expected decline in the area-averaged gauge pressure through the geometry. The pragmatic simulations have a linearly decreasing pressure in the middle section, where the separating wall is located, with varying slopes. The CFD simulation results have a less linear shape in the section with the separating wall. However, it has a linear trend further downstream. Compared to the CFD simulations, it has a slight additional pressure loss as the duct is split up and a slight pressure gain at the opposite side. The initial pragmatic results have similar trends but with inflated loss values as well as pressure gain. Using the error minimization approach described in the Section 3.3.5, $C_{D_h} = 3.73$ was found as the optimal hydraulic diameter coefficient. Fig. 4.6 shows a visualization of the optimization. The pressure-recovery coefficient was calculated by applying pressure values from the CFD simulations to Eq. (2.15). This showed an improvement in accuracy downstream of the walled section.

4.2.2 Wall with Flat Ends

The alternative flow situation used to study the hydraulic diameter was also further investigated. For this case, the separating wall has flat ends instead of wedges. The aim of this was to study the effects of tuning the hydraulic diameter coefficient, C_{D_h}, and comparing it to the wedged case to find out how the hydraulic diameter coefficient would deviate from the initial results. This was to study the reliability and generalizability of the results obtained in the wedged case. The results from these simulations are displayed in Fig. 4.5. Minimizing the RSS value for these

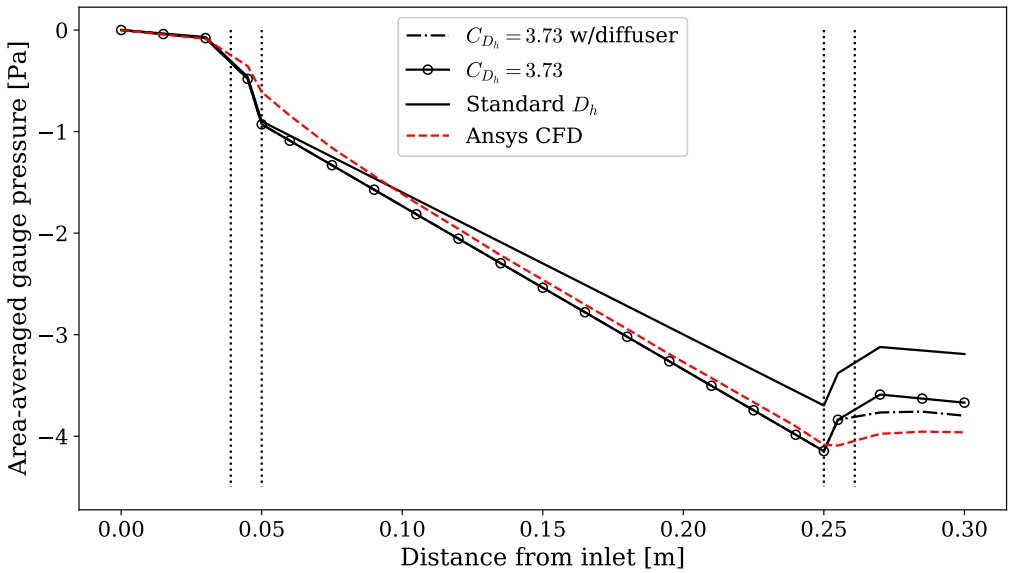

Figure 4.4: Results from Ansys Fluent and corresponding pragmatic simulations for simulations with a 10.4° wedge at both ends of the separating wall. The vertical dotted lines indicate the wedge locations.

simulations gave $C_{D_h} = 3.69$ as the hydraulic diameter coefficient with the highest accuracy. Similarly to the case with 10.4° wedges, applying the increased pressure recovery coefficient to the pragmatic simulations gave a result closer to the CFD simulations. Due to the nature of the geometry with its sudden geometrical changes, the pragmatic model has sudden pressure changes at the beginning of the walled section and at the end, with a pressure loss and a pressure gain, respectively. The same procedure for finding the pressure recovery coefficient was used. In the case with flat ends, this gave a highly accurate result. This implies that there is more flow separation in the non-wedged case. However, this increased accuracy may be due to the sudden changes, which make the pressure recovery coefficient from the CFD simulations easier to find. The increased accuracy using the pressure-recovery coefficient in the wedged versus the non-wedged case is thus inconclusive. However, the use of a pressure recovery coefficient, in general, is promising.

4.3 Conclusions for Validation of Hydraulic Diameter

As a part of creating a pragmatic flow simulator, the hydraulic diameter was used to transform the human upper airway geometry into a piping system. A test case has been created and presented in this chapter to determine if this is a valid assumption to make in the nasal cavity. The test case used two variations of a simple duct-like geometry with a single duct to begin with, which goes over to a split-up section with a separating wall between two passages and a coinciding geometry at the end of the wall. The simulations were performed assuming a laminar steady incompressible airflow with a uniform velocity of 1 m/s at the inlet of the numerical domain. The

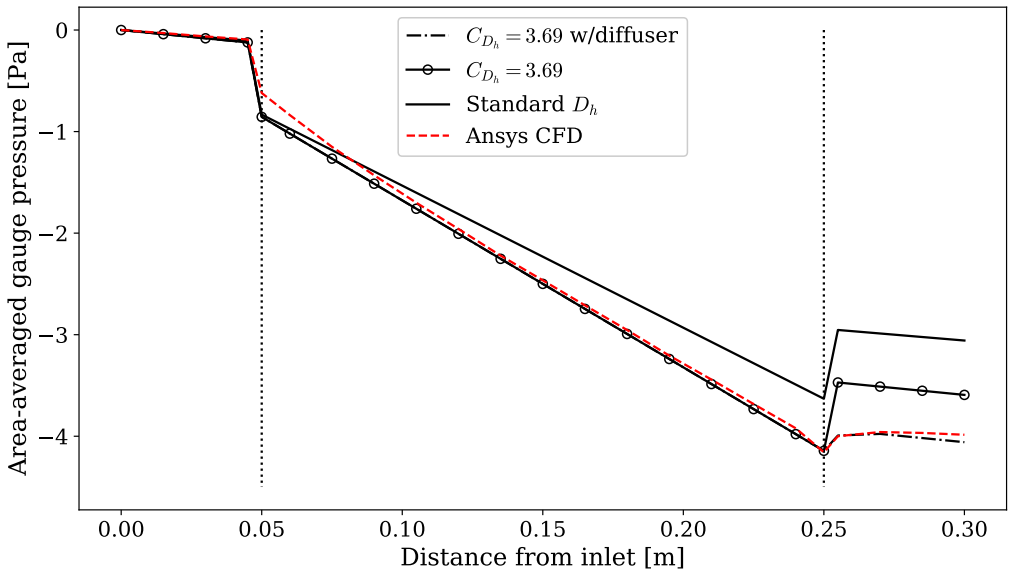

Figure 4.5: Results from Ansys Fluent and corresponding pragmatic simulations for the simulations with flat ends of the separating wall.

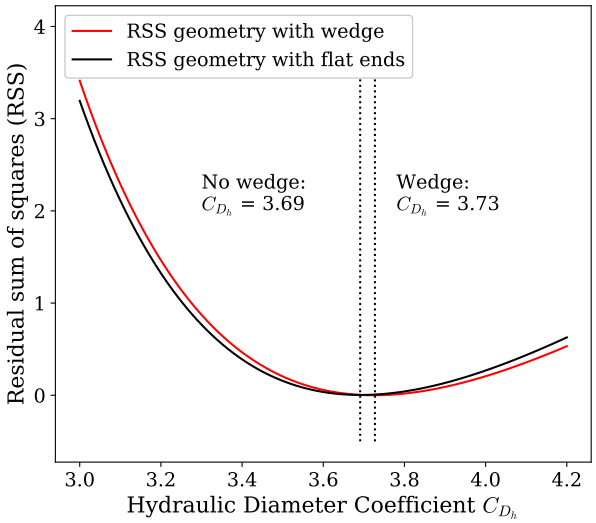

Figure 4.6: Calculations of the RSS values for simulations with and without a 10.4° wedge at the ends of the wall.The vertical dotted line to the right corresponds to best performing hydraulic diameter coefficient for the test case with a wedge, $C_{D_h} = 3.73$. The vertical dotted line to the left corresponds to best performing hydraulic diameter coefficient for test case with flat leading and trailing ends of the separating wall, $C_{D_h} = 3.69$

results from these simulations showed an expected decline in the area-averaged gauge pressure over the length of the geometry. The resulting pressure curve was used comparison with the pragmatic flow simulations. Pragmatic flow simulations were executed, with the only contribution being the frictional losses. Comparing the results to the CFD simulations proved that the pressure slope generated by the pragmatic simulator was a little off. Analyzing different values of the hydraulic diameter coefficient C_{D_h} for the two test cases presented gave two slightly different

values. The two values were $C_{D_h} = 3.72$ and $C_{D_h} = 3.69$ for the case with and without a wedge at the leading and trailing ends of the wall, respectively. This result can further be implemented into the pragmatic model, with data input from the entire upper airway geometry to see if it yields improved simulation performance.

Chapter 5

Results and Discussion

Chapter 3 in this thesis lays the foundation for the improvements of the pragmatic model implemented through the present thesis. Along with the promising results gained through updating the hydraulic diameter coefficient, C_{D_h}, found through the numerical simulations from Chapter 4, their effects on the pragmatic model are presented and discussed in this chapter.

5.1 Hydraulic Diameter Coefficient

Fig. 5.1 shows the results obtained with the implementation of various hydraulic diameter coefficients. The area-averaged gauge pressure curves have been compared to the CFD investigations performed by Aasgrav [38], as presented in Section 3.3.4. Two hydraulic diameter coefficients were found from the validation simulations in Chapter 4. For simplicity in the further use of these coefficients, they were averaged, obtaining a hydraulic diameter coefficient of $C_{D_h} = 3.71$. This coefficient was implemented in the pragmatic model using the upper airways of patient 12 as the base case for comparison. With a hydraulic diameter coefficient of $C_{D_h} = 3.71$, there was a marginal decrease in the slope, which is almost indistinguishable from the implementation using the standard hydraulic diameter. A hydraulic diameter coefficient of $C_{D_h} = 1.80$ is presented as the lowest curve in the figure and was found to be in best agreement with the area-averaged gauge pressure from the CFD simulations. The results show a decreasing trend in the slope of the curves with a decreasing hydraulic diameter coefficient.

The nasal passages become a single passage between cross-sections 3 and 4, which can be seen in Fig. 3.5a. Cross-section number 4 is indicated by a vertical dashed and dotted line in Fig. 5.1, which is the first single-cross-section cutplane. The hydraulic diameter coefficient C_{D_h} was assumed to be valid for the geometry downstream of the coinciding of the nasal passages. The variations in the hydraulic diameter coefficient were therefore only implemented upstream of cross-section 4, and the standard hydraulic diameter given by Eq. (2.13) was used downstream of cross-section 4 as well as for cross-section 4 itself. The results from implementing the hydraulic diameter coefficients, C_{D_h}, from the hydraulic diameter validations, proved

to be inaccurate for the actual human upper airway geometry. Therefore, an effort was made to find a hydraulic diameter coefficient that better fit the verification data.

An optimization approach using the residual sum of squares (RSS) presented in section 3.3.5 was implemented to find the coefficient best fitted for the verification data. To find the best fitting coefficient, 1000 pragmatic simulations were carried out using hydraulic diameter coefficients in the range $1 \leq C_{D_h} \leq 4$, with even spacing between them. The coefficient was assumed to be within this range based on previous simulations. For each simulation, the RSS value was calculated by extracting the area-averaged pressure from cross-sections 1-3, using Eq. (3.1). The results from the optimization scheme are presented in Fig. 5.2. The plot's minimum point indicates that the chosen range of calculated hydraulic diameter coefficients was sufficient. The hydraulic diameter coefficient with the value closest to the CFD results was found to be $C_{D_h} = 1.801$, by obtaining the smallest value from the RSS-curve in Fig. 5.2 and obtaining its associated hydraulic diameter coefficient.

The results from the initial simulations shown in Fig. 5.1 imply that the loss in area-averaged pressure in the upper airways of an OSA patient is more significant than the results from the validation simulations in Chapter 4 indicated. Although the validation simulations concluded that $C_{D_h} = 3.73$ and $C_{D_h} = 3.69$ provided better accuracy for the hydraulic diameter coefficients, it also showed that re-defining the hydraulic diameter may be a promising approach for increasing the pragmatic model's accuracy. A possible explanation is that these deviations might be due to the difference in geometrical complexity between the validation cases shown in Fig. 4.1 and Fig. 4.2 and the upper airways of an OSA patient shown in Fig. 3.5. This difference in complexity may have led to the validation geometries' duct-shaped passages requiring minor tuning to achieve accurate results. These findings indicate that an increase in geometrical complexity requires decreasing the impact of the hydraulic diameter coefficient. This corresponds with the slightly lower value of the hydraulic diameter coefficient found in the test case with flat leading and trailing wall ends. Although the deviations were minor, $C_{D_h} = 3.73$ versus $C_{D_h} = 3.69$, and the geometries mostly were the same in the test cases. This may be an indication that there is a correlation between complex flow structures and the applicability of a reduced hydraulic diameter coefficient.

5.2 Pressure Recovery Coefficient

Fig. 5.3 shows the results obtained by introducing the pressure-recovery coefficients to the pragmatic model. Pressure-recovery coefficients were included in cross-sections 7 and 9 as these cross-sections have the expanding geometry required for diffuser-related flow separation to be induced. These were also the cross-sections from Fig. 5.1 with the most significant deviations from the CFD simulation. In these simulations, the results from Fig.5.1 were used to aid in the obtained accuracy. The results using the hydraulic diameter coefficient from the validation case $C_{D_h} = 3.71$ were also included for further comparison. The pressure recovery coefficient, C_p, has been implemented in the pragmatic model in these simulations. The best results when compared to the CFD simulations were found to be when the pres-

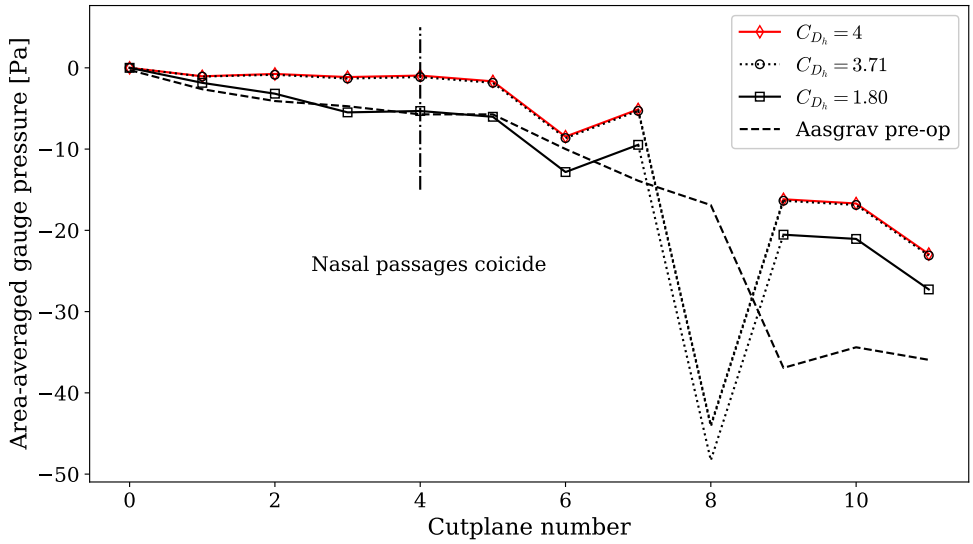

Figure 5.1: Pragmatic simulations where the hydraulic diameter coefficient C_{D_h} was varied. The black dashed and dotted line indicates where the nasal passages coincide. The section in prior to this is where C_{D_h} was varied. The dotted lines indicate the non-comparable cross section as explained in Section 3.3.4.

sure recovery coefficients were $C_p = 0.313$ for cross-section number 7 and $C_p = 0.020$ for cross-section number 9. Applying these coefficients had a similar impact on all three pragmatic cases. However, the pragmatic simulation with $C_{D_h} = 1.80$ was used for the continued optimization due to its previous accuracy.

A similar optimization procedure as the one presented in section 5.1 was used to obtain the presented results. The procedure involved calculating the RSS for a configuration of pressure recovery coefficients. From the nature of the pressure recovery coefficient, its value was assumed to be in the range $0 \leq C_p \leq 1$. The optimization procedure involves choosing a value for the pressure recovery coefficient at cross-section 7 and running simulations with a similar range of coefficients for cross-section 9. The RSS value was then calculated for each combination of coefficients, thus obtaining the optimal values for both pressure recovery coefficients according to the CFD data already acquired. The results showed that the combination of values with $C_p = 0.3131$ and $C_p = 0.0202$ for cross-section 7 and 9 respectively, gave the smallest deviation from the verification case. All of the curves presented in Fig. 5.3 have used the pressure recovery coefficients presented above.

The procedure used for calculating the pressure recovery coefficient in the validation simulation from Chapter 4 gave an improved accuracy for the pragmatic simulations when compared to the test-case CFD simulations. A similar cross-section to the coinciding of the passages in those simulations is cross-section number 3 in patient 12's upper airways, leaving cross-section number 4 to be affected by the pressure recovery coefficient. However, in the simulations using an OSA patient's geometry, there is no significant pressure recovery for cross-section number 4 compared to the CFD verification case. This can be seen in Fig. 5.1 where the curve has a similar slope for all the hydraulic diameter coefficients tested between cross-sections 3 and

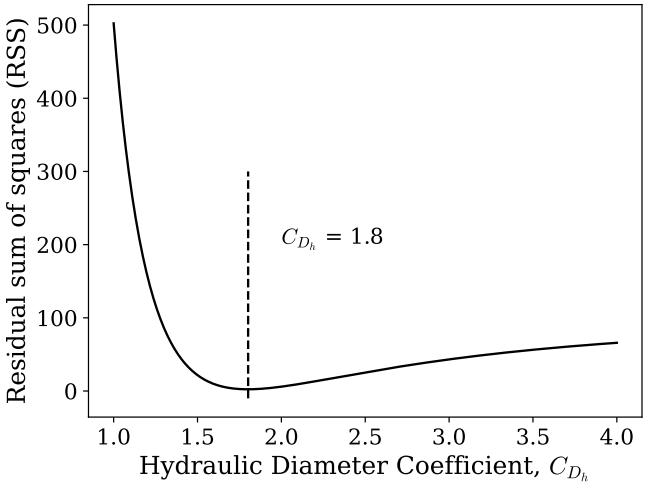

Figure 5.2: RSS values for the deviation between the area-averaged gauge pressure calculated by the pragmatic model and through CFD [38]. The vertical dashed line indicates the minimum point along the curve, which corresponds to the pragmatic result with the best accuracy.

4. Therefore, improving the accuracy of this cross-section by applying a pressure recovery coefficient was abandoned. The lack of deviation for cross-sections 3-4 between the curves could be due to the difference in the geometrical setups. The wall of both of the numerical setups shown in Fig. 4.1 and Fig. 4.2 is greater than the thin septum in the actual human upper airways. Therefore, the pressure recovery in the numerical test cases could be more prominent for the section directly downstream of the coinciding passages.

Since the method used for obtaining the pressure-recovery coefficients for the pragmatic simulations using data from patient 12 is patient-specific, its applicability for other patients might vary. However, it is an excellent start for obtaining the correct parameters to give the pragmatic model added accuracy. The nature of the optimization method is expected to produce results that are in good agreement with the CFD verification case, as it essentially is a curve-fitting procedure. Even after the optimization procedure, there are still some notable deviations between the pragmatic results and the CFD simulations. The minor deviations between the curves upstream of cross-section 5 are thought to be due to expected deviations between models. However, there is a notable deviation between the results for cross-section number 6. Fig. 3.5a shows the cross-section's location on the 3D model, which is close to the uvula. This cross-section also extends into a non-comparable flow domain similarly to cross-section 8, discussed in Section 3.3.4. A similar effect could be causing the deviations observed for this cross-section. At the last cross-section, cross-section number 11, the curves with hyraulic diameter coefficients of $C_{D_h} = 4$ and $C_{D_h} = 3.71$ interestingly seem to be in near-perfect agreement with the CFD simulations. However, this is likely due to coincidence, as $C_{D_h} = 1.8$ was the curve used for the optimization. Overall the curve with $C_{D_h} = 1.8$ is in good agreement with the CFD simulation results and is a good foundation for indicating the pragmatic model's potential. Pragmatic simulations using the post-operative case and the same parameters could indicate the model's applicability in other cases than

patient 12's pre-operative geometry.

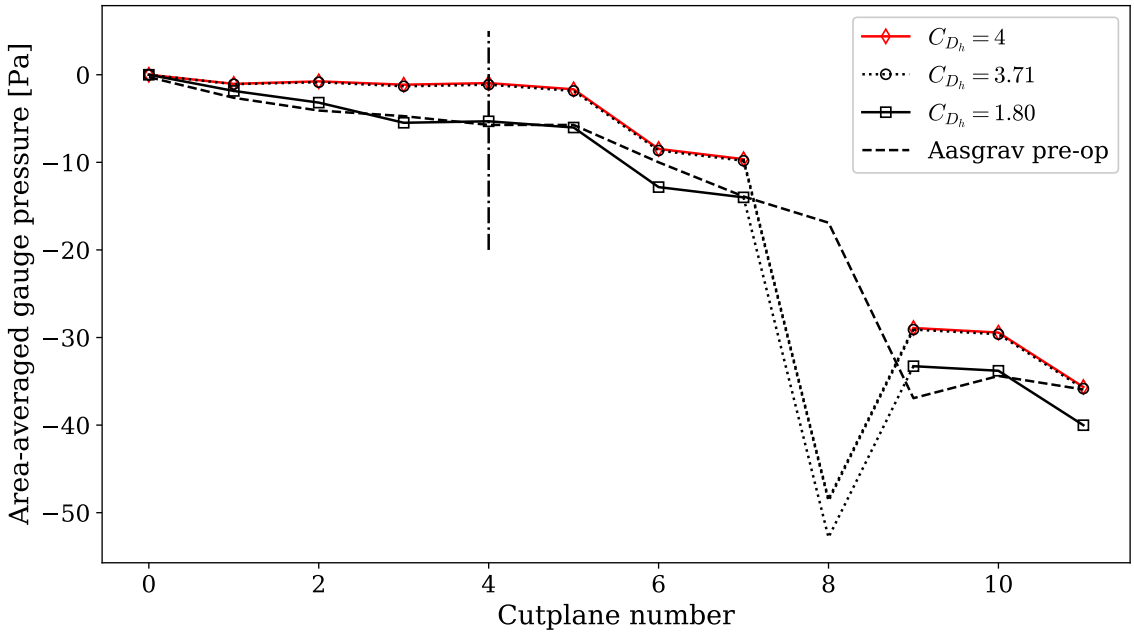

Figure 5.3: Results from pragmatic simulations with pressure-recovery coefficients included. $C_p = 0.31$ was included for cross-section 7 and $C_p = 0.02$ for cross-section 9.

5.3 Post Operative Results

Pragmatic simulations of the post-operative geometry were carried out to assess the accuracy of the settings found from simulations shown in Fig. 5.1 and 5.3. The results of the post-operative simulations are shown in Fig. 5.4. Similar to the results presented previously, the results from the pragmatic simulations have been compared to the CFD simulations performed by Aasgrav [38]. The corresponding post-operative CFD simulations were compared with the post-operative pragmatic simulations. The simulation parameters for the pressure-recovery coefficient, C_p, and the hydraulic diameter coefficient, C_{D_h}, that gave the most accurate results were used for the post-operative pragmatic simulations. The post-operative case shows a similar trend to the pre-operative case, with a more significant pressure loss. However, there was some deviation in the nasal cavity and towards the trachea.

The results generally show a good correspondence with the post-operative CFD simulations. This indicates that applying changes to a pre-operative simulation may lead to accurate post-operative results for the same patient. Although for any conclusions to be made regarding the correlation between pre-and post-operative results, further analyses are needed through a study with more patients.

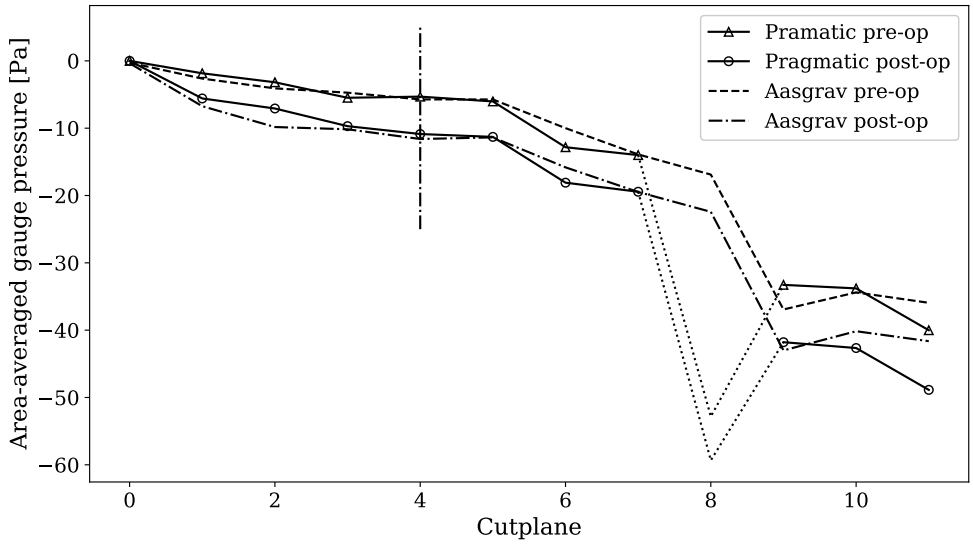

Figure 5.4: Pragmatic simulation using the pre-and post-operative data from patient 12 as input. The results of the pre-and post-operative CFD simulations have been included for comparison.

5.4 Patient Specific Results

An important indicator of the success of this model is its ability to predict flows in different patients reliably. Using the procedures for extracting data from CT-images described in chapter 3 data from patient 1 and patient 6 from the study by Moxness et al. [26] were retrieved. These resulting inputs for the pragmatic flow simulations are presented in table 5.1. For both patients, the pre-operative case was used for the geometry retrieval. The retrieved cross-sectional area, perimeter, and distances to the cross-sections were used as input for the pragmatic simulations. Fig. 5.5 shows the results from these simulations. For both cases, two simulations were performed, one without any user-added losses, i.e., only the losses calculated from the pragmatic model's algorithm were included. For the alternative simulation, the losses used to compensate for pressure-recovery found in Section 5.2 were included. The results from the pragmatic simulations using the data from patient 12 in its best performing configuration have been included for comparison. $C_{D_h} = 1.8$ was used for all of the simulations and was implemented using the approach described in Section 5.1.

Due to the lack of verification data for these patients, it is challenging to discuss their accuracy. However, a short preliminary discussion is included in this thesis. The results from patient 1, without the additional pressure-recovery coefficient, showed some similar unphysical pressure-recovery trends as the results from patient 12. This is likely to be in part due to similar factors, as the added use of the pressure-recovery coefficients used for the patient 12 simulations gave a reduced area-averaged gauge pressure. Patient 6 has a similar trend for the first cross-sections. However, its flat nature further downstream indicates that the parameters might not be correctly tuned. A decrease in the area-averaged pressure is also seen for patient 6. However, it is less prominent than for patient 12 and patient 1. Due to the varying nature of

the human upper airway geometries, it is unknown if these curves represent the flow in these patients' upper airways correctly. However, it does show that the pragmatic model has potential, although further verification is required. An essential factor in the deviation of these curves is the CT-extraction method. It is a fast and potentially less accurate method than creating a perfect 3D model of the upper airways. Since the nature of the method is prone to deviations, the input of the pragmatic model will also have variations. A sensitivity study where the pragmatic model's input has therefore been performed in section 5.5 to assess the pragmatic model's sensitivity to input variations.

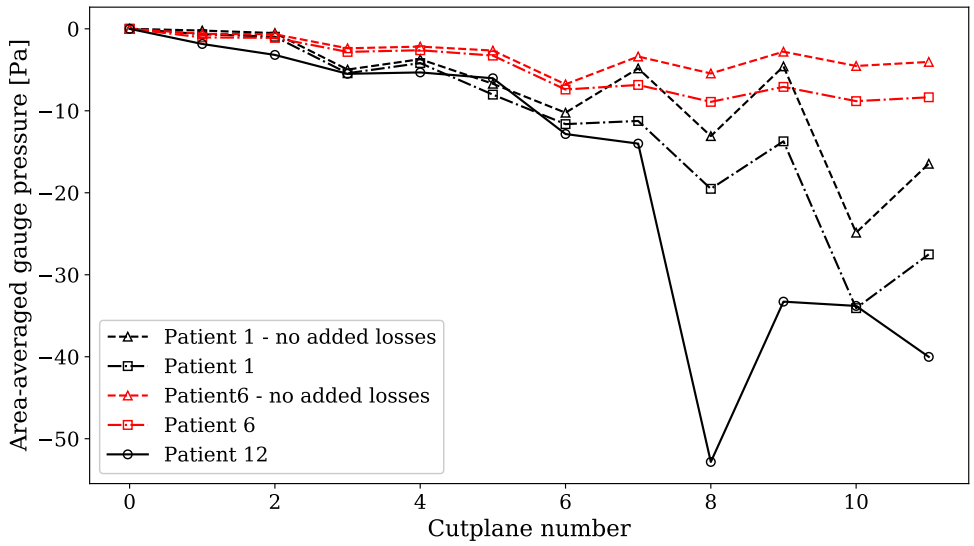

Figure 5.5: Pragmatic simulations using data from patient 1 and patient 6. The pragmatic simulation result with the best accuracy from Fig. 5.3 has been included for comparison.

5.5 Sensitivity Study

The procedure for creating 3D models from patient-specific data, presented in section 3.2, is an efficient approach for obtaining input for the pragmatic model. However, the accuracy of the resulting 3D models is unknown. Although a detailed assessment of the accuracy of these models is outside the scope of the present thesis, a study of variations to the input of the pragmatic flow simulations is worth investigating. A sensitivity study was performed to assess the pragmatic model's sensitivity to input variations. This was done by applying variations to the cross-sectional area of the data extracted from patient 12's pre-operative geometry. The new cross-sectional area was used as input for the pragmatic simulations. The area-averaged gauge pressure at cross-section 11, the last cross-section, was used for comparison as it indicates the total impact of the area deviations. The chosen method is not entirely precise since a cross-section with a decreased area also would have a smaller perimeter in most cases. However, it was chosen for simplicity. Although it is not

Table 5.1: Data extracted from the 3D geometries of patient 1 and patient 6. This was used as input for the pragmatic flow prediction of these patients' airways.

	Patient 1			Patient 6		
Cutplane number	Area [mm^2]	Perimeter [mm]	Distance [mm]	Area [mm^2]	Perimeter [mm]	Distance [mm]
0	214.27	89.60	0.00	216.24	91.20	0.00
1	298.48	144.96	19.81	275.12	148.56	22.03
2	369.74	224.74	35.17	500.98	319.60	39.98
3	187.75	219.60	56.62	368.70	296.70	66.12
4	409.57	91.74	78.07	586.85	96.97	86.45
5	151.31	47.29	93.67	335.32	71.77	102.65
6	109.05	45.80	107.40	130.00	54.00	119.60
7	275.28	76.84	125.43	261.78	62.60	137.00
8	92.40	43.50	135.44	158.50	55.23	161.42
9	387.58	104.61	149.91	462.43	136.90	183.10
10	61.64	30.75	161.64	195.18	57.00	201.94
11	89.31	39.57	167.34	249.00	56.60	221.04

entirely accurate, it helps indicate the effect varying the cross-sectional area has on the pragmatic simulations. Variations of the cross-sectional area from -10% to 10% were included, as this was considered a plausible input variation range with the given data extraction method. The results from the sensitivity study are displayed in Table 5.2. Where the decreases in the cross-sectional area led to decreases in the area-averaged gauge pressure and increases in the cross-sectional area led to increases in area-averaged gauge pressure.

They indicate that the total loss in area-averaged gauge pressure is sensitive to the changes in the data used as input. The area-averaged gauge pressure sees a deviation of around three times the amount applied to the cross-sectional area. This proves that the input created by the 3D models needs to be fairly accurate to achieve reliable results. However, during an actual extraction, the deviation would not apply equally to all of the cross-sections like in this sensitivity study. Thus the actual deviations might be lower if only a few of the cross-sections are affected by inaccuracies. However, the sensitivity study shows that the pragmatic model is relatively sensitive to input variations and is an essential factor to consider for the model's future use.

5.6 Computing Time of the Pragmatic Model

One of the advantages of the pragmatic model is its low computational cost compared to traditional CFD simulations. The model presented has an initial simulation which gives a baseline result by calculating the baseline area-averaged gauge pressure through a simulation. Different parameters of the simulation can be varied depending on each specific case. Alterations can be included before obtaining the initial results or as user-added losses after the simulations. In both cases, updating the

Table 5.2: Results from sensitivity study. Deviations were applied to patient 12's cross-sectional area, and pragmatic simulations were performed. The deviation from the most accurate pragmatic simulation with $C_{D_h} = 1.8$ and added pressure recovery coefficients were obtained for the last cross-section, cross-section 11. All of the simulations' parameters, except for the cross-sectional area, were kept the same.

Deviation applied to the cross-sectional area	-10%	-5%	-2%	-1%	1%	2%	5%	10%
Deviation in area-averaged gauge pressure	-33.4%	-14.4%	-4.8%	-1.9%	3.8%	6.7%	15.5%	31.1%

parameters to improve the simulation results is essential. Result updates in real-time would be beneficial to make this a seamless process. Therefore, computing times from pragmatic simulations with various settings applied have been obtained. The resulting computing times are presented in Table 5.3. In the base case, the hydraulic diameter coefficient for the first four cross-sections from $C_{D_h} = 4$ to $C_{D_h} = 1.8$ was the only modification. The subsequent simulations use the same modifications of the hydraulic diameter coefficient mentioned above. Case 2 includes the additional minor losses for bends. Case 3 includes the pressure recovery coefficients from section 5.2 along with the minor losses for bends. Due to the nature of the results, visualization of the area-averaged gauge pressure is important. Therefore, computing times for the same three cases, where their corresponding visual representations are shown, have been included. The computer used for all simulations was a Dell inc. OptiPlex 7060 with six processor cores with a clock rate of 3.20GHz and 32 GB of memory. The results show lower simulation times for simulations where user-added losses are included, which is unexpected. However, this could be due to the way Python calculates the run time of a code, and will not be further investigated in this study. With mean simulation times being on the scale of 0.001 s, it can be concluded that the simulations can provide real-time results.

Table 5.3: The computational time for pragmatic simulations. For the Base Case 1, user-added input was included. For Case 2 the addition of minor losses for bends were added, and for Case 3, pressure-recovery coefficients were added on top of the minor losses from Case 2.

	Without visualization [s]	With visualization [s]
Base Case	0.0013 ± 0.0003	0.024 ± 0.0005
Case 2	0.0011 ± 0.0004	0.026 ± 0.0007
Case 3	0.0011 ± 0.0004	0.022 ± 0.0008

5.7 Discussion of the Hydraulic Diameter as Choice of Optimization Parameter

When choosing which parameter to use as an optimization parameter for this study, the hydraulic diameter was one of the possible parameters which could be updated. Another notable variation that could be made for the upper airway geometry was varying the friction factor. The laminar friction factor impacts the major losses in the Bernoulli equation with losses Eq. (2.2). The laminar friction factor given by Eq. (2.7), is meant for a flow through a circular pipe [32], making it applicable when using the hydraulic diameter Eq. (2.13). Through turbulent and laminar CFD studies performed on an OSA patient's upper airways [38], turbulence was found to have a negligible impact on the area-averaged gauge pressure. In the author's specialization project [1], the same conclusion was reached by implementing the turbulent friction factors provided by Haaland and Colebrook [32, p. 357]. Therefore, including a turbulent friction factor was not used as an optimization parameter. For non-circular ducts alternative relations apply [32, p.348]. This could have been used as an alternative optimization parameter to the hydraulic diameter since the wetted perimeters of the cross-sections in the nasal cavity are large, making frictional impact important. Changing the friction factor would also leave the hydraulic diameter in its intended form, which implies that using the area and perimeter of a circle in Eq. (2.13) returns the circle's diameter. This would be an interesting investigation, however, it is outside the scope of this thesis.

Chapter 6

Conclusions

Due to the complicated flow dynamics in the human upper airways, predicting surgical outcomes of surgery performed on OSA patients is challenging. CFD simulations can model the flow structures and provide accurate flow predictions for many cases. However, its use requires expertise, and it is a time-consuming and computationally expensive approach. Through previous work by the author, a pragmatic model for predicting flow in the human upper airways of OSA patients has been developed. The pragmatic model aimed to combine the accuracy of CFD with near real-time simulation speeds. The model is aimed to eventually provide doctors with an easy-to-use tool to obtain insights into which surgical procedure has the best chance of success. The objective of this thesis has been to gain further insights into the surgical treatment of OSA patients and to make further improvements to the pragmatic model. The improvements included developing a system to obtain flow predictions from patient-specific CT scans. A procedure for creating 3D models of OSA patients' upper airways has been developed to obtain a simple way of providing necessary input for the pragmatic model's 1D flow simulations.

A CFD test case was used to validate the use of the hydraulic diameter conversion in the nasal cavity of OSA patients. The results from the CFD investigations showed that the standard hydraulic diameter applied to a numerical domain with a separated geometry was not entirely accurate. Therefore, a novel approach that involved redefining the hydraulic diameter for more complicated geometries was developed. The approach involved changing the constant 4 in the standard equation to a variable parameter, C_{D_h}, termed the hydraulic diameter coefficient. For the test cases, $C_{D_h} = 3.71$ applied to the pragmatic model was in good agreement with the results from the CFD simulations. Applied to an OSA patient's nasal cavity, this coefficient had a negligible effect on the accuracy of the flow predictions. For the upper airways of OSA patient 12, $C_{D_h} = 1.8$ was found to give the most accurate results compared to the CFD simulations performed on the same geometry. The validation procedure provided evidence that the hydraulic diameter coefficient had the potential for alteration to reach a more accurate result.

In the previous iteration of the pragmatic model, deviations were found in sections of the upper airways where the OSA patient's upper airways had expanding geometries. A pressure-recovery coefficient has been included to better account for

the unphysical pressure recovery in expanding sections of the upper airways. The investigation of including a pressure-recovery coefficient was continued, using the pragmatic model with an updated hydraulic diameter coefficient. The most notable expanding sections in the geometry were given hydraulic diameter coefficients to match the area-averaged gauge pressure from CFD simulations. A curve-fitting procedure was implemented, giving the results from the pragmatic simulations excellent agreement with the CFD simulations after their implementations. Although the results were found by fitting the pragmatic simulation results to the CFD data, they prove that a pressure-recovery coefficient can be beneficial in improving the model's accuracy. The added pressure-recovery coefficients could be essential additions to the pragmatic model as they create a way of more accurately modeling the effects of flow separation than the included minor losses, as the effects of flow separation can be challenging to capture through a 1D simulation.

Implementing the various improvements in the pragmatic model for other OSA patients gave a notable decrease in the area-averaged gauge pressure. They were not entirely accurate compared to the area-averaged gauge pressure from the base comparison case used for the above optimizations. However, it is difficult to conclude whether this is due to inherent differences between flow in the upper airways of OSA patients or if the model does not apply to other patients. The results are inconclusive since there is no verification data for these patients.

In conclusion, major updates have been made to the pragmatic model, and a complete system for providing flow predictions based on patient-specific CT images has been developed. Although the pragmatic model has limitations, due to its simple nature and lack of verification data, its predictive capabilities are promising.

Chapter 7

Further Work

Although advances have been made to improve the pragmatic model presented in the present thesis, there are possibilities for further improvements. For the further validation of the use of hydraulic diameter coefficients found on a patient-specific basis' applicability to different OSA patients needs to be investigated. A more comprehensive range of verification data is required for this to be investigated. This data could be obtained by utilizing CFD, where the 3D models created by the method described in this thesis can be used to create the numerical domains.

The long-term aim of the pragmatic model is to expand it further to include a surgical prediction tool and to create something like a desktop application, complete with a user interface. For this to become a reality, the CT segmentation process should be automatic, only requiring the user's CT images to be uploaded.

Bibliography

[1] T. G. Weisz, 'Pragmatic modeling of flow in the human upper airways', Specialization project, NTNU, 2021.

[2] Ashish. 'Why does the human body release carbon dioxide?' (2022), [Online]. Available: https://www.scienceabc.com/humans/why-does-the-human-body-release-carbon-dioxide.html. accessed: 06.05.2022.

[3] D. J. Gottlieb and N. M. Punjabi, 'Diagnosis and management of obstructive sleep apnea: A review', *JAMA*, vol. 323, no. 14, pp. 1389–1400, 2020.

[4] C. V. Senaratna, J. L. Perret, C. J. Lodge *et al.*, 'Prevalence of obstructive sleep apnea in the general population: A systematic review', *Sleep Medicine Reviews*, vol. 34, pp. 70–81, 2017.

[5] T. Gharibeh and R. Mehra, 'Obstructive sleep apnea syndrome: Natural history, diagnosis, and emerging treatment options', *Nature and Science of Sleep*, vol. 2, p. 233, 2010.

[6] E. J. Kezirian, E. M. Weaver, B. Yueh *et al.*, 'Incidence of serious complications after uvulopalatopharyngoplasty', *The Laryngoscope*, vol. 114, no. 3, pp. 450–453, 2004.

[7] M. Friedman, R. Vidyasagar, D. Bliznikas and N. Joseph, 'Does severity of obstructive sleep apnea/hypopnea syndrome predict uvulopalatopharyngoplasty outcome?', *The Laryngoscope*, vol. 115, no. 12, pp. 2109–2113, 2005.

[8] M. R. Mannarino, F. Di Filippo and M. Pirro, 'Obstructive sleep apnea syndrome', *European Journal of Internal Medicine*, vol. 23, no. 7, pp. 586–593, 2012.

[9] D. A. Pevernagie, B. Gnidovec-Strazisar, L. Grote *et al.*, 'On the rise and fall of the apnea- hypopnea index: A historical review and critical appraisal', *Journal of Sleep Research*, vol. 29, no. 4, e13066, 2020.

[10] I. Takenaka and K. Aoyama. 'Prevention of aspiration of gastric contents during attempt in tracheal intubation in the semi-lateral and lateral positions'. (2022), [Online]. Available: https://www.ncbi.nlm.nih.gov/pmc/articles/PMC5143313/ (visited on 05/06/2022).

[11] E. R. Hans A. Dahl, *Menneskets funksjonelle anatomi*. Cappelen Damm AS, 2010.

[12] D. K. Ponnusamy. 'What is airway management?' (2022), [Online]. Available: https://biology-forums.com/index.php?action=gallery;sa=view;id=8486 (visited on 05/06/2022).

[13] X. Tingting, Y. Danming and C. Xin, 'Non-surgical treatment of obstructive sleep apnea syndrome', *European Archives of Oto-Rhino-Laryngology*, vol. 275, no. 2, pp. 335–346, 2018.

[14] B. Carvalho, J. Hsia and R. Capasso, 'Surgical therapy of obstructive sleep apnea: A review', *Neurotherapeutics*, vol. 9, no. 4, pp. 710–716, 2012.

[15] K. K. Li, 'Surgical therapy for adult obstructive sleep apnea', *Sleep Medicine Reviews*, vol. 9, no. 3, pp. 201–209, 2005.

[16] J. S. Virk and B. Kotecha, 'When continuous positive airway pressure (CPAP) fails', *Journal of Thoracic Disease*, vol. 8, no. 10, E1112, 2016.

[17] A. G. Elshaug, J. R. Moss, A. M. Southcott and J. E. Hiller, 'Redefining success in airway surgery for obstructive sleep apnea: A meta analysis and synthesis of the evidence', *Sleep*, vol. 30, no. 4, pp. 461–467, 2007.

[18] J. T. Maurer, 'Update on surgical treatments for sleep apnea', *Swiss Medical Weekly*, vol. 139, no. 4344, 2009.

[19] J. H. Choi, S. H. Cho, S.-N. Kim, J. D. Suh and J. H. Cho, 'Predicting outcomes after uvulopalatopharyngoplasty for adult obstructive sleep apnea: A meta-analysis', *Otolaryngology–Head and Neck Surgery*, vol. 155, no. 6, pp. 904–913, 2016.

[20] A. E. Sher, K. B. Schechtman and J. F. Piccirillo, 'The efficacy of surgical modifications of the upper airway in adults with obstructive sleep apnea syndrome', *Sleep*, vol. 19, no. 2, pp. 156–177, 1996.

[21] M. Van Egmond, M. Rovers, A. Tillema and N. v. Heerbeek, 'Septoplasty for nasal obstruction due to a deviated nasal septum in adults: A systematic review', 2018.

[22] S. Zaghi, J.-E. C. Holty, V. Certal *et al.*, 'Maxillomandibular advancement for treatment of obstructive sleep apnea: A meta-analysis', *JAMA Otolaryngology–Head & Neck Surgery*, vol. 142, no. 1, pp. 58–66, 2016.

[23] M. Camacho, V. Certal, S. E. Brietzke, J.-E. C. Holty, C. Guilleminault and R. Capasso, 'Tracheostomy as treatment for adult obstructive sleep apnea: A systematic review and meta-analysis', *The Laryngoscope*, vol. 124, no. 3, pp. 803–811, 2014.

[24] D. D. Patil and S. G. Deore, 'Medical image segmentation: A review', *International Journal of Computer Science and Mobile Computing*, vol. 2, no. 1, pp. 22–27, 2013.

[25] M. Mustra, K. Delac and M. Grgic, 'Overview of the DICOM standard', vol. 1, pp. 39–44, 2008.

[26] M. H. S. Moxness and S. Nordgård, 'An observational cohort study of the effects of septoplasty with or without inferior turbinate reduction in patients with obstructive sleep apnea', *BMC Ear, Nose and Throat Disorders*, vol. 14, no. 1, pp. 1–5, 2014.

[27] B. Gibaud, 'The dicom standard, a breif overview', *Molecular Imaging: Computer Reconstruction and Practice*, pp. 229–238, 2008.

[28] A. Fedorov, R. Beichel, J. Kalpathy-Cramer *et al.*, '3d slicer as an image computing platform for the quantitative imaging network', *Magnetic resonance imaging*, vol. 30, no. 9, pp. 1323–1341, 2012.

[29] 'Modeling of obstructive sleep apnea by fluid-structure interaction in the upper airways'. (2022), [Online]. Available: http://osas.no/description.

[30] F. M. White, *Fluid Mechanics, 6^{th} ed.* McGraw Hill, 2008.

[31] A. K. Al_Omari, H. F. I. Saied and O. G. Avrunin, 'Analysis of changes of the hydraulic diameter and determination of the air flow modes in the nasal cavity', in *Image Processing and Communications Challenges 3*, Springer, 2011, pp. 303–310.

[32] Y. A. Cengel and J. M. Cimbala, *Fluid Mechanics: Fundamentals and Applications, 2^{nd} ed.* McGraw Hill, 2010.

[33] *Ansys® Fluent, 2021R2, User's Guide*, ANSYS, Inc, 2021.

[34] G. Van Rossum and F. L. Drake, *Python 3 Reference Manual*. Scotts Valley, CA: CreateSpace, 2009, ISBN: 1441412697.

[35] *MeshMixer manual*, Autodesk, 2022. [Online]. Available: https://forums.autodesk.com/autodesk/attachments/autodesk/138/367/1/MeshmixerManual.pdf.

[36] L. Zhu, I. Kolesov, Y. Gao, R. Kikinis and A. Tannenbaum, 'An effective interactive medical image segmentation method using fast growcut', in *MICCAI workshop on interactive medical image computing*, 2014.

[37] *Ansys® Spaceclaim, 2021R2, Discovery Spaceclaim*, ANSYS, Inc, 2021.

[38] E. Aasgrav, 'CFD Simulations of Turbulent Flow in the Human Upper Airways', master's thesis, NTNU, 2017.

[39] Microsoft Corporation, *Microsoft excel*, version 2019 (16.0), 24th Sep. 2018. [Online]. Available: https://office.microsoft.com/excel.

[40] M. R. Jordal, S. G. Johnsen, S. K. Dahl and B. Müller, 'Patient Specific Numerical Simulation of Flow in the Human Upper Airways for Assessing the Effect of Nasal Surgery', en, *Progress in Applied CFD - CFD - 2017*, pp. 153–162, 2017.

[41] P. A. Yushkevich, J. Piven, H. Cody Hazlett *et al.*, 'User-guided 3D active contour segmentation of anatomical structures: Significantly improved efficiency and reliability', *Neuroimage*, vol. 31, no. 3, pp. 1116–1128, 2006.

[42] M. R. Jordal, 'Geometry retrieval from ct and mri of the human upper airways', *Project work, The Norwegian University of Science and Technology*, 2015.

[43] E. Aasgrav, S. Johnsen, A. Simonsen and B. Müller, 'CFD simulations of turbulent flow in the upper airways', *The Norwegian*, 2016.

[44] Wikipedia contributors, *Residual sum of squares — Wikipedia, the free encyclopedia*, [Online; accessed 29.05.2022], 2022. [Online]. Available: https://en.wikipedia.org/wiki/Residual_sum_of_squares.

[45] T. pandas development team, *Pandas-dev/pandas: Pandas*, version latest, Feb. 2020. DOI: 10.5281/zenodo.3509134. [Online]. Available: https://doi.org/10.5281/zenodo.3509134.

[46] C. Matthias, 'Surgery of the nasal septum and turbinates', *GMS Current Topics in Otorhinolaryngology, Head and Neck Surgery*, vol. 6, 2007.

[47] N. Fettman, T. Sanford and R. Sindwani, 'Surgical management of the deviated septum: Techniques in septoplasty', *Otolaryngologic Clinics of North America*, vol. 42, no. 2, pp. 241–252, 2009.

[48] E. Sparrow, J. Abraham and W. Minkowycz, 'Flow separation in a diverging conical duct: Effect of reynolds number and divergence angle', *International Journal of Heat and Mass Transfer*, vol. 52, no. 13-14, pp. 3079–3083, 2009.

[49] T. B. Martonen, L. Quan, Z. Zhang and C. Musante, 'Flow simulation in the human upper respiratory tract', *Cell Biochemistry and Biophysics*, vol. 37, no. 1, pp. 27–36, 2002.

[50] T. Lee and D. Mateescu, 'Experimental and numerical investigation of 2D backward-facing step flow', *Journal of Fluids and Structures*, vol. 12, no. 6, pp. 703–716, 1998.

[51] *Ansys® Meshing, 2021R2, ANSYS Meshing User's Guide*, ANSYS, Inc, 2021.

[52] *Ansys® Workbench, 2021R2, User's Guide*, ANSYS, Inc, 2021.

Appendix

A Conference Paper Submitted to SIMS2022

Simulation of Flow in the Human Upper Airways Modeled as a Piping System Using the Hydraulic Diameter

Thor Gudmund Weisz [a,*], Bernhard Müller [b], Reidar Kristoffersen [c],

[a,b,c] *Department of Energy and Process Engineering, NTNU, Trondheim, Norway*
[*] *thor.weisz@gmail.com*

Abstract

Obstructive sleep apnea (OSA) is a medical condition characterized by repetitive obstructions in the human upper airways during sleep. Recent estimates from the United States show that the condition impacts 15% to 20% of the adult population. OSA treatment can be subdivided into surgical and non-surgical approaches. Non-surgical approaches such as continuous positive airway pressure (CPAP) devices have the highest success rates when used correctly. However, these approaches have low patient compliance due to the invasive nature of the devices during sleep, leaving surgery as a viable alternative for many. Predicting the outcome of OSA surgery is difficult due to the complex nature of both the airways and the surgeries themselves. CFD modeling of the airways is a helpful way to gain valuable insights into the flow structures and the impact of individual surgeries on the airways. However, CFD is not a viable approach for each patient-specific case due to its time-consuming nature. A pragmatic model has been created to predict the outcome of OSA surgery on a patient-specific basis to produce valid surgical estimates fast to be used by non-CFD engineers. The model transforms the human upper airways into a piping system by applying the hydraulic diameter equation on geometries created from CT scans. This paper aims to validate the use of the hydraulic diameter given by $D_h = 4 \cdot \frac{A}{P_e}$, where A is the cross-sectional area and P_e is the wetted perimeter, on the complex geometries of the nasal cavity and to provide a novel equation for the hydraulic diameter in the nasal cavity. The proposed hydraulic diameter equation is given by $D_h = C_{D_h} \cdot \frac{A}{P_e}$ where C_{D_h} is the hydraulic diameter coefficient. Airflow has been simulated through a simplified geometry using CFD to validate the hydraulic diameter and find an updated equation. Pragmatic model simulations using the hydraulic diameter have been compared to the results from CFD simulations to assess the pragmatic model's accuracy. The results showed that the original hydraulic diameter did not give entirely accurate results and that the novel equation using $C_{D_h} = 3.71$ gave the pragmatic model better accuracy for the validation cases. Tuning the parameter C_{D_h} for flow in an OSA patient's upper airways, the pragmatic model succeeded in quite accurately reproducing the area-averaged pressure in the patient's upper airways.

1. Introduction

Obstructive sleep apnea (OSA) is a sleep disorder characterized by repeated collapses of the upper airways during sleep. These collapses obstruct airflow, leading to loss of oxygen intake and a build-up of CO_2, which can cause daytime symptoms such as drowsiness or loss of functioning while seemingly getting enough sleep [1]. It may cause a stroke or a heart attack in more severe cases. There are several surgical and non-surgical treatment options that help to alleviate or remove OSA entirely. The most common treatment is the non-surgical use of a sleeping mask which provides a constant pressurized flow through the airways, removing the possibility of airway collapse. Of these devices, the most common one is the continuous positive airway pressure device (CPAP) which is highly effective when properly used. However, patient compliance is a prominent issue with such devices [2]. These factors leave surgical treatment as a viable option in many cases, although it is more invasive in the short term. Since OSA first was described in the middle of the 10^{th} century [3], there have been many medical advances in surgical treatment options for OSA. Although significant advances have been made in OSA treatment, the outcome of surgery is still not entirely predictable [4, 5]. There have been marginal improvements in some cases, and in more severe cases, OSA has worsened after surgery.

1.1. Fluid Mechanics in OSA

Computational fluid dynamics (CFD) and widely available computed tomography (CT) image segmentation tools have made it possible to create patient-specific 3D models for airway analyses rapidly [6]. Fig. 2 shows a 3D model of the human upper airways of an OSA patient prior to surgery. With appropriate verification and validation, CFD becomes a great and trustworthy tool that makes model testing much faster than its experimental counterpart. Even though computational capacity has seen exponential growth, detailed CFD simulations are still computationally expensive. Using CFD software to acquire accurate and trustworthy results requires an experienced engineer, making it a less viable choice for medical doctors to use in patient-specific cases. The pragmatic simulator developed through Weisz's specialization project [7] and further improved through the master's thesis by the same author [8] is a proposed method for combining the accuracy of CFD with fast simulation and user-friendliness.

1.2. Pragmatic Model

The pragmatic model is a proposed 1D flow simulator that takes in cross-sectional data from the upper airways of a patient with OSA and converts it into a piping system. The area-averaged gauge pressure is calculated using the Bernoulli equation with losses from cross-section to cross-section [9]. The geometrical variations in the geometry lead to additional pressure losses, which are modeled using known relations for pipes and included in the Bernoulli equation with losses. A doctor can perform the pragmatic calculations and the results can give insights into the current state of the patient's airways, and further help determine what type of surgery to perform.

1.3. Hydraulic Diameter

In the pragmatic model described, the unorthodox transformation of the human upper airway cross-sectional geometry to a pipe using the hydraulic diameter has been made. Fig. 1 shows a representation of this transformation for a cross-section in the nasal cavity. Since this approach is not common, validation material is challenging to find. As the airway from the nasopharynx and down has a less complex shape and only one passage, the hydraulic diameter assumption is assumed to be accurate for this anatomical region. Although a validation using the entire geometry would be beneficial, it would yield patient-specific results and might not apply to all OSA patients. It would also be difficult to validate these results since experimental data for velocity and pressure in OSA patients' upper airways are unavailable. This led to the proposal of two simplified test cases used for simulations with the CFD tool Ansys Fluent [10]. The results led to a redefinition of the hydraulic diameter for this specific case after comparison with results from the pragmatic simulation.

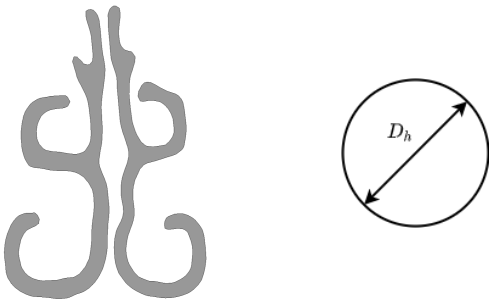

Figure 1: Representation of the conversion from a cross-section in the nasal cavity to a circle with the hydraulic diameter D_h.

2. Theoretical Background

In this paper, the flow simulations from the pragmatic model described in this section are validated using simulations with the commercial CFD software Ansys Fluent. The two simulators have different sets of governing equations solved through the simulations. Both sets of governing equations will be presented in this section of the paper.

2.1. Governing Equations for the Pragmatic Model

The governing equation for the pragmatic model is the Bernoulli equation with losses used to calculate the pressure through the human upper airways. The Bernoulli equation with losses between arbitrary points 1 to 2 along a streamline is given as [9]:

$$\frac{p_1}{\rho g} + \alpha_1 \frac{V_1^2}{2g} + z_1 = \frac{p_2}{\rho g} + \alpha_2 \frac{V_2^2}{2g} + z_2 + h_L \qquad (1)$$

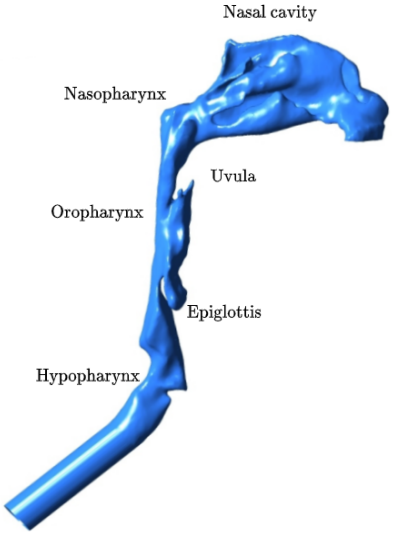

Figure 2: 3D model of the human upper airways adapted from Jordal's master's thesis [11].

where p_1 and p_2 are the pressures and V_1 and V_2 are the velocities at point 1 and 2, respectively. z_1 and z_2 correspond to the height of each point, while α_1 and α_2 are the kinetic energy correction factors. ρ is the density of the fluid and g is the gravitational acceleration. h_L is the loss term which accounts for irreversible losses in the equation. Through solving (1) for the pressure at point 2 and substituting in an index notation, the pressure is given as

$$p_i = p_{i-1} + \rho \frac{\alpha_{i-1} V_{i-1}^2 - \alpha_i V_i^2}{2} + \rho g (z_{i-1} - z_i) - \rho g h_{L,i}, \qquad (2)$$

where $i-1$ and i refer to cross-sections along the same streamline. This pressure corresponds to the gauge pressure in the pragmatic model, as the reference pressure is assumed to be atmospheric.

2.2. Losses

The loss term in equation (1) is comprised of both minor and major losses, where major losses are frictional losses and minor losses are caused by losses from geometrical changes in a pipe [9, p. 364]. The minor losses in the pragmatic simulator are given by

$$h_{L,minor,i} = \sum_{j=1}^{m} K_{L,j} \frac{V_j^2}{2g}, \qquad (3)$$

where j is a geometric component causing a minor loss in section i of the airways and $K_{L,j}$ is its minor loss coefficient. The major loss is given by

$$h_{L,major,i} = f_i \frac{L_i}{D_{h,i}} \frac{V_i^2}{2g}, \qquad (4)$$

where i is the section of the pipe between cross-sections $i-1$ and i. L_i is the length of the section, and $D_{h,i}$ is its hydraulic diameter.

2.3. Diffuser Effect

The minor losses in Eq. (3) include losses that occur due to gradual expansions. Results from the pragmatic simulations show that additional loss modeling may be required in these regions. These additional losses due to

flow separation are modeled through a pressure-recovery coefficient given as [12, p. 398]

$$C_p = \frac{p_e - p_t}{p_{0t} - p_t}, \tag{5}$$

where p_e and p_t are the pressure at the exit and throat of the diverging nozzle respectively and p_{0t} is the stagnation pressure at the throat. To include this as an additional loss it can be solved for p_e after obtaining a value for C_p and adding it to Eq. (2).

2.4. Hydraulic Diameter

The hydraulic diameter is given by the equation

$$D_h = 4 \cdot \frac{A}{P_e}, \tag{6}$$

where A is the cross-sectional area of the geometry and P_e is the wetted perimeter. In the investigation, a variation of the hydraulic diameter is proposed, which is given by

$$D_h = C_{D_h} \cdot \frac{A}{P_e}, \tag{7}$$

where C_{D_h} is the "hydraulic diameter coefficient" which replaces the constant 4 in the original equation.

2.5. Volumetric Flow Rate

The velocity is one of the input variables in Eq. (2) and therefore needs to be calculated. Since the flow rate is known, the velocity can be calculated using the incompressible volumetric flow rate

$$Q = V_i A_i = \text{constant}. \tag{8}$$

In this equation V_i is the velocity and A_i is the cross-sectional area of cross-section i.

2.6. Governing Equations for CFD

In the commercial CFD software Ansys Fluent [10] the Navier Stokes equations are solved on a discretized mesh using the finite volume method. The continuity equation and the momentum equation, which make up the Navier-Stokes equations, are solved for each cell. Since the Mach number is much lower than 0.3, the incompressible variants of the equations have been used. The incompressible continuity equation is given by

$$\frac{\partial u_i}{\partial x_i} = 0, \tag{9}$$

where u_i is the velocity component in the $x_i -$ direction where $i = 1, 2, 3$. The incompressible momentum equation is given by

$$\frac{\partial u_i}{\partial t} + u_j \frac{\partial u_i}{\partial x_j} = f_i - \frac{1}{\rho}\frac{\partial p}{\partial x_i} + \nu \frac{\partial^2 u_i}{\partial x_j \partial x_j}. \tag{10}$$

f_i is the i^{th} component of the gravitational acceleration, where $i = 1, 2, 3$. ν is the kinematic viscosity, which is a constant for this case. Einstein summation is assumed for equations (9) and (10).

3. Methodology

As mentioned in the introduction, converting two ducts into one using the hydraulic diameter is not a common approach. To the knowledge of the authors, this conversion has not been used for flow calculation using the proposed method. Therefore, the procedure is explained in detail in the following section, along with justifications for the choices made.

3.1. Numerical Setup

A simple numerical case was chosen to validate the use of the hydraulic diameter on cross-sections from the human upper airways. For simplicity, a duct was chosen as the foundation of the simplified geometry. A wall was then introduced to the geometry giving the duct a divided geometry, further mimicking the human upper airway geometry in the nasal cavity. The separating wall is the simple geometry's counterpart to the septum, the cartilage which divides the nasal passage in the airways [13]. One of the ducts was created more narrow than the other because of the prevalence of deviated septums in OSA cases. A deviated septum is a deformation of the cartilage and bone wall separating the nasal passages, which impacts the many functions of the nasal cavity [14]. Therefore, the variation in geometry between the two passages in the numerical geometry was implemented to generalize the test case. Fig. 3 shows the setup and the dimensions of the different passages. The length of the wall was chosen to allow the flow to develop while not necessarily becoming fully developed, as the flow in the nasal cavity does not become fully developed due to the short entry length and its varying geometry. Two test cases were chosen since differences will occur in the various patient-specific upper airways. Both of the test cases have the same overall dimensions apart from the leading and trailing ends of the wall. One numerical case has a wedge at the leading and trailing ends of the wall, while the other has flat ends.

3.1.1. Wall with Wedged Ends

In the human upper airways, flow separation is likely to occur at various stages because of the complexity of the geometry. However, for the simple generalizable case presented in this paper, investigating a non-separated flow is of interest, possibly yielding a better base case for future comparison. To avoid flow separation leading into the region with two passages, a 10° wedge is placed in front of the wall. The walls on either side are flat, which effectively leads to an angle of 5° for either passage. For a circular diffuser, flow separation has been found to occur in the range $1000 \leq \text{Re} \leq 4000$ [15] giving a comparable case downstream of the wall. The Reynolds number of the flow in both of the single duct sections, prior to and post the separated passages, was $\text{Re} = 2500$. Although the test case is not circular, it was chosen as a case with a lower chance of separation than its wedge-less counterpart. The dimensions of the computational domain have been taken from the height and width of a nasal cavity cross-section at its largest point. The left figure in Fig. 1 shows the largest cross-section. The largest section of the airways was measured using the 3D geometry from a patient who showed great improvement in OSA post-surgery. The same geometry used [16].

3.1.2. Wall with Flat Ends

An alternative numerical setup to the wedged setup presented in the section above was tested. This alternative setup was proposed to capture flow separation and recirculation which are likely to occur in the complex human upper airways [17]. The alternative setup chosen is identical to Fig. 3 apart from the leading and trailing ends of the separating wall, which in the alternative case are flat. The alternative setup is shown in Fig. 4. The flat leading and trailing ends of the separating wall are hypothesized to cause flow separation and recirculation, similar to the flow structures found in a backward-facing step [18]. This is meant to aid in the validation of the hydraulic diameter by

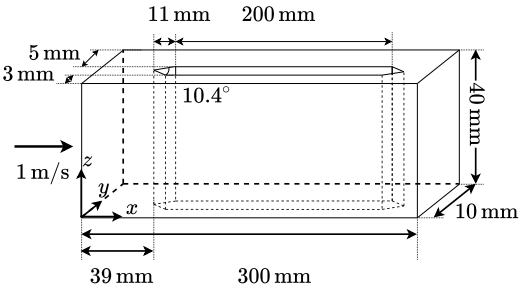

Figure 3: Numerical setup with 10° wedges at both ends of the separating wall.

providing more test data more closely resembling actual human upper airway flow structures.

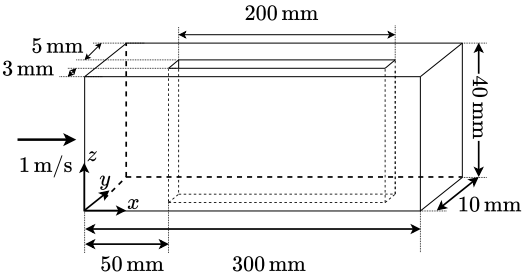

Figure 4: Numerical setup where the leading and trailing ends of the separating wall are flat.

3.2. Inlet and Outlet Boundary Conditions

For both test cases, the boundary conditions at the inlet and outlet, respectively, were the same. In both cases air with a kinematic viscosity of $\nu = 1.6 \cdot 10^{-5}$ was used as the fluid. A fully developed laminar flow was given as the inlet condition. The fully developed flow was found by extending the numerical domain prior to the inlet by an entry length of 800 mm, with a uniform flow of $V = 1$ m/s at the inlet of the extended domain. The entry length was found using the equation for a nondimensional hydrodynamic entry length for a laminar flow [9, p. 342]. The inlet velocity was found by calculating the Reynolds number using the actual human upper airway geometry and is based on a flow rate of 250 mL/s [16]. The outlet condition specified the gauge pressure and is set to 0 Pa at the end of the flow domain. The outer and internal separating walls were treated with no-slip boundary conditions.

3.3. Grid Generation

The mesh for both cases was created using Ansys Meshing [19], a part of the Ansys simulation environment, where all of the simulations were carried out. With the help of the mesh creator and Ansys Workbench [20], several different grid configurations were tested to find a grid that would provide a grid-independent solution. The result from the pragmatic model simulations was the area-averaged gauge pressure. This was a natural quantity to check when performing the mesh independence study. The grid was created by predetermining the number of subdivisions along the outer horizontal edges, the horizontal edges along the separating wall, and the outer vertical edges. To create the mesh, the number of division along the outer edges and along the wall's edges in the x-direction was set to 300, thus giving the numerical domain 300 cells in the x-direction. 8 cells were used in the y-direction and 40 cells were used in the z-direction, both created by setting the number of divisions along the outer edges in their respective directions to 8 and 40 respectively. In Ansys Meshing [19] the behaviour of these sections was set to "hard" to create a structured mesh mostly containing hexahedral cells. This meshing scheme made it possible to generate meshes at different scales with the same proportions in a controllable way. Different resolutions for the mesh were created and simulated while controlling the selected parameter, the gauge pressure. The meshes with a slightly coarser resolution gave similar pressure values for the control plane. Therefore, the mesh with a higher number of cells was chosen for further simulations since the control parameter remained reasonably constant. The mesh independence study was only performed on the numerical domain with a 10° wedge. The same grid generation technique and resolution were applied to the case with flat wall ends.

3.4. Tuning the Hydraulic Diameter

Altering the hydraulic diameter given by Eq. (6) is proposed to match the results from the CFD investigations more accurately. A novel method to tune this parameter was to define a hydraulic diameter coefficient, C_{D_h}. The hydraulic diameter coefficient replaces the constant, 4, in Eq. (6) to obtain a new equation given by (7) allowing the possibility to find a coefficient that better represents the present case. The method involved running the CFD simulations described in this paper along with the pragmatic simulations and comparing the results from both. The pragmatic simulations' input were the flow rate, cross-sectional area and the wetted perimeter from evenly spaced cross-sections along the numerical geometries. The pragmatic model was modified only to include the frictional losses introduced through the major loss term in Eq. (4)when validating the hydraulic diameter. The hydraulic diameter is present in both the Reynolds number and the loss term itself, leading to a negative squared inverse correlation between the pressure and the hydraulic diameter. This correlation implies that a decrease in the hydraulic diameter leads to a decrease in the pressure slope. Pragmatic simulations were run for hydraulic diameter coefficients in the range $3 \leq C_{D_h} \leq 4.2$ to compare the CFD simulations and the pragmatic simulations. The residual sum of squares (RSS)[21] was calculated for each pragmatic simulation. The equation for RSS is given by

$$RSS = \sum_{i=1}^{n} (y_i - f(x_i))^2, \tag{11}$$

where y_i is the i^{th} component of the value to be predicted (the area-averaged gauge pressure from CFD simulation) and $f(x_i)$ is the i^{th} component of the predicted value (the area-averaged gauge pressure from the pragmatic model). The RSS value was calculated using pragmatic and CFD gauge pressures from the middle of the wall to the end of the walled section, i.e. $150\,\text{mm} \leq x \leq 200\,\text{mm}$ in Fig. 3 and Fig. 4. This was done to reduce the impact of inaccuracies in the error estimation in the entrance regions of the split geometries. In these regions, deviations are expected due to the simple nature of the pragmatic simulations. The hydraulic diameter coefficients could then be obtained by minimizing the error in this region.

3.5. Minor Losses and Diffuser Effects

With the pragmatic model using loss relations known from piping systems, the accuracy of these relations is important. An effect seen in the results of the pragmatic simulations is a nonphysical pressure recovery where the human upper airway geometry has an expansion. The relations for expansions used in the pragmatic model did not accurately model the pressure difference seen in the CFD simulations [8]. Therefore, it was proposed that the effects of flow separation were more significant than initially thought. To further investigate this increased flow separation and model it accurately, the effects were included in the validation simulations presented in the present paper. This was implemented at the end of the walled section, where the nasal passages coincide. The Bernoulli equation with losses Eq. (1) takes flow separation into account though minor losses given by Eq. (3). However, the pressure recovery found through the pragmatic flow simulations was too large. This occurs when the two passages in the geometry coincide downstream of the separating wall and there is an increase in the cross-sectional area for both passages. This effect can be taken into account through added diffuser losses for these sections. These losses were calculated using Eq. (5) by using the CFD gauge pressure to calculate the pressure recovery coefficient C_p, using Eq. (5). The exit pressure, p_e, in Eq. (5) was the CFD gauge pressure from the cross-section downstream of the expansion, and the throat pressure, p_t, in Eq. (5) was the gauge pressure from the cross-section upstream of the same expansion. The calculated C_p values for the expanding sections were included in the pragmatic model by solving Eq. (5) for the exit pressure p_e using the area-averaged gauge pressure from the pragmatic model, p_{i-1}, as the throat pressure, p_t. This was used as p_i in the pragmatic model instead of using Eq. (2) to calculate p_i for this section, leading to a larger, more physically accurate pressure loss in the relevant region.

3.6. Verification of the Numerical Code

A crucial part of any CFD simulation is verifying the accuracy of the code used for simulations. In the present case, this step was done through a simplification of the numerical domain. The 3D domain was simplified to a 2D domain with the same height as the 3D domain, 40 mm, and long enough for the flow to become fully developed. The fully developed flow was found by using a domain which was 7000 mm in length, giving the flow the opportunity to become fully developed. The grid for the verification case was created using Ansys Meshing [19], where a structured grid with rectangular cells was created. The mesh had 1000 cells in the flow direction, where a bias which decreased the cell size from the inlet to the outlet was included to achieve similar cell dimensions as in the 3D case towards the end of the domain. 40 cells were used in the y-direction with even spacings. The inlet velocity was chosen to be $V = 1$ m/s to achieve a Reynolds number of $\mathrm{Re} = 2500$ using the height of the domain as the length scale and $\nu = 1.6 \cdot 10^{-5}$ as the kinematic viscosity. The simulations were carried out using Ansys Fluent [10], using the same settings as the full 3D simulations. The results from the verification were compared to the analytical solution of a plane Poiseuille flow [9, p. 468]. Fig. 5 compares the two solutions and shows a high degree of accuracy in the numerical simulations compared to the analytical solution. Fig. 5 also shows the development of the flow, at the locations $x = 0.05, 2$ and 6.9 m, where x is the downstream distance from the inlet located at $x = 0$ m. The flow profiles show an expected development with the flow reaching its fully developed state at $x = 6.9$ m. Since these results correspond to their analytical counterpart, the solver was considered an accurate enough standard for further numerical investigation.

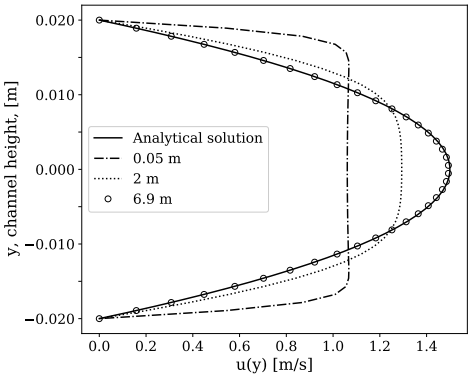

Figure 5: Fluid flow profiles at the locations $0.05, 2$ and 6.9 m downstream from the inlet. The flow profile reaches the analytical solution close to the end of the simulation domain, $x = 6.9$ m. The analytical solution is given for a fully developed plane Poiseuille flow.

3.7. Pragmatic Simulations

The pragmatic simulations were run using input data found using the numerical geometries. The area-averaged gauge pressure was extracted when the CFD simulations were completed. The pressure was extracted at evenly spaced cross-sections along the length of the numerical domain. The pragmatic model's input for each location is the cross-sectional area, the perimeter and the flow rate for the given simulation. The cross-sectional area and the perimeter of each cross-section were calculated based on the numerical geometries' dimensions shown in Fig. 3 and Fig. 4, the extracted values are shown in Tab. 1. The flow rate was calculated using the area-averaged input velocity $V = 1$ m/s. The flow rate could then be converted into the velocity at the various cross-sections in the wall-separated region using equation (8). The pragmatic simulations were then carried out and the area-averaged gauge pressure from both the pragmatic simulations and the CFD simulations could be compared.

Table 1: Cross-sectional area and perimeter calculated using dimensions from Fig. 3 and Fig. 4, where the dimensions at $x = 45$ mm only apply to the wedged case.

x [mm]	A [mm^2]	P_e [mm]
0	400	100
45	356.36	177.82
150	320	176

4. Results and Discussion

The results from the validation simulations are to be applied to the pragmatic model to accurately represent the flow through predicting the area-averaged gauge pressure. The area-averaged gauge pressure from the pragmatic simulations and the CFD simulations are compared to assess the accuracy of the standard hydraulic diameter Eq. (6) and find an accurate fit for the hydraulic diameter coefficient C_{D_h} in Eq. (7). Fig. 6 and 7 show the results from both simulations along with the initial pragmatic results using Eq. (6), which are the

uppermost curves The initial results revealed deviations from the CFD simulations, most notably the slope of the area-averaged gauge pressure. The slope of the pragmatic curve was initially too flat and was altered through varying the hydraulic diameter coefficient C_{D_h}. In the Bernoulli equation with losses (1) the hydraulic diameter D_h is inversely correlated to he pressure through its representation in the loss term h_L, given by Eq. (4). However, as the term is negatively signed, the pressure gradient and the hydraulic diameter become correlated, leading to predictable changes when tuning the coefficient C_{D_h}. Changing the hydraulic diameter coefficient and introducing losses from the pressure-recovery coefficient gave more accurate results when compared to the CFD simulations. The effects on the pragmatic model from both of the numerical validation cases are presented and discussed in the following subsections.

4.1. Wall with Wedged Ends

Fig. 6 shows the results from both the CFD simulations and the pragmatic simulations in the case where the wedge is present. The results show an expected decline in the area-averaged gauge pressure through the geometry. The pragmatic simulations have a linearly decreasing pressure in the middle section, where the separating wall is located, but with varying slopes. The CFD simulation has a less linear shape in the section with the separating wall. However, it has a linear trend further downstream. Compared to the CFD simulations, it has a slight additional pressure loss as the duct is split up, and a slight pressure gain at the opposite side. The initial pragmatic results have similar trends but with inflated loss values as well as pressure gain. Using the error minimization approach described in the methodology section, $C_{D_h} = 3.73$ was found as the optimal hydraulic diameter coefficient. A visualization of the optimization is shown in Fig. 8. The pressure-recovery coefficient was calculated by applying pressure values from the CFD simulations to Eq. (5). This showed an improvement in accuracy downstream of the walled section.

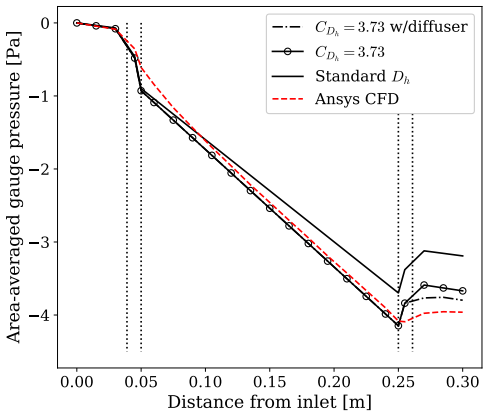

Figure 6: Results from Ansys Fluent and corresponding pragmatic simulations for simulations with a 10° wedge at both ends of the separating wall. The vertical dotted lines indicate the wedge locations.

4.2. Wall with Flat Ends

The alternative flow situation used to study the hydraulic diameter is also investigated. For this case, the separating wall has flat ends instead of wedges. The aim of this was to study the effects of tuning the hydraulic diameter coefficient, C_{D_h}, and comparing it to the wedged case to find out how the hydraulic diameter coefficient would deviate from the initial results. This was to study the reliability and generalizability of the results obtained in the wedged case. The results from these simulations are displayed in Fig. 7. Minimizing the RSS value for these simulations gave $C_{D_h} = 3.69$ as the hydraulic diameter coefficient with the highest accuracy. Similarly to the case with 10° wedges, applying the increased pressure recovery coefficient to the pragmatic simulations gave a result closer to the CFD simulations. Due to the nature of the geometry with its sudden geometrical changes, the pragmatic model has sudden pressure changes at the beginning of the walled section and at the end, with a pressure loss and a pressure gain respectively. The same procedure for finding the pressure recovery coefficient was used. In the case with flat ends, this gave a highly accurate result. This implies that there is more flow separation in the non-wedged case. However, this increased accuracy may be due to the sudden changes, which make the pressure recovery coefficient from the CFD simulations easier to find. The increased accuracy using the pressure recovery coefficient in the wedge versus the non-wedged case is thus inconclusive. However, the use of a pressure recovery coefficient in general is promising.

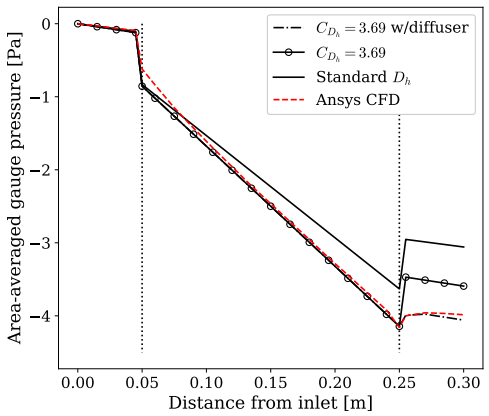

Figure 7: Results from Ansys Fluent and corresponding pragmatic simulations for the simulations with flat ends of the separating wall.

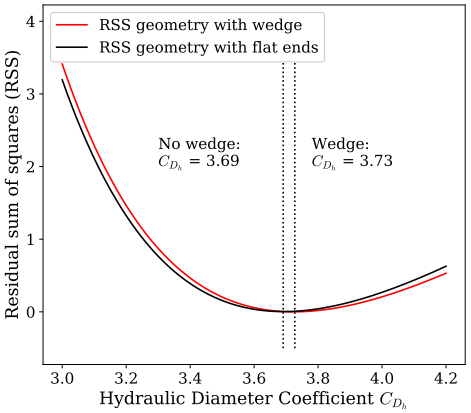

Figure 8: Calculations of the RSS values for simulations with and without a 10° wedge at the ends of the wall.

4.3. OSA Patient's Upper Airways Simulations

The aim of finding an improved version of the hydraulic diameter is to implement the improved version in the pragmatic model and achieve better results when simulating the flow the actual upper airways of an OSA patient. The results of implementing the averaged value of the two hydraulic diameter coefficients into the pragmatic model are shown in Fig. 9. In this figure the cutplanes correspond to the cutplanes from Fig. 10, which indicate the locations the results from the CFD simulations are taken from. The cross-sectional area and perimeter used as input for the pragmatic model have been extracted from the same 3D model at the numbered locations. The results with $C_{D_h} = 3.71$ in Eq. (7) only show a marginal improvement compared to using Eq. (6). The alternative hydraulic diameter coefficient, C_{D_h}, was applied to the first four cutplanes prior to the coinciding of the nasal passages indicated by the dashed and dotted line in Fig. 9, the standard hydraulic diameter $C_{D_h} = 4$ was used downstream of this. Further analyses showed that a more accurate coefficient for the human upper airways is given by $C_{D_h} = 1.80$. One of the reasons for this deviation is that the simple nature of the geometries analysed in this paper are better modeled by the a value closer to the original hydraulic diameter. The hydraulic diameter is meant for square ducts and other simple geometries, thus increasing the complexity of the geometry requires decreasing the hydraulic diameter.

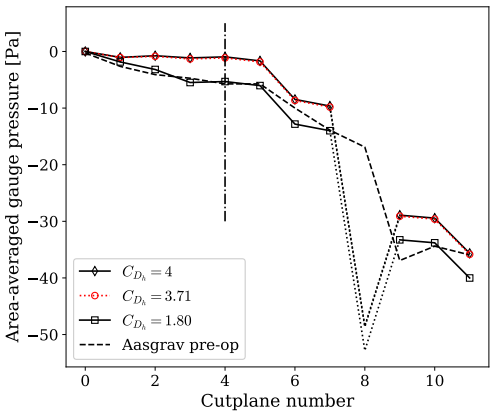

Figure 9: Pragmatic model simulations with cross-sections from Fig. 2 as input verified using CFD simulation performed through Aasgrav's specialization project [16]. The dashed and dotted line indicates where the nasal passages coincide.

5. Conclusions

As a part of creating a pragmatic flow simulator, the hydraulic diameter is used to transform the human upper airway geometry into a piping system. A test case has been created and presented in this paper to determine if this is a valid assumption to make in the nasal cavity. The test case used two variations of a simple duct-like geometry with a single duct to begin with, which goes over to a split up section with a separating wall between two passages and a coinciding geometry at the end of the wall. The simulations were performed assuming a laminar steady incompressible airflow that with a uniform velocity of 1 m/s at the inlet of the numerical domain. The results from these simulations showed the expected decline in the area-averaged gauge pressure over the length of the geometry. The resulting pressure curve was used as a basis for comparison to the pragmatic flow simulations. Pragmatic flow simulations were executed, with the only loss contribution being the frictional losses. Comparing

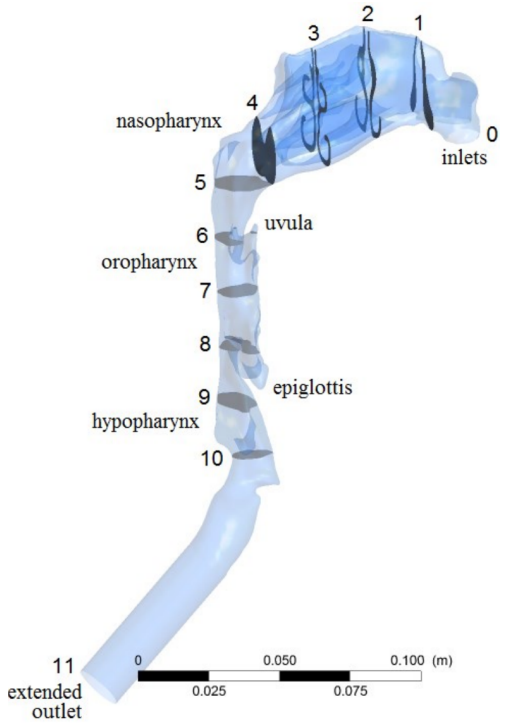

Figure 10: Locations of cutplanes used for the extraction of the area-averaged gauge pressure in the CFD investigation of the human upper airways [16].

the results to the CFD simulations proved that the pressure slope generated by the pragmatic simulator was a little off. Analysing different values of the hydraulic diameter coefficient C_{D_h} for the two test cases presented gave two slightly different values. The two values were $C_{D_h} = 3.72$ and $C_{D_h} = 3.69$ for the case with and without a wedge at the leading and trailing ends of the wall respectively. Averaging the two values and implementing the new equation given by $D_h = 3.71 \cdot \frac{A}{P_e}$ into the pragmatic model hardly improved its accuracy for flow in the upper airways of an OSA patient. However, $C_{D_h} = 1.80$ in the pragmatic model proved to give good agreement of the pressure with the CFD results. This investigation proved that the accuracy of the pragmatic simulations could be improved by altering the hydraulic diameter coefficient C_{D_h}. To conclude, the coefficients found through this study did not provide accurate results on the actual human upper airway, but imply that altering the hydraulic diameter can lead better accuracy. This implies that the redefinition of the hydraulic diameter proposed in this study can be used as an optimization parameter in the pragmatic model.

References

[1] N. M. Punjabi, "The epidemiology of adult obstructive sleep apnea," *Proceedings of the American Thoracic Society*, vol. 5, no. 2, pp. 136–143, 2008.

[2] A. M. Sawyer, N. S. Gooneratne, C. L. Marcus, D. Ofer, K. C. Richards, and T. E. Weaver, "A systematic review of CPAP adherence across age groups: clinical and empiric insights for developing CPAP adherence interventions," *Sleep Medicine Reviews*, vol. 15, no. 6, pp. 343–356, 2011.

[3] T. Gharibeh and R. Mehra, "Obstructive sleep apnea syndrome: natural history, diagnosis, and emerging treatment options," *Nature and Science of Sleep*, vol. 2,

p. 233, 2010.

[4] E. J. Kezirian, E. M. Weaver, B. Yueh, R. A. Deyo, S. F. Khuri, J. Daley, and W. Henderson, "Incidence of serious complications after uvulopalatopharyngoplasty," *The Laryngoscope*, vol. 114, no. 3, pp. 450–453, 2004.

[5] M. Friedman, R. Vidyasagar, D. Bliznikas, and N. Joseph, "Does severity of obstructive sleep apnea/hypopnea syndrome predict uvulopalatopharyngoplasty outcome?," *The Laryngoscope*, vol. 115, no. 12, pp. 2109–2113, 2005.

[6] S. K. Kim, Y. Na, J.-I. Kim, and S.-K. Chung, "Patient specific CFD models of nasal airflow: overview of methods and challenges," *Journal of Biomechanics*, vol. 46, no. 2, pp. 299–306, 2013.

[7] T. G. Weisz, "Pragmatic modeling of flow in the human upper airways," specialization project, NTNU, 2021.

[8] T. G. Weisz, "Pragmatic modeling of flow in the human upper airways for sleep apnea treatment," master's thesis, NTNU, 2022.

[9] Y. A. Cengel and J. M. Cimbala, *Fluid Mechanics: Fundamentals and Applications, 2^{nd} ed.* McGraw Hill, 2010.

[10] ANSYS, Inc, *Ansys® Fluent, 2021R2, User's Guide*, 2021.

[11] M. R. Jordal, S. G. Johnsen, S. K. Dahl, and B. Müller, "Patient Specific Numerical Simulation of Flow in the Human Upper Airways for Assessing the Effect of Nasal Surgery," *Progress in Applied CFD - CFD - 2017*, pp. 153–162, 2017.

[12] F. M. White, *Fluid Mechanics, 6^{th} ed.* McGraw Hill, 2008.

[13] C. Matthias, "Surgery of the nasal septum and turbinates," *GMS Current Topics in Otorhinolaryngology, Head and Neck Surgery*, vol. 6, 2007.

[14] N. Fettman, T. Sanford, and R. Sindwani, "Surgical management of the deviated septum: techniques in septoplasty," *Otolaryngologic Clinics of North America*, vol. 42, no. 2, pp. 241–252, 2009.

[15] E. Sparrow, J. Abraham, and W. Minkowycz, "Flow separation in a diverging conical duct: Effect of reynolds number and divergence angle," *International Journal of Heat and Mass Transfer*, vol. 52, no. 13-14, pp. 3079–3083, 2009.

[16] E. Aasgrav, "CFD Simulations of Turbulent Flow in the Human Upper Airways," master's thesis, NTNU, 2017.

[17] T. B. Martonen, L. Quan, Z. Zhang, and C. Musante, "Flow simulation in the human upper respiratory tract," *Cell Biochemistry and Biophysics*, vol. 37, no. 1, pp. 27–36, 2002.

[18] T. Lee and D. Mateescu, "Experimental and numerical investigation of 2D backward-facing step flow," *Journal of Fluids and Structures*, vol. 12, no. 6, pp. 703–716, 1998.

[19] ANSYS, Inc, *Ansys® Meshing, 2021R2, ANSYS Meshing User's Guide*, 2021.

[20] ANSYS, Inc, *Ansys® Workbench, 2021R2, User's Guide*, 2021.

[21] Wikipedia contributors, "Residual sum of squares — Wikipedia, the free encyclopedia," 2022. [Online; accessed 29.05.2022].

B Python Code

```
from matplotlib.markers import MarkerStyle
import numpy as np
import pandas as pd
import matplotlib.pyplot as plt
from functions import friction_factor
from matplotlib_rcParams import *
from scipy.optimize import fsolve
from scipy.interpolate import interp1d
basic_plot(plt)


class Model:
"""
Main class for 1D pragmatic flow simulations.
"""
    # Constants
    g = 9.81                # [m/s^2]  gravitational acceleration
    rho = 1.25              # [kg/m^3] air density
    nu = 1.48e-5            # [m^2/s]  kinematic viscosity
    q = 250*10**-6          # [m^3/s]  volumetric flow rate


    def __init__(self, data, hydraulic_diameter_coefficient=4,
        result_data = 'none'):
        """
        Input to begin with is a DataFrame which must contain the
        Area and Perimeter for all cross-section for which the pressure
        is to be calculated.
        """
        # If the input data is a DataFrame
        self.data = data
        self.length = len(data)
        self.A = data.area
        self.perimeter = data.perimeter
        self.distance = data.distance
        self.P = []                     # Local gauge pressure
        self.V = []                     # Local velocity
        self.hl_minor = []              # Minor losses: h_L
        self.hl_major = []              # Major losses; frictional losses
        self.Re = []                    # Local velocity
        self.Dh = []                    # Hydraulic diameter
        self.added_losses = []

        self.diffuser = []                # Diffuser
```

```
        self.cp = []
        self.f = []
        self.d_coeff = hydraulic_diameter_coefficient
        self.d_coeff2 = 4

        self.initialize_V_Dh_Re()
        if isinstance(result_data, pd.DataFrame):
            self.calculate_cp_from_df(df=result_data)


    def simulate(self, turbulence_model="laminar", epsilon=0.2,
        diffuser=False, include_minor=True):
        """
        The main simulation loop of the pragmatic model. All calculations
        and supporting funtions for the calculations are either carried
        out or performed in this atribute.
        """
        self.diffuser.append(0)
        self.set_P_hl_boundary()
        L = self.distance
        g = Model.g
        total_losses = 0

        for i in range(1, self.length):
            Re_avg = (self.Re[i] + self.Re[i - 1])/2
            D_avg =  (self.Dh[i] + self.Dh[i - 1])/2
            V_avg =  (self.V[i] +  self.V[i - 1])/2

            # Major Losses
            self.f.append(self.friction_factor(turbulence_model,
                Re_avg, D_avg, epsilon))
            self.hl_major.append(self.f[i] *
                (L[i] - L[i-1])/D_avg * V_avg**2/(2*g))

            # Minor Losses
            if include_minor:
                minor_losses = 0
                minor_loss_object = Minor_losses(self.Dh[i-1], self.Dh[i],
                                    self.V[i-1], self.V[i], L[i]-L[i-1])
                minor_losses = minor_loss_object.find_losses()
                hl = minor_losses*V_avg**2 / (2*self.g)
                self.hl_minor.append(hl)
            else:
                self.hl_minor.append(0)

            if diffuser:
                diff = self.diffuser_from_cp(self.V[i-1],
                    self.cp_perfect_diffusor(i))
```

```
            else:
                diff = 0
            self.diffuser.append(diff)
            # Total Losses
            total_losses += (self.hl_minor[i] + self.hl_major[i])

            loss_term = (self.hl_minor[i] + self.hl_major[i])*
                        self.rho*self.g
            a = 2
            bernoulli_term = (a * self.V[i - 1]**2 - a * self.V[i]**2)
                           *self.rho/2

            pressure = self.P[i-1] + bernoulli_term - loss_term - diff

            self.P.append(pressure)



    # Initialization and pre-calculation atributes
    def initialize_V_Dh_Re(self):
        """
        Atribute to calculate the velocity,
        hydraulic diameter and Reynolds number.
        """
        for i in range(self.length):
            self.V.append(self.calculate_velocity(self.A[i], self.q))
            if i < 4:
                self.Dh.append(self.calculate_hydraulic_diameter(
                            self.d_coeff, self.A[i], self.perimeter[i]))
            else:
                self.Dh.append(self.calculate_hydraulic_diameter(
                            self.d_coeff2, self.A[i], self.perimeter[i]))
            self.Re.append(self.calculate_Reynolds(self.V[i],
                            self.Dh[i]))


    def calculate_velocity(self, area, flow_rate) -> float:
        """ Calculate the velocity given an area and a flow rate."""
        return flow_rate/area

    def calculate_hydraulic_diameter(self, d_coeff, area, perimeter)
                                    -> float:
        """
        Calculate the Hydraulic Diameter given an area and
        a perimeter and, optionally a hydraulic diameter coefficient.
        """
        return d_coeff*area/perimeter
```

```
    def calculate_Reynolds(self, velocity, diameter):
        """ Calculate the Reynolds number from the velocity,
        the diameter and the kinematic viscosity """
        return velocity*diameter/self.nu

    def set_P_hl_boundary(self):
        """Set the initial values of all
            the lists included in the model."""
        if(len(self.P) == 0):
            self.P.append(0)
            self.hl_minor.append(0)
            self.hl_major.append(0)
            self.f.append(0)

    def friction_factor(self, turbulence_model, Re, Dh=None,
                        epsilon=None) -> float:
        """Calculates the friction factor,
        There are three possibilities for model:
            'laminar', 'haaland', 'colebrook'
            """
        if turbulence_model == "laminar":
            res = 64/Re

        elif turbulence_model == "haaland":
            temp = -1.8*np.log10(6.9/Re + ((epsilon/Dh)/3.7)**1.11)
            res = (1/temp)**2

        elif turbulence_model == "colebrook":
            # Using Haaland as a starting point for the iterations.
            temp = -1.8*np.log10(6.9/Re + ((epsilon/Dh)/3.7)**1.11)
            x0 = (1/temp)**2

            def fr(f, epsilon=epsilon, Dh=Dh, Re=Re):
                return 2*np.log10((epsilon/Dh)/3.7 +
                            2.51/(Re*np.sqrt(f))) + 1/np.sqrt(f)
            res = fsolve(fr, x0)

        else:
            pass
        return res


    # Result visulization
    def plot_pressure(self, other='none', fig_size=(11, 6),
            title='none', x_axis='none', res=True):
        """
        Plot method.
        Plots the pressure from the current simulation.
```

```
        other: Optional Dataframe which can also be plotted, this
        """
        fig, ax = plt.subplots(figsize=fig_size)
        ax.set_ylabel("Area-averaged gauge pressure")
        ax.set_xlabel(x_axis)

        # **kwargs
        if x_axis == 'distance':
            ax.plot(self.distance, self.P, '-o', color='r',
                label="Base plot")
        elif x_axis == 'none':
            ax.plot(self.P, '-o', color='r', label="Base plot")

        if isinstance(other, pd.DataFrame):
            ax.plot(other.pressure, color='black', label="CFD pressure")

        plt.legend()
        if res:
            return fig, ax

    def plot_multiple(self, *other, type="pressure", fig_size=(11,6),
        include_self=True, labels='none', dropindex='none', cfd_first=True,
        guide_line='none',
                        xlabel="", ylabel="", title="") -> None:
        """Docstring"""
        colors = ["black", "b", "g", "m", "b", "g", "m"]
        style = ["-", "-.", "--", "-", "-.", "--", "-"]
        shapes = ["", "o", "s", "d", "o", "s", "d"]

        fig, ax = plt.subplots(figsize=fig_size)
        ax.set_xlabel(xlabel)
        ax.set_ylabel(ylabel)
        ax.set_title(title)

        if include_self:
            ax.plot(self.P, '-o', color='r', label="Test Label")

        for i, df in enumerate(other):
            if labels != 'none':
                label = labels[i]
            else:
                label = 'none'
            if i == 0 and cfd_first:
                ax.plot(df.pressure, color='black', label="CFD Pressure")
            else:
                if isinstance(dropindex, int):
                    ax.plot(df.pressure[:dropindex], color=colors[i],
                        label=label, marker=shapes[i])
```

```
                ax.plot([dropindex-1, dropindex, dropindex+1],
                        [df.pressure[dropindex-1], df.pressure[dropindex],
                        df.pressure[dropindex+1]], linestyle=':', color='b')
                ax.plot(df.pressure[(dropindex+1):],
                        color=colors[i],marker=shapes[i])
            else:
                ax.plot(df.pressure, label=label, linestyle=style[i],
                        color=colors[i])

    if isinstance(guide_line, int):
        ax.plot([guide_line, guide_line], [-30, 5], 'r-.')
    ax.plot([0, 0.0001], [0, -0.0001],  linestyle=':', color='b',
        label="Non-comparable cross-section")
    plt.legend()

# Output atributes
def to_DataFrame(self) -> pd.DataFrame:
    """ Converts the result data to a Pandas DataFrame."""
    output_dict =   {   "V":            self.V,
                        "area":         self.A,
                        "perimeter":    self.perimeter,
                        "distance":     self.distance,
                        "Dh":           self.Dh,
                        "Re":           self.Re,
                        "pressure":     self.P,
                        "hL_major":     self.hl_major,
                        "hL_minor":     self.hl_minor,
                        "friction":     self.f,
                        "Diffusor":     self.diffuser  }
    output_DataFrame = pd.DataFrame.from_dict(output_dict)
    return output_DataFrame

# Diffuser calculation atributes
def diffuser_from_cp(self, V, cp) -> float:
    """Calculates the pressure value from a given cp.

    Args:
        V (float): velocity
        cp (float): diffuser coefficient

    Returns:
        float: Calculated pressure value from the givencp.
    """
    return (0.5*self.rho*V**2)**2*cp

def calculate_cp_from_df(self, df):
    assert(len(df) == len(self.V))
    for index, row in df.iterrows():
```

```
            if index < (len(df) -1 ):
                cp = df.loc[index + 1,"pressure"] -
                    df.loc[index, "pressure"]
                self.cp.append(cp)
            else:
                self.cp.append(0)

    def cp_perfect_diffusor(self, index)->float:
        """Manually add the diffuser effect to the relevant
            sections of the model."""
        if index == 7:
            cp = 0.5
        elif index == 9:
            cp = 0.03
        elif index == 4:
            cp = 0.13
        else:
            cp = 0
        return cp

    # Future functions: adding data
    def add_nasal_data(self, data):
        pass

    def add_pharynx(self, data):
        pass


    def add_minor_losses(self, minor_loss_dict):
        for index in minor_loss_dict:
            self.hl_minor[index] += minor_loss_dict[index]

        pressure_delta = 0
        for i, p in enumerate(self.P):
            if self.hl_minor[i] > 0:
                if self.V[i-1] > self.V[i]:
                    V = self.V[i-1]
                else:
                    V = self.V[i]
                self.hl_minor[i] = self.hl_minor[i]*V**2/(2*self.g)
                pressure_temp = self.hl_minor[i]*self.rho*self.g
            else:
                pressure_temp = 0

            pressure_delta += pressure_temp
            self.P[i] -= pressure_delta
```

```
    def add_specific_diffuser(self, diffuser_dict) -> None:
        """Includes a specific diffuser value at a specified
        location in
            the human upper airway geometry.

        Args:
            diffser_dict (dictionary): contains the index
            location and the corresponding diffuser value

        Raises:
            Exception: _description_
        """
        for index in diffuser_dict:
            self.diffuser[index] = diffuser_dict[index]

        pressure_delta = 0
        for i, p in enumerate(self.P):
            if self.diffuser[i] > 0:
                pressure_temp = self.diffuser_from_cp(self.V[i-1],
                    self.diffuser[i])
            else:
                pressure_temp = 0

            pressure_delta += pressure_temp
            self.P[i] -= pressure_delta
```

```
class Minor_losses:
    """
    Class where all minor loss calculations are performed.
    """
    def __init__(self, Dh1, Dh2, V1, V2, dL, loss_type='none',
                 alpha=1):
        """ Calculate the minor loss for a section of the model.
            Valid loss_type strings are:
            'sudden expansion', 'sudden contraction', 'bend45',
            'bend90'
        """
        self.dL = dL
        self.Dh1 = Dh1
        self.Dh2 = Dh2
        self.V1 = V1
        self.V2 = V2
```

```
        self.loss_type = loss_type
        self.alpha = alpha
        self.valid_loss = ['sudden expansion',
            'sudden contraction', 'bend45', 'bend90', 'none']
        self.check_input()

    def check_input(self):

        if self.loss_type not in self.valid_loss:
            raise Exception(f'Loss type "{self.loss_type}"
                is not valid, valid loss types: {self.valid_loss}')

    def find_losses(self, loss_type='none'):
        """ Determine which method to use to calculate the
            minor losses.
        """
        self.loss_type = loss_type
        self.check_input()

        if self.loss_type == "bend45":
            return 0.3
        elif self.loss_type == "bend90":
            return 0.5

        if self.Dh2 > self.Dh1:
            if self.loss_type == "sudden expansion":
                res = self.sudden_expansion(self.alpha)
            else:
                res = self.gradual_expansion()
        elif self.Dh1 > self.Dh2:
            if self.loss_type == "sudden contraction":
                res = self.sudden_contraction(self.alpha)
            else:
                res = self.gradual_contraction()
        else:
            res = 0

        return res

    def sudden_expansion(self, alpha):
        dr = self.Dh1/self.Dh2
        return alpha * (1-(dr)**2)**2

    def sudden_contraction(self, alpha):
        dr = self.Dh2/self.Dh1
        if dr <= 0.76:
            return alpha * 0.42*(1 - dr**2)
        else:
```

```
            return self.sudden_expansion(dr, alpha)

    def gradual_expansion(self):
        """ Gradual expansion for a conical section."""
        theta = self.angle(method="expansion")
        return 0
        return 2.61*np.sin(theta)*(1 - (self.Dh1/self.Dh2)**2)**2

    def gradual_contraction(self):
        """ Gradual contraction for a conical section. """
        theta = 2*self.angle(method="contraction")*360/(2*np.pi)
        #print(f'theta = {theta}')
        KL_con = interp1d([20, 30, 45, 60], [0.01, 0.02, 0.04, 0.07])
        if (theta <= 30) or (theta >= 60):
            return 0
        else:
            return(KL_con(theta))

    def angle(self, method="expansion"):
        """ Calculate angle for a conical expansion or contraction
            with an angle of 2*theta"""
        if method == "expansion":
            return np.arctan(0.5*(self.Dh2-self.Dh1)/self.dL)
        elif method == "contraction":
            return np.arctan(0.5*(self.Dh1 - self.Dh2)/self.dL)
```

C Ansys Fluent Settings and Solution Report

ANSYS 2021 R1

Ansys Fluent Simulation Report

Analyst	tgweisz
Date	6/9/2022 04:29 PM

Table of Contents

1 System Information
2 Geometry and Mesh
  2.1 Mesh Size
  2.2 Mesh Quality
  2.3 Orthogonal Quality
3 Simulation Setup
  3.1 Physics
    3.1.1 Models
    3.1.2 Material Properties
    3.1.3 Cell Zone Conditions
    3.1.4 Boundary Conditions
    3.1.5 Reference Values
  3.2 Solver Settings
4 Run Information
5 Plots

System Information

Application	Fluent
Settings	3d, double precision, pressure-based, laminar
Version	21.1.0-10179
Source Revision	49a2c352da
Build Time	Nov 20 2020 15:49:32 EST
CPU	Intel(R) Core(TM) i7-8700
OS	Windows

Geometry and Mesh

Mesh Size

Cells	Faces	Nodes
215120	693984	264015

Mesh Quality

Name	Type	Min Orthogonal Quality	Max Aspect Ratio
fff_main_component	Mixed Cell	0.33152636	13.284712
fff_entry	Hex Cell	1	1.7320508
fff_exit	Hex Cell	0.9999999	1.7390877

Orthogonal Quality

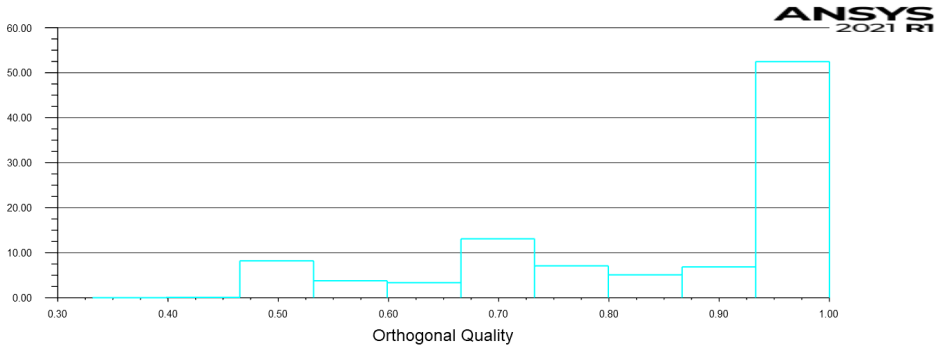

Simulation Setup

Physics

Models

Model	Settings
Space	3D
Time	Steady
Viscous	Laminar

Material Properties

− Fluid	
− air	
Density	1.225 kg/m^3
Cp (Specific Heat)	1006.43 J/(kg K)

Thermal Conductivity	0.0242 W/(m K)
Viscosity	1.7894e-05 kg/(m s)
Molecular Weight	28.966 kg/kmol
Thermal Expansion Coefficient	0
Speed of Sound	none
− Solid	
− aluminum	
Density	2719 kg/m^3
Cp (Specific Heat)	871 J/(kg K)
Thermal Conductivity	202.4 W/(m K)

Cell Zone Conditions

− Fluid	
− fff_main_component	
Material Name	air
Specify source terms?	no
Specify fixed values?	no
Frame Motion?	no
Porous zone?	no
3D Fan Zone?	no
− fff_entry	
Material Name	air
Specify source terms?	no
Specify fixed values?	no
Frame Motion?	no
Porous zone?	no
3D Fan Zone?	no
− fff_exit	
Material Name	air

Specify source terms?	no
Specify fixed values?	no
Frame Motion?	no
Porous zone?	no
3D Fan Zone?	no

Boundary Conditions

— Inlet	
— inlet	
Velocity Specification Method	Magnitude, Normal to Boundary
Reference Frame	Absolute
Velocity Magnitude [m/s]	1
Supersonic/Initial Gauge Pressure [Pa]	0
— Outlet	
— outlet	
Backflow Reference Frame	Absolute
Gauge Pressure [Pa]	0
Pressure Profile Multiplier	1
Backflow Direction Specification Method	Normal to Boundary
Backflow Pressure Specification	Total Pressure
Build artificial walls to prevent reverse flow?	no
Radial Equilibrium Pressure Distribution	no
Average Pressure Specification?	no
Specify targeted mass flow rate	no
— Wall	
— wall-22	
Wall Motion	Stationary Wall
Shear Boundary Condition	No Slip
— wall-21	

Wall Motion	Stationary Wall
Shear Boundary Condition	No Slip
━ wall-19	
Wall Motion	Stationary Wall
Shear Boundary Condition	No Slip
━ wall-18	
Wall Motion	Stationary Wall
Shear Boundary Condition	No Slip
━ wall-fff_main_component	
Wall Motion	Stationary Wall
Shear Boundary Condition	No Slip
━ wall-fff_entry	
Wall Motion	Stationary Wall
Shear Boundary Condition	No Slip
━ wall-fff_exit	
Wall Motion	Stationary Wall
Shear Boundary Condition	No Slip

Reference Values

Area	1 m^2
Density	1.225 kg/m^3
Enthalpy	0 J/kg
Length	1 m
Pressure	0 Pa
Temperature	288.16 K
Velocity	1 m/s
Viscosity	1.7894e-05 kg/(m s)
Ratio of Specific Heats	1.4
Yplus for Heat Tran. Coef.	300
Reference Zone	fff_main_component

Solver Settings

— Equations	
Flow	True
— Numerics	
Absolute Velocity Formulation	True
— Pseudo Transient Explicit Relaxation Factors	
Density	1
Body Forces	1
Explicit Momentum	0.5
Explicit Pressure	0.5
— Pressure-Velocity Coupling	
Type	Coupled
Pseudo Transient	True
— Discretization Scheme	
Pressure	Second Order
Momentum	Second Order Upwind
— Solution Limits	
Minimum Absolute Pressure [Pa]	1
Maximum Absolute Pressure [Pa]	5e+10
Minimum Temperature [K]	1
Maximum Temperature [K]	5000

Run Information

Number of Machines	1
Number of Cores	6
Case Read	6.223 seconds
Data Read	0.629 seconds
Virtual Current Memory	0.998463 GB
Virtual Peak Memory	1.02349 GB
Memory Per M Cell	3.96147

Plots

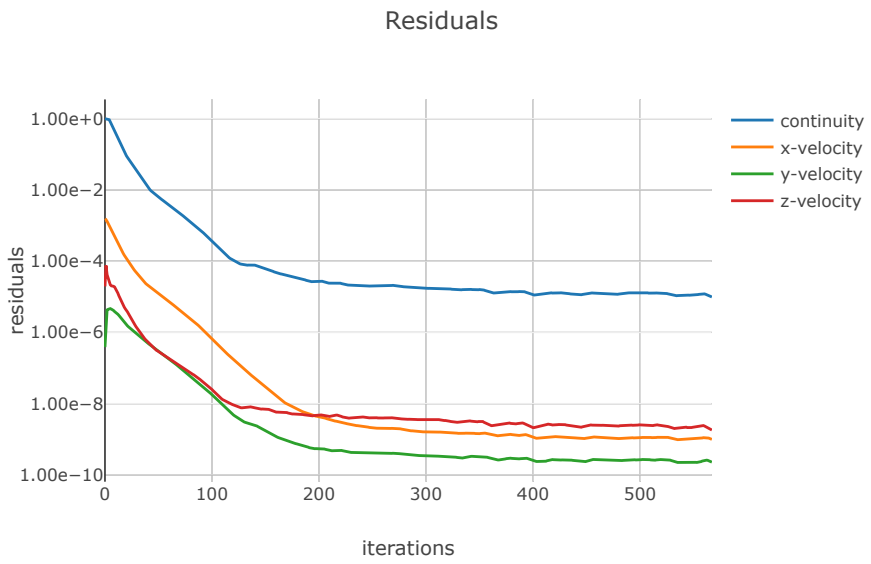
Residuals
1.00e+0
1.00e−2
1.00e−4
1.00e−6
1.00e−8
1.00e−10
residuals
0
100
200
300
400
500
iterations
continuity
x-velocity
y-velocity
z-velocity

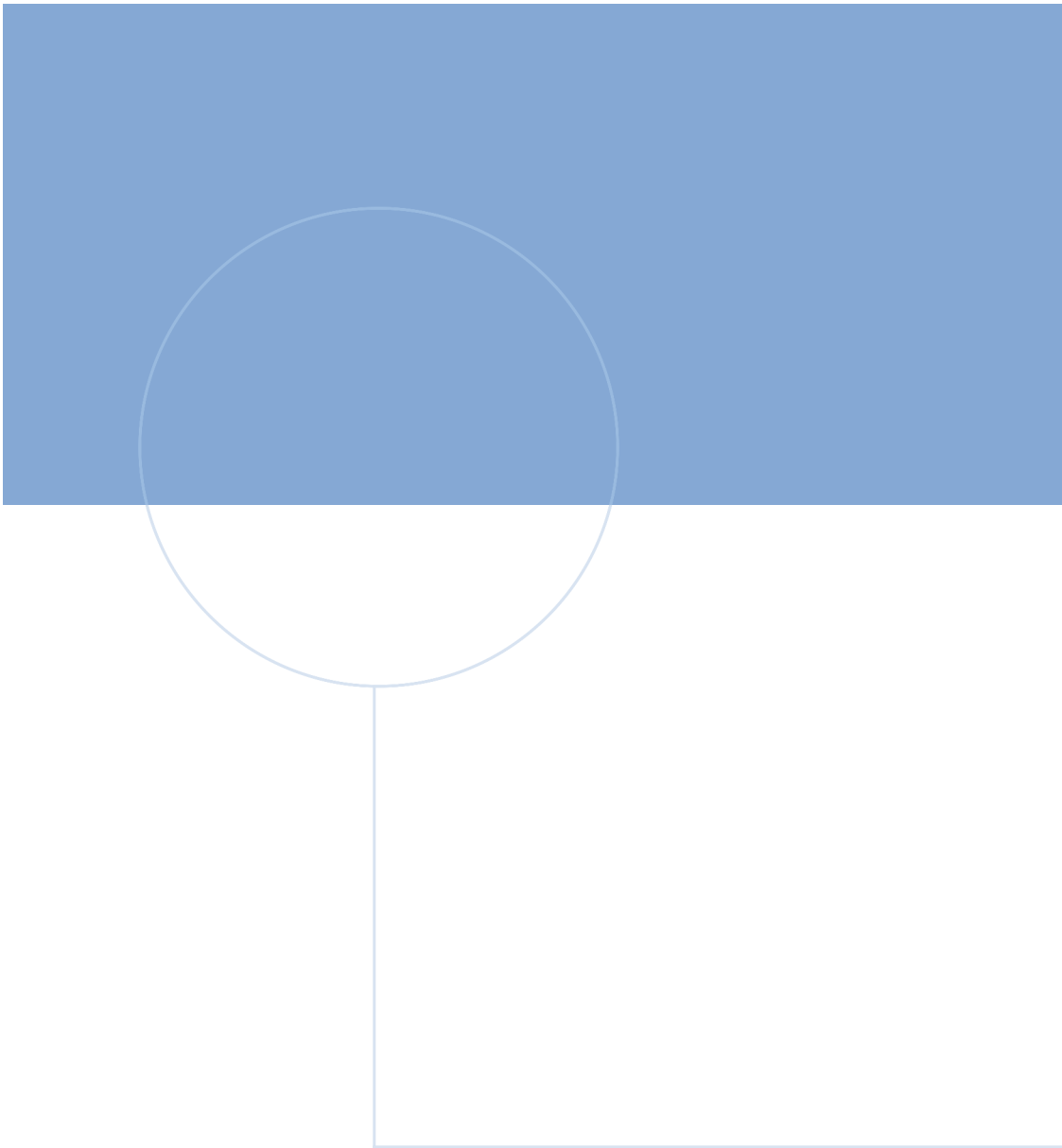

NTNU

Norwegian University of
Science and Technology